5-2010

Monotonic and Cyclic Compression Behavior of Bulk Metallic Glasses

Matthew Webster Freels
University of Tennessee - Knoxville, mfreels1@utk.edu

To the Graduate Council:

I am submitting herewith a dissertation written by Matthew Webster Freels entitled "Monotonic and Cyclic Compression Behavior of Bulk Metallic Glasses." I have examined the final electronic copy of this dissertation for form and content and recommend that it be accepted in partial fulfillment of the requirements for the degree of Doctor of Philosophy, with a major in Materials Science and Engineering.

Peter K. Liaw, Major Professor

We have read this dissertation and recommend its acceptance:

Yanfei Gao, John D. Landes, James R. Morris

Accepted for the Council:

Carolyn R. Hodges

Vice Provost and Dean of the Graduate School

(Original signatures are on file with official student records.)

To the Graduate Council:

I am submitting herewith a dissertation written by Matthew Webster Freels entitled "Monotonic and Cyclic Compression Behavior of Bulk Metallic Glasses." I have examined the final electronic copy of this dissertation for form and content and recommend that it be accepted in partial fulfillment of the requirements for the degree of Doctor of Philosophy, with a major in Materials Science and Engineering.

Peter K. Liaw, Major Professor

We have read this dissertation and recommend its acceptance:

Yanfei Gao

John D. Landes

James R. Morris

Accepted for the Council:

Carolyn R. Hodges
Vice Provost and Dean of the Graduate School

(Original signatures are on file with official student records.)

\

MONOTONIC AND CYCLIC COMPRESSION BEHAVIOR OF BULK METALLIC GLASSES

A Dissertation Presented for the
Doctor of Philosophy Degree
University of Tennessee, Knoxville

Matthew Webster Freels
May 2010

DEDICATION

This dissertation is dedicated to my wife, Jessica B. Freels, for her encouragement, love, and tremendous patience (most of the time) throughout my graduate studies; and my parents, James D. and Elizabeth L. Freels, for their encouragement, love, and support throughout my life in whatever endeavors I pursue.

ACKNOWLEDGMENTS

I would like to acknowledge the financial support of the National Science Foundation: (1) the Division of the Design, Manufacture, and Industrial Innovation Program, under Grant No. DMI- 9724476, (2) the Combined Research-Curriculum Development (CRCD) Programs, under EEC-9527527 and EEC-0203415, (3) the Integrative Graduate Education and Research Training (IGERT) Program, under DGE-9987548, (4) the International Materials Institutes (IMI) Program, under DMR-0231320, and (5) the Major Research Instrumentation (MRI) Program, under DMR-0421219, to the University of Tennessee, Knoxville, with Dr. D. Durham, Ms. M. Poats, Dr. C.J. Van Hartesveldt, Dr. D. Dutta, Dr. W. Jennings, Dr. L. Goldberg, Dr. C. Huber, and Dr. C.R. Bouldin as Program Directors, respectively.

I would also like to thank Prof. Peter K. Liaw for his advice, assistance, and guidance during my graduate career. Moreover, I would like extend thanks to my committee members Profs. Yanfei Gao, John D. Landes, and James R. Morris, for their time and advice. Also, this research would not have been possible without the assistance of Greg Jones, Douglas Fielden, Larry Smith, Dan Hackworth, Frank Holiway, Randy Stooksbury, Carla Lawrence, Sandra Maples, and Susan Seymour of The University of Tennessee. Many thanks also goes to all of my team members at the University of Tennessee.

ABSTRACT

The cyclic-compression behavior of a $Cu_{45}Zr_{45}Al_5Ag_5$ bulk metallic glass (BMG) was investigated in order to elucidate the damage initiation and growth mechanisms. The present $Cu_{45}Zr_{45}Al_5Ag_5$ BMG was found to have the highest fatigue-endurance limit for BMGs reported to date. Fracture under cyclic compression occurred in a pure shear mode. In addition to many shear bands and cracks, areas of "chipping" were commonly found on the outside surfaces of the fatigue specimens. Crack growth rates were found decrease with cycles.

The effects of the as-cast specimen size, cooling rate, and the free volume content on the monotonic and cyclic compression behavior of a Zr-based BMG was investigated. The smaller samples experienced a faster cooling rate, resulting in a higher free volume content. The smaller samples displayed superior monotonic compression and cyclic compression properties. This trend was attributed to a higher free volume content.

The effect of the sample aspect ratio (height/diameter) on the cyclic compression behavior of a Zr-based BMG was explored. For smaller aspect ratios (0.5), the yield strength and compressive plastic strain significantly increased when compared to that for an aspect ratio of 2. In general, when the aspect ratio was 0.5, the fatigue lives were longer than when the aspect ratio was 2. The dramatic effect of the sample aspect ratio was attributed to the development of a hydrostatic stress state from the interaction of the

uniaxial applied load and the friction stress developed at the interface of the top and bottom specimen surfaces and the platens.

The stress-life fatigue behavior and fracture morphology of a $(Cu_{60}Zr_{30}Ti_{10})_{99}Sn_1$ BMG alloy was investigated under both 3-point and 4-point bending conditions. For all stress levels tested, the fatigue lifetimes tended to be higher for the 3-point loading condition. All fracture surfaces were found to be comprised of four main regions: a crack-initiation site, a stable crack-growth region, an unstable fast-fracture region, and a melting region. Finely spaced parallel marks oriented somewhat perpendicular to the direction of crack propagation were observed in the stable crack-growth region. Analyses of these marks found that their spacing increased with increasing stress-intensity-factor range.

TABLE OF CONTENTS

List of Figures		
Figure		**Page**
2-1	The correlation between T_g / T_l and (a) R_c, and (b) t_{max} [93].	97
2-2	The correlation between ΔT_{xg} and (a) R_c and (b) t_{max} [93].	98
2-3	The correlation between γ and (a) R_c, and (b) t_{max} [93].	99
2-4	Typical room temperature stress-strain curves for BMGs; (a) tension and (b) compression.	100
2-5	Shear bands in a Pd-based BMG [180].	101
2-6	Schematics of the two main theories that exist in the literature that attempt to describe the deformation mechanisms of metallic glasses, including (a) a local atomic jump [39] and (b) a STZ [41].	102
2-7	Compressive fracture surface of a Zr-based BMG [4].	103
2-8	Liquid droplets on the fracture surface of a Zr-based BMG [181].	104
2-9	Crack growth rate (da/dN) as a function of ΔK for a Zr-based BMG [2]. Also shown are results for a high-strength steel and an age-hardened aluminum alloy for comparison.	105
2-10	S-N data showing large variability in the S-N behavior of BMGs even for seemingly the same alloy [11].	106
2-11	A comparison of the S-N behavior of all BMG compositions under cyclic bending [19, 34, 128-133], TT [7, 29, 30, 135-139], and CC [29, 38, 137] loading conditions.	107
2-12	Comparing the S-N behavior of a Zr-based BMG with various finishes [146].	108
2-13	S-N data for various Zr-based BMGs tested under same TT cyclic loading conditions [139].	109
2-14	The fracture surface of a Zr-based BMG subjected to TT fatigue [135]; (a) over all fracture surface showing four distinct regions: the crack initiation site, crack propagation, unstable fast fracture, and apparent melting regions, (b) higher magnification of the crack propagation region, (c) transition from stable crack propagation to unstable crack propagation (fast fracture), (d) higher magnification of the unstable crack propagation region, and (e) melting region.	110
2-15	Fatigue fracture surface of a Zr-based BMG during CC cyclic loading [29]; (a) severely damaged surface area on the outside surface, (b) failure occurs by unstable fracture in a shear mode, and (c) vein-like structure that nearly covers the entire fracture surface.	113
4-1	Monotonic compressive stress–strain curve for the $Cu_{45}Zr_{45}Al_5Ag_5$ BMG at a strain rate of $3 \times 10^{-4} s^{-1}$. The BMG displays a compressive ε_p of 0.004. The σ_F reaches 1,845 MPa, while the measured E is approximately equal to 90 GPa.	115
4-2	Fracture under compression occurring in a pure shear mode. The fracture plane forms an θ_c of 41° with respect to the compressive loading axis. The two arrows in the top right corner indicate the	116

Note: Sections 3.1.3, 3.3.3, 4.4, 5.4, and 6.4 contained in this dissertation have been previously published in the following reference: M. Freels, P. K. Liaw, G. Y. Wang, Q. S. Zhang and Z. Q. Hu, Journal of Materials Research 22 (2007) 374.

1. INTRODUCTION

As a result of the successful development of bulk metallic glasses (BMGs) in many different alloys systems, research on the mechanical behavior of BMGs has been very active [1]. BMGs have been found to exhibit many excellent mechanical properties, such as high hardness [2], high elastic limit [3], high yield strength [4], high fracture toughness [5], high specific strength [6], and high fatigue endurance limits [7]. However, their low ductility [8] and unpredictable fatigue behavior [9-11] hinder their progress as structural materials. Therefore, it is worthwhile to study the fundamental mechanisms of the mechanical behavior of BMGs. Thus, their impressive properties can be exploited and BMGs can be utilized for engineering applications.

It is well known that the mechanical behavior of crystalline materials is affected by processes taking place at the microscopic and/or atomic level [12]. However, the relationship between the mechanical response and the non-crystalline structure of BMGs is not well established. Although research in the area of the mechanical behavior of BMGs is very active, the basic knowledge of the underlying mechanisms that control their deformation and fracture behavior is still debated [1].

Due to their inherit amorphous structure, BMGs do not possess any of the traditional notions of crystalline defects, such as dislocations or grain boundaries. Consequently, traditional deformation mechanisms associated with conventional crystalline alloys do not apply to BMGs. At low temperatures or high strain rates, BMGs deform inhomogeneously with deformation

confined to narrow shear bands, which rapidly propagate until catastrophic failure. At high temperatures or low strain rates, BMGs deform more homogenously [13-15]. Moreover, under tensile loading, BMGs display zero plasticity, while in compression, some ductility is observed [16].

Fatigue in materials is the result of the kinematic irreversibility of the microscopic deformation processes, such as the to-and-fro motion of dislocations and associated plastic strain accumulation during cyclic loading of crystalline metals. It has been experimentally established that BMGs are prone to fatigue failure [2, 7, 17]. However, the sources of kinematic irreversibility in BMGs have yet to be determined.

As potential materials for engineering applications, the knowledge of how BMGs behave under cyclic-loading conditions is crucial. Therefore, the fatigue behavior of BMGs deserves further attention. In crystalline alloys, fatigue damage can initiate along persistent slip bands, grain boundaries, or some other preexistent flaw (such as inclusions or gas pores) [18]. Recently, a number of studies have focused on the fatigue behavior of Zr-based BMGs [2, 19-35]. These studies have revealed that BMGs are susceptible to fatigue degradation. Shear localization occurs, which leads to the initiation of fatigue damage under cyclic loading. Crack-growth rates depend on the applied stress-intensity range. However, early studies found fatigue lifetimes to be shorter compared with conventional crystalline alloys. In fact, one study [19] of a Zr-Ti-Ni-Cu-Be alloy showed the fatigue endurance limit to be as low as 9% of the tensile strength when. This value is very low compared to conventional crystalline materials, such as high-strength steels and aluminum alloys, whose fatigue endurance limits are typically 30 - 40% of their tensile strength. Since then, however, a number of fatigue studies on several different

Zr-based systems have shown more promising results [22-27], with endurance limits reaching as high as 30 - 50% of their tensile strength. The results of these more recent studies are promising, providing encouragements to further study the fatigue behavior of BMGs.

Fracture mechanics concepts generally assume that compression-compression cyclic loading, or random compressive loads mixed with cyclic tensile loads, do not significantly affect fatigue-crack growth behavior. This concept is based on the assumption that fatigue cracks remain closed during the compressive load, or even below the crack-closure load [36]. However, studies have shown that compressive loads can have significant effects on the initiation and growth of fatigue cracks [37].

BMGs generally exhibit superior mechanical properties under compression than under tension, exhibiting greater strength and, in some cases, plasticity [4]. Therefore, the potential exists for BMGs to find applications in compression-dominated, fatigue-critical applications. However, the fatigue behavior of BMGs under cyclic compression has received little attention [29, 32, 38]. This manuscript will address the cyclic compression behavior of a $Cu_{45}Zr_{45}Al_5Ag_5$ BMG. Both stress-life and the fatigue crack propagation behavior will be investigated in order to elucidate the fatigue damage initiation and growth mechanisms.

At low temperatures (e.g., room temperature), BMGs deform inhomogeneously and are characterized by the formation of localized shear bands. These narrow shear bands rapidly propagate, resulting in catastrophic failure. The inhomogeneous deformation in BMGs is usually described by the free volume theory [39-41]. Argon introduced the concept of the shear transformation zone (STZ). These STZs are small regions where the local atomic structure is rearranged when a shear stress is applied. The amount of free volume determines the ability of a

region to develop an STZ. Free volume is essentially "extra" volume, relative to a fully dense glass structure, which is frozen into the atomic structure and allows physical space for atomic movement under an applied stress [39-41]. The free volume is assumed to be uniformly distributed among all the atoms in the BMG, implying that the flow defects (or STZs) are also uniformly distributed.

The amount of free volume in a BMG is expected to have significant effects on its ability to plastically deform [42, 43]. An increase in free volume will result in an increase in plasticity. The amount of free volume is in a metallic glass depends on the cooling rate from a fixed temperature [44]. It is also expected that the cooling rate for a given composition will increase with a decrease in the specimen casting size (d) [45]. Therefore, it would be reasonable to assume that the free volume content increases (as well as the ductility) with a decrease in specimen casting size.

The potential effects of free volume on the fatigue lifetimes of BMGs have only been investigated in a few studies [46, 47], and the results are conflicting. Moreover, it is expected that there is a size effect in the fatigue behavior of engineering materials [48]. The fatigue strength of larger samples is lower than that of small specimens. Since fatigue damage usually initiates from the surface, increasing the surface area can significantly effect the fatigue strength of a material. In this manuscript, the affects of the specimen size and free volume on the cyclic compression behavior a Zr-based BMG will be investigated.

A major drawback of BMGs is their brittleness under unconstrained conditions. At low homologous temperatures, typically including room temperature, BMGs usually fail by the formation of highly localized shear bands, leading to catastrophic failure without obvious

macroscopic plasticity [49, 50]. This inherent poor ductility and subsequent catastrophic fracture severely limits their processing and applications as engineering materials.

Various strategies have been developed to improve their ductility. One strategy is the composite approach, in which case the amorphous matrix is reinforced with a second phase [51]. Under unconstrained loading conditions, the second phase confines the propagation of shear bands and promotes their multiplication. This feature can result in an increase in the plasticity, impact resistance, and toughness [51]. Moreover, it has recently been discovered that BMG foams show an improvement in ductility when compared to solid BMGs [52]. Similarly, the pores in the foams can also restrict the propagation of shear bands.

In addition to interior structural changes, it is also possible to promote shear band multiplication and prevent catastrophic failure by exterior constraints. For example, Lu and Ravichandran [53] were able to promote large inelastic deformation of more than 10% in compression using a confining sleeve technique. This feature was attributed to the development of multiple shear bands that were visible on the surfaces of the deformed specimens. Schroers et al. [54] performed bending tests on a Pt-based BMG using rectangular bar specimens with different thicknesses. It was found that the specimen with a thickness of 1.8 mm did not fail during bending and the strain exceeded 14.2%. However, the specimen with a thickness of 4 mm had a strain to fracture of only 3%. The bending ductility for the thinner specimen was the result of the formation of multiple shear bands.

The specimen geometry can also have a dramatic influence on the monotonic compressive ductility of BMGs [55-59]. For example, Jiang et al. [55] found that the specimen height (h) to diameter (d) ratio (h/d), or aspect ratio, significantly affects the monotonic

compressive plasticity of BMGs. Specimens with aspect ratios larger than 0.75 exhibited poor ductility, while specimens with aspect ratios smaller than 0.75 showed excellent ductility with a maximum strain up to 80%. The results were attributed to the specimen geometry effect. The loading platen hindered the propagation of the shear bands, which prevented premature fracture in the smaller aspect ratios. A similar trend was found in other studies [56-58]

As potential materials for engineering applications, the knowledge of how BMGs behave under cyclic-loading conditions is crucial. However, how the specimen geometry can affect the fatigue behavior of BMGs has yet to be investigated. In this study, how the aspect ratio affects the cyclic compression behavior of a Zr-based BMG will be investigated.

2. REVIEW OF RELATED LITERATURE

2.1 Historical Background

By definition, a glass is a non-crystalline solid exhibiting the phenomenon of glass transition. The corresponding physical state is called the vitreous state. One cannot simply call a glass a "non-crystalline solid" or "amorphous solid". Although glass is truly a non-crystalline solid, all non-crystalline solids are not necessarily glasses – e.g., gels. Glasses are characterized not only by the absence of crystallinity, but above all by their ability to pass progressively and reversibly to a more and more fluid state as the temperature is increased. During this change, there is a modification of properties called the glass transition. Moreover, there are basically three different ways of forming a glass: 1) formation from a liquid phase by freezing of a supercooled liquid, 2) formation from a phase by non-reactive deposition, and 3) formation from a solid phase from radiation damage or mechanical damage. The definition given above does not place any restrictions on the manner in which the vitreous material is formed.

Glass formers are known in all major bonding classes: covalent, ionic, van der Waals, hydrogen bond, and metallic. Metallic glasses are alloys with no long-range and limited short-range atomic ordering. Their atomic bonding continues to be metallic, but the structure is amorphous, similar to a metal in its liquid state.

What causes a material to become glassy? When a liquid is cooled, one of two events may occur. If the liquid is slowly cooled, crystallization will take place at the melting temperature (T_m). If the liquid is cooled sufficiently fast, nucleation of crystalline phases can be completely avoided, and the liquid will become supercooled for temperatures below T_m. As a supercooled liquid is cooled to lower temperatures, it becomes more and more viscous and the

atoms which comprise it move more and more slowly. Eventually, the atoms will be moving so slowly that they do not have a chance to rearrange themselves significantly before the temperature is lowered further, falling out of equilibrium into the structurally arrested glass state. The temperature at which this phenomenon occurs is known as the glass transition temperature (T_g).

The structure and properties of a glass depend on previous thermal history such as the cooling rate. T_g is different for different cooling rates. A slower cooling rate allows the sample to stay in equilibrium, i.e., the supercooled liquid state, until lower temperatures. Typically, the dependence of T_g upon cooling is relatively weak; an order of magnitude change in the cooling rate may change T_g by only 3 - 5 K. A glass is observed to have a greater specific volume and heat content when produced at faster cooling rates (T), as illustrated in Figure 2-1. G_1 and G_2 correspond, respectively, to the glass state obtained upon cooling a liquid at rates T_1 and T_2, for which $T_1 > T_2$. Upon subsequent heating at a rate slower than either T_1 or T_2, the glass tends to relax structurally to a more stable glassy state at temperatures far below T_g, as indicated by a dashed line.

In 1960, Klement et al. [60] reported for the first time the formation of the amorphous alloy, specifically a $Au_{75}Si_{25}$ alloy, cooled directly from the melt utilizing a rapid quenching technique [61]. Their work showed that the process of nucleation and growth of a crystalline phase could be kinetically bypassed in some alloy melts, if undercooled uniformly and rapidly enough, yielding a frozen liquid configuration. The significance of Duwez's work was that, compared to other methods such as thin-film techniques [62], their method [61] permitted relatively large quantities of an alloy to be made into an amorphous state.

Early on, the most important experimental condition necessary to avoid crystallization was a high rate of heat transfer to the cooling medium. The highest heat transfer rates are achieved by conduction from the liquid to a highly conductive metallic substrate. These conditions were incorporated into the method employed by Klement et al. [60] to produce the $Au_{75}Si_{25}$ amorphous alloy [61]. The method, generally referred to as the gun technique (or splat cooling), consists of propelling a small liquid globule by means of a shock tube and spraying it into a thin foil on a copper substrate. The substrate was curved so that centrifugal force promoted good thermal contact between the liquid layer and the substrate. The cooling rate produced by the gun technique was, on average, about 10^{6}°Cs^{-1} and as high as 10^{8}°Cs^{-1}.

However, the gun technique only extracted heat from one side of the melt. This limitation was removed in the next design in which the liquid globule is squeezed between a fast moving piston and a fixed anvil [63]. Both the piston and the anvil were lined with copper to insure fast heat removal. This revised design had similar cooling rates as the gun technique, but could produce amorphous foils that were twice as thick. Utilizing the piston and anvil technique, Duwez et al. would later demonstrate glass formation in the binary Pd-Si alloy system [64] and ternary Pd- [65] and Fe-based [66] systems.

If one arbitrarily defines the millimeter scale as ‘‘bulk’’, the earliest reports of BMG formation date back to 1969, when Chen and Turnbull [67] were able to form amorphous ternary Pd–Si–N (N = Ag, Cu or Au) alloys with thicknesses greater than 1 mm at much lower cooling rates (~10^{3}°C/s) simply by dropping the melt onto a metal substrate (Ag or Cu). In 1974, using simple suction casting methods with cooling rates of 10^{2}°C/s to 10^{3}°C/s, Chen performed systematic investigations on the Pd–T–P (T = Ni, Co, and Fe), Pd-M-Si (M = Au, Ag, Cu, Ni,

Co, Fe, and T), and Pt-Ni-P systems, producing glassy rods with critical casting thickness > 1 mm in these alloys [68].

During the early 1980s, the Turnbull group studied the Pd–Ni–P alloys [69, 70]. Drehman et al. were able to successfully prepare glassy ingots of $Pd_{40}Ni_{40}P_{20}$ with a diameter of 5 mm with cooling rates as low as 1 °C/s. This was made possible by etching the ingots to eliminate surface heterogeneities, then subjecting them to a succession of heating and cooling cycles. Kui et al. extended the critical casting thickness of the $Pd_{40}Ni_{40}P_{20}$alloy to 1 cm by utilizing a boron oxide fluxing method to purify the melt. This $Pd_{40}Ni_{40}P_{20}$ alloy was the first BMG with a critical thickness near 1 cm to be developed. Moreover, in 1982, Lee et al. reported the formation of $Au_{55}Pb_{22.5}Sb_{22.5}$ metallic glass spheres with diameters near 1.5 mm produced by cooling in a drop tower at relatively low cooling rates [71].

However, the above BMGs were unlikely to be widely applied due to the expense of the precious metals and the rigorous preparations required to produce them. For a period of time, BMGs were thought to be somewhat of a laboratory curiosity.

It was not until the late 1980s that the Inoue group began to investigate the glass forming ability (GFA) of a number of multicomponent alloy families containing more common elements and involving less special precautions. Using simple metal mold casting methods, they systematically assessed the critical cooling conditions required to form a number of metallic glasses. For example, utilizing a copper-mold casting method, Inoue et al. developed $La_{55}Al_{25}Ni_{20}$ amorphous alloys with a large glass-forming capacity in cylindrical and sheet forms, with critical thicknesses of 3 and 2.3 mm, respectively [72, 73]. Inoue et al. also studied the Mg-Cu-Y system, finding that the $Mg_{65}Cu_{25}Y_{10}$ alloy possesses significant GFA [74].

Amorphous alloys in cylindrical form with a maximum diameter of 4 mm were produced by injection casting of the melt into copper molds [75], Shortly after, amorphous cylinders with a maximum diameter of 7 mm were produced by a high-pressure die casting technique [76]. Moreover, Inoue et al. discovered that the ternary Zr-Al-Ni system [77] and quaternary and quinary alloys in the Zr-Al-TM (TM = Co, Ni, and Cu) system [78] possessed large glass-forming capacities. Specifically, the $Zr_{65}Al_{7.5}Ni_{10}Cu_{17.5}$ alloy showed exceptional GFA, and Inoue et al. would later show that this alloy could be water quenched to produce 16 mm diameter rods [79].

It soon became apparent that the work by Inoue and colleagues showed that BMGs in multicomponent alloys was a far more general phenomenon than previously thought and not limited to just a few special alloys. The significance of Inoue's work was quickly recognized by Johnson and colleagues from Caltech. In 1993, Peker and Johnson studied the quinary Zr-Ti-Cu-Ni-Be system [80], most importantly the $Zr_{41.2}Ti_{13.8}Cu_{12.5}Ni_{10}Be_{22.5}$ alloy, commonly referred to as Vitreloy 1 (Vit1) [80]. At cooling rates < 1°C/s, the Zr-based alloy could be water quenched to form a fully amorphous rod up to 14 mm in diameter. Lin and Johnson would later investigate the Ti-Zr-Cu-Ni system [45], and found that the best glass forming alloys, specifically the $Ti_{34}Zr_{11}Cu_{47}Ni_8$ alloy, could be cast to a thickness of at least 4 mm using an injection casting technique and a critical cooling rate near 10°C/s.

Since the pioneering work of Duwez, the critical casting thickness has increased by more than three orders of magnitude, with the largest thickness over 70 mm in the Pd-Cu-Ni-P system [81]. Today, research continues on alloy development, and a number of systems based on magnesium, lanthanum, zirconium, palladium, iron, cobalt, titanium, calcium, copper, and nickel

have been discovered [82]. Recently, Takeuchi and Inoue classified BMGs according to the atomic size difference, heat of mixing, and period of the constituent elements in the periodic table [83].

2.2 BMG Formation

Prior to the development of BMGs in the late 1980's, metallic glasses were produced using techniques involving rapid quenching from the melt [84]. These techniques included sputtering and evaporation, chemical deposition and electrodeposition, ion implantation, splat quenching and spray deposition, fabrication of amorphous powders, and filaments, ribbons and tapes using continuous casting methods [84].

BMG fabrication methods can be classified into two groups [85]: (1) solidification, and (2) consolidation. The different solidification techniques include water quenching [86], high pressure die casting [76], arc melting [87], copper mold casting [75], unidirectional casting [88], and suction casting [89]. BMGs can also be produced by hot pressing and warm extrusion of atomized amorphous powders in the supercooled liquid state [87, 90, 91].

The most straightforward indicators of GFA are the critical cooling rate (R_c) and the maximum sample thickness (t_{max}). Alloys with high GFA have a lower R_c and greater t_{max}. Although these indicators are fundamental parameters, they are difficult to measure precisely and do not tell much about the potential of an alloy system to be vitrified into the amorphous state. Thus, a more simple, reliable, and measurable gauge of GFA is needed to develop new amorphous alloys.

Many criteria have been proposed to reflect relative GFA among BMGs on the basis of the characteristic temperatures measured by differential scanning calorimetry (DSC) and/or

differential thermal analysis (DTA). The most extensively used are the reduced glass transition temperature (T_{rg}) [92] and the supercooled liquid region (ΔT_{xg}) [85]. More recently, the γ criterion [93] was developed in an attempt to address the shortcomings of T_{rg} and ΔT_{xg}. The current GFA criteria are utilized during alloy development, using T_g, T_m, liquidus (T_l) and crystallization (T_x) temperatures. The initial efforts at finding BMG forming compositions relied primarily on empirical approaches, rationalized by thermodynamics and kinetics, and which serve as the basis for current predictive models.

Turnbull used the thermodynamic and kinetic factors influencing glass formation to formulate the first measurable parameter that could be used as a measure for the GFA of an alloy system [92]. He pointed out that if the ratio of T_g to T_m was $\geq 2/3$ (or as T_g gets closer to T_m), the nucleation of the undercooled melt should be slow enough to allow solidification of the melt without crystallization. This criterion is commonly known as the "Turnbull criterion" or T_{rg}:

$$T_{rg} = T_g / T_m \qquad 1$$

Based upon this criterion, the GFA should increase as T_{rg} increases. The use of T_{rg} as a predictive measure points toward alloys with low melting points, as T_g cannot be easily predicted. Thus, good glass-forming alloys are commonly found near eutectic compositions with low T_m. More recently, Lu et al. [94] pointed out that T_l should be employed for T_{rg} in place of T_m, as using this value gives a stronger correlation with GFA. This can be easily understood as T_m and T_g are both less composition dependent while T_l is strongly dependent on the composition. Figure 2-1 (All Tables/Figures are located in the Appendix) shows R_c (Figure 2-1a) and t_{max} (Figure 2-1b) as a function of T_g / T_l for metallic glasses [93]. As T_g / T_l increases, R_c decreases and t_{max} increases. The R^2 value, also known as the coefficient of determination, is an

indicator that ranges in value from 0 to 1. The higher the R^2 value, the more reliable the regression line should be.

Upon annealing a glass, crystal nuclei start to form and grow at T_x. The size of ΔT_{xg}, or the temperature interval between T_g and T_x, has been emphasized by Inoue [85] as an indicator of the stability of the amorphous phase to crystallization. The ΔT_{xg} is defined as follows:

$$\Delta T_{xg} = T_x - T_g \qquad 2$$

As described by Inoue, the GFA of the alloy should increase as ΔT_{xg} increases. The correlation between ΔT_{xg} and R_c and t_{max} for various metallic glasses is shown in Figure 2-2a and 2-2b, respectively [93]. Although not a clear relation is observed, R_c and t_{max}, seem to decrease and increase, respectively, as ΔT_{xg} increases.

More recently, Lu and Liu [93] have systematically addressed the weaknesses of the T_{rg} and ΔT_{xg} criteria. They proposed a new, comprehensive criterion (γ) for the prediction of GFA as follows:

$$\gamma = T_x / (T_g + T_l) \qquad 3$$

The denominator accounts for the liquid phase stability (thermodynamics) while the numerator describes the resistance to crystallization (kinetics). As T_l and T_g decrease, the supercooled liquid stability and GFA increase. On the other hand, higher values of T_x result in an increased resistance to crystallization and a higher GFA. Therefore, the best GFA is obtained when γ is equal to 0.5. Figure 2-3 displays the correlation between R_c (Figure 2-3a) and t_{max} (Figure 2-3b) and γ. By comparing the R^2 in Figures 2-1, 2-2, and 2-3, it appears that the γ criterion is a more reliable criterion to reflect the GFA of metallic glasses.

Inoue et al. proposed three empirical rules [85] for the achievement of a large glass-forming ability as follows: (a) a multicomponent system consisting of three or more elements, (b) atomic size ratios with differences of greater than 12% among the constituent elements, and (c) negative heats of mixing among the constituent elements. The need for multicomponents was recognized as being of great importance only after the advent of BMGs and is often termed as the confusion principle in glass formation [95]. The introduction of a new component into an alloy introduces local atomic level strain along with chemical disorder, frustrating crystallization. For two atoms of different sizes, there exists a critical maximum solubility in the solid solution. Multicomponent glass-forming alloys contain elements with significant differences in their atomic sizes. Due to this, the random packing density of the alloy increases.

2.3 Mechanical Behavior of Bulk Metallic Glasses

The mechanical behavior of metallic glasses is characterized by either inhomogeneous (room temperature) or homogeneous deformation (in or near the supercooled liquid region). This research is only concerned with room-temperature inhomogeneous deformation. Homogeneous deformation will not be dealt with here, but the reader can refer to Schuh et al. [1] for a complete discussion of this type of deformation mode.

2.3.1 Monotonic Inhomogeneous Deformation

Schematics depicting typical room temperature stress-strain curves for BMGs are shown in Figure 2-4. A major advantage of BMGs is their high elastic strain (~ 2%) [4], which is much higher than that of common crystalline metallic alloys (typically < 1%) [12]. In addition, due to the lack of microstructural features, such as grains, grain boundaries, and dislocations, the strengths of BMGs are very high. Strengths are usually near 2 GPa [4], but can be much higher

in some cases [96]. Macroscopically, BMGs usually only exhibit an elastic response under tension, with essentially no plastic strain (Figure 2-4a) [4]. Under compressive loading, BMGs exhibit a nominally elastic-perfectly plastic response, and can show a limited amount of plastic strain (Figure 2-4b) [4].

Bonding in BMGs is primarily metallic, and atomic bonds can be broken and reformed at the atomic scale without concern for the rigidity of bond angles (covalent bonding), or the balance or charges (ionic bonding) [12]. As a result, strain can easily be accommodated at the atomic level. However, BMGs do not exhibit long-range translational symmetry like crystalline alloys do. Dislocations in metals allow atomic-level rearrangements at low energies or stresses, but the local rearrangement of atoms in BMGs is a relatively high-energy or high-stress process.

Flow in BMGs is extremely inhomogeneous at high stresses and low temperatures. Deformation is localized in shear bands (Figure 2-5) near planes of maximum shear due to a local change in the viscosity within these bands. The change in the viscosity is caused by a volume increase that is thought to possibly come about either by mechanical dilatation or thermal expansion.

For the mechanical dilatation theory, free volume accumulates within a shear band during deformation, decreasing the density of the glass, leading to a decrease in the viscosity within the band. Thus, it is usually assumed that the amount and distribution of the free volume controls plastic flow. It is generally thought that, in order for BMGs to accommodate strain, there must be a process involving the local rearrangement of atoms.

Figure 2-6 shows two-dimensional schematics of the two main theories that exist in the literature that attempt to describe the deformation mechanisms of metallic glasses, including

local atomic jumps [39] (Figure 2-6a) and STZs [41] (Figure 2-6b). Spaepen proposed an atomistic free volume deformation theory for metallic glasses based on a competition between the stress-driven creation and diffusional annihilation of free volume. Deformation is the result of a series of individual atomic jumps (Figure 2-6a), which are easily accommodated near sites of high free volume. Steif modified Spaepen's model by deriving an expression for the stress at which catastrophic softening due to free volume creation occurs during uniform shear of a homogeneous body under constant applied strain rate [40].

On the basis of atomistic simulations and sheared bubble raft experiments, Argon introduced the first quantitative model of STZ behavior to explain the plastic deformation of BMGs [41]. This model depicts glass deformation as a collective effect arising from the operation of many small atomic-scale shear events (Figure 2-6b), in which a few atoms collectively shuffle in a shear mode under the combined action of stress and temperature. The physical basis for such local shear events was provided by early simulations of amorphous systems [97, 98]. More recent simulations [99-101] have continued to support this model.

These models suggest basically the same sequence of events to shear band formation in metallic glasses. First, strains are accommodated elastically, until the stress level increases to a point where flow is activated in a locally disturbed region. This causes a mismatch in strain rate between the disturbed and undisturbed regions. Strain softening occurs in the disturbed region, further intensifying the strain rate mismatch, leading to a runaway growth process (shear band). The shear band continues to grow until a new equilibrium redistribution of shear flow is reached between band and matrix.

In plastic deformation, almost all of the work done on the sample is dissipated as heat. If the deformation is heavily concentrated in a few bands, one can expect a substantial increase in temperature and a corresponding drop in viscosity. The possibility that shear banding events are essentially adiabatic phenomena (similar to adiabatic shear bands in crystalline alloys) and was first proposed by Leamy et al. [102], who attributed the vein pattern morphology (Figure 2-7) of fracture surfaces to adiabatic heating of the deformed region. This feature is the same as that produced by pulling apart two solid surfaces with a thick viscous layer between them [102]. The viscosity of the material in the shear band has dropped by many orders of magnitude. Moreover, liquid droplets (Figure 2-8) are frequently observed on the fracture surfaces of metallic glasses, suggesting that the temperature rise is high enough to lead to melting.

However, because shear bands are thin, move fast (close to the speed of sound), and are short-lived, it is not easy to measure this temperature rise directly. Although infrared measurements clearly show temperature rises, the spatial and temporal resolution of these techniques are too low to allow accurate determination of the temperature evolution in shear bands [49, 103-105]. Lewandowski and Greer [106] coated a BMG sample with a thin layer of tin. After deformation, they observed that the tin near the shear bands had beaded up due to melting. Their method had excellent resolution, allowing them to estimate the temperature rise to possibly several thousand degrees. They find, however, that the width of the hot zone is significantly larger than the width of shear bands. Moreover, Wright et al. [107] found that it was unlikely that the primary cause of flow localization was localized heating.

The local heating, therefore, is not considered to be the origin of shear localization. Instead, changes in viscosity associated with increased free volume in the shear band seem more

consistent with experiments. Nevertheless, as a secondary effect, it remains important to the evolution of the material in the bands.

BMGs experience dilatation due to plastic deformation [39, 41, 108]. Thus, shear band formation leads to several predictions [108]: (1) inhomogeneous yielding should be dependent on the hydrostatic component of the applied stress (or the normal stress acting on the shear plane), (2) the yield stress should depend more strongly on changes in the bulk modulus of the glass than on changes in the shear modulus, and (3) excess free volume should be retained in a BMG after plastic flow.

Donovan [108] investigated the yielding behavior of a Pd-based metallic glass subjected to different loading modes, including uniaxial compression, plane strain compression, pure shear, and tension. He proposed that the Mohr-Coulomb criterion can be used to describe yielding:

$$\tau_\theta = \tau_0 - \alpha\sigma_\theta \qquad 4$$

where τ_θ is the shear stress acting on the shear plane, σ_θ is the normal stress acting on the shear plane, τ_0 is the shear resistance (i.e., the yield stress in pure shear), and α is a system specific friction coefficient that controls the strength of σ_θ. For this criterion, the critical shear yield stress is dependent on the normal stress acting on the shear plane. The Mohr-Coulomb criterion has been supported by many studies [3, 4, 109, 110]. The value of α defines the extent to which the normal stress σ_θ influences the effective shear yield stress. Donovan found experimentally that $\alpha = 0.113 \pm 0.03$ for a Pd-based metallic glass [108], which is consistent with simulations by Schuh et al., who came up with $\alpha = 0.123 \pm 0.004$ for a Cu-Zr model system [111].

There is also a size effect found for BMGs. Guo et al. [112], using in situ tensile tests in a transmission electron microscope, observed significant plastic strain (23–45%) in metallic

glasses with thicknesses near 100 nm. Wu et al. [113] also observed a size effect in tension. A size effect has also been seen in compression [114]. There have been numerous ideas to explain this phenomenon: (1) the probability of finding a critical flaw (such as pores, unmelted particles, oxides, inclusions, etc.) is lower in the smaller sample [115, 116]; (2) the smaller sample experiences a faster cooling rate during solidification, thus trapping more free volume, which would favor shear localization [117, 118]; (3) the plastic zone size is larger than the smaller sample size, such that brittle failure due to catastrophic crack propagation is not favorable [119]; and (4) when the specimen size is smaller than the inherent critical shear offset, the shear deformation should be stable up to the occurrence of certain tensile plasticity [113]. Moreover, sometimes no shear bands are observed at all during deformation of small samples, with groups calling this a form of "homogeneous deformation" [120, 121], while others have reported stable shear localization throughout the deformation process, leading to extensive plastic strain [114].

Under unconstrained conditions, BMGs develop highly localized shear bands, leading to catastrophic failure without obvious macroscopic ductility [1]. This lack of ductility severely limits the usefulness as engineering materials. However, it is possible to limit the propagation of individual shear bands and thus distribute the plastic strain over many bands. This delays the onset of fracture and produces significant macroscopic plastic strains. A common method of accomplishing this effect is by producing materials consisting of an amorphous matrix with one or more discontinuous crystalline phases [51, 122]. BMG foams can display plasticity up to 80% without macroscopic fracture [52].

One obvious way to achieve larger plastic strains is to provide a geometrical constraint to shear band propagation. Conner et al. [123] found that thin metallic glassy ribbons showed

ductility without failure in bending, but thicker plates fail catastrophically. Using a confining sleeve technique, Lu and Ravichandran [53] observed a large plastic deformation of more than 10% in compression, which was the result of numerous shear-banding operations. When subjected to cold rolling, the BMGs can undergo deformation with plasticity up to 70% [124]. Bruck et al. [50] investigated the effect of the aspect ratio (height (h) / diameter (d)) on the compressive properties of a Zr-based BMG. A slight increase in the yield strength and an obvious increase in the compressive plasticity was observed on going from as aspect ratio of 2 to an aspect ratio of 0.5.

Recently, several investigators have studied in more detail how the aspect ratio effects the strength, ductility, and the corresponding deformation and fracture mechanisms of several Zr-based BMGs [55, 58, 59]. Zhang et al. [59] studied the compressive deformation behavior of BMGs with aspect ratios ranging from 0.67 up to 2 found that the compressive plastic strain monotonically increases with decreasing aspect ratio, but the maximum strength almost maintains a constant value. The high ductility (> 18%) of the BMG samples with small aspect ratios (< 1) were attributed to the formation and interaction of multiple shear bands. Failure was found to obey the Mohr-Coulomb criterion for all aspect ratios. Zhang et al. speculated that, besides the uniaxial stress, there is a lateral stress induced by friction between the ends of the samples and the crosshead of the testing machine. For BMGs with large aspect ratios, the lateral stress acts only close to the end of the sample and plays only a minor role in determining the deformation and fracture of the BMG samples. With decreasing aspect ratio, the effect of the lateral stress will continuously increase due to the strong effect of the friction between the sample and the crosshead. Once shear bands have formed, their rapid propagation will be

difficult due to the strong constraint imposed by the lateral stress and the crosshead of the testing machine. With further loading, the density of the shear bands will continue to increase, resulting in a high compressive plasticity.

Wu et al. [58] found that for an aspect ratio of 0.25, the yield strength increased significantly (2,415 MPa) when compared to that for an aspect ratio of 2 (1,860 MPa). Moreover, significant work hardening was observed, in constrast to Zhang et al., who did not find any work hardening for aspect ratios larger than 0.67. This feature suggests that different deformation mechanisms occur at very low aspect ratios.

2.4.2 Cyclic Loading of Bulk Metallic Glasses

Work on the fatigue behavior of BMGs has shown that the crack-growth behavior is similar to that of other high strength crystalline alloys [2]. However, the S-N behavior appears to be significantly different [7, 17, 19, 34]. Moreover, there is considerable scatter in the S-N results, even for seemingly the same composition [9-11]. A brief summary of the work that has been done so far is given below.

Early work on metallic glass ribbons and wires [125-127] established that the fatigue crack growth obeys the Paris equation [36]:

$$\frac{da}{dN} \propto (\Delta K)^m \qquad 5$$

where a is the crack length, N is the number of cycles, ΔK is the stress intensity factor range, and m is an empirical constant, which is a function of material properties, microstructure, fatigue properties, mean stress, environment, loading mode, stress state, and test temperature. More recent work on BMGs which satisfy plane strain conditions confirm this [2, 5, 9]. Figure 2-9 shows da/dN as a function of ΔK for a Zr-based BMG [2]. Also shown are results for a high-

strength steel and an age-hardened aluminum alloy for comparison. The value of m for BMGs typically range from 2 to 5, which is similar to ductile crystalline alloys and much lower than oxide glasses [36]. BMGs also show a fatigue threshold, ΔK_{th}, and typical values range from 1 to 5 MPa $m^{1/2}$ [2, 5, 9], and is again comparable to many ductile crystalline alloys [36].

The S-N behavior of BMGs has been studied under four point bending (4PB) [19, 34, 128-133], three point bending (3PB) [129, 130, 134], uniaxial tension-tension (TT) [7, 29, 30, 135-139], uniaxial compression-compression (CC) [29, 38, 137], and rotating bending (RB) [140-142] cyclic loading conditions. BMGs exhibit a fatigue endurance limit (σ_L, defined here as the applied stress range, σ_R (σ_{max} - σ_{min}, where σ_{max} and σ_{min} are the maximum and minimum applied stress, respectively), below which fatigue failure does not occur after 10^7 cycles). Because BMGs do not exhibit plasticity, a perfectly amorphous alloy, could, in theory, exhibit a fatigue limit that approaches the ultimate tensile strength [143]. However, this early idealistic theory has not been realized for BMGs experimentally. In fact, the resistance of BMGs to cyclic loads ranges from relatively poor [7, 19, 34, 136] to rather impressive [7, 135], with fatigue ratios (σ_L/σ_F, where σ_F is the fracture strength) ranging from 0.08 [19] up to 0.60 [137]. Conventional crystalline alloys, such as high-strength steels, titanium alloys, or aluminum alloys, typically exhibit σ_L/σ_F ranging from 0.30 to 0.50 [144].

Moreover, large variability in the S-N behavior of BMGs is observed (Figure 2-10), even for seemingly the same alloy. For example, Gilbert and co-workers [19] performed 4PB fatigue tests and reported a fatigue ratio of 0.08 for a Zr-based BMG (Vitreloy 1) (Figure 2-10), while Wang et al. [136] performed TT tests and found the fatigue ratio to be as high as 0.38 for the same Vitreloy 1 alloy (Figure 2-10). Why do BMGs appear to show such erratic S-N behavior?

Menzel et al. [9] tried to attribute the above observed difference to an error in the stress concentration factor for the geometry used by Wang et al. However, Wang et al. [11] employed finite element analysis to verify the stress concentration factor and found it to be acceptable (Figure 2-10). Wang et al. claimed other factors, such as the specimen geometry, material quality, environment, residual stress, and surface condition, could be possible reasons for the large discrepancies. The reason for such erratic S-N behavior has been addressed in a number of other studies as well [17, 19, 34, 38, 128, 129, 135, 136, 138]. However, no real definitive answer exists. Nevertheless, some of the possible reasons will be discussed briefly here.

A comprehensive summary of the experimental conditions and the reported fatigue endurance limits for BMGs is given in Table 2-1. Figure 2-11 gives a comparison of the S-N behavior of BMGs under cyclic bending [19, 34, 128-133], TT [7, 29, 30, 135-139], and CC [29, 38, 137] loading conditions. At first glance of Figure 2-11, one possible explanation for such erratic behavior would appear to be the fatigue loading mode. It is obvious from Figure 2-11 that BMGs give the longest lives, at both high and low stresses, under CC cyclic loading conditions. At lower stresses, TT cyclic loading conditions generally have longer lives than bending conditions. However, at higher stress, TT and bending conditions appear to be very similar. Fatigue endurance limits seem to be highest for CC, followed by TT and the least being bending conditions.

Another possible explanation could be the different volumes of material being tested. During the fatigue process, the probability of finding a critical flaw is proportional to the volume of material experiencing the maximum stress [144]. The 4PB method employed by Gilbert et al. [19] had a much larger volume of material experiencing the maximum tensile stress when

compared to the TT method of Wang et al. [136] Fatigue damage in BMGs usually initiates at the surface from stress concentrators [17, 34, 145], such as scratches or inclusions. The larger test volume of material experiencing the maximum tensile stress of the 4PB geometry could contain more stress concentrators, which would enhance the possibility for fatigue damage initiation, resulting in a lower fatigue limit. This trend could possibly explain, at least in small part, the lower fatigue limit reported by Gilbert et al. [19]. However, Morrison et al. [128] recently performed 4PB fatigue experiments on a very similar Zr-based BMG (Vitreloy 105), and found fatigue lifetimes very similar to that observed by Wang et al. [136]. This trend would suggest that the loading mode and/or testing volume cannot alone account for the large differences observed in the S-N behavior of BMGs.

Fatigue damage in BMGs nearly always originate at the surface from stress concentrators [17, 34, 145], such as scratches or inclusions. Therefore, the condition of the surface of a BMG could play a decisive role in dictating the initiation life for fatigue cracks. Peter et al. [146] found that under TT fatigue, BMGs were highly sensitive to changes in the surface roughness (Figure 2-12). The σ_L was reduced by 28% with a surface roughness of 0.552 μm, and reduced by 56% with a surface roughness of 0.667 μm, when compared to a fine polish (surface roughness of 0.163 μm). Peter et al. also noted that BMGs seem to be more sensitive to surface finish than most conventional high-strength crystalline alloys. This may be associated with a crystalline alloys' ability to strain hardening, which could inhibit flow. BMGs exhibit elastic-perfectly plastic behavior and do not strain harden.

Another factor that could influence the S-N behavior is the quality of the BMG material itself. It is known that BMG alloys are very sensitive to oxygen contamination. Oxygen

impurity was found to dramatically reduce the GFA and severely embrittle a Zr-based BMG [147]. Oxygen has been shown to be very detrimental to the fatigue life of BMGs [136]. Moreover, BMGs could contain small amounts of crystalline inclusions that cannot be identified by laboratory XRD. Unfortunately, in many cases, laboratory XRD is the only technique utilized to characterize the structure of BMGs. Laboratory XRD has limited capabilities, and cannot detect the presence of small crystalline inclusions. Many of the BMGs reported in the literature are deemed "completely amorphous" based solely on the results of laboratory XRD. However, the fatigue behavior of BMGs has been shown to be significantly affected by partial crystallization [21, 138]. Wang and co-workers [138] found that the fully amorphous BMG showed longer fatigue lifetimes when compared to the partially crystallized BMG of the same composition. In contrast, Flores et al. [21] found the endurance limit to be greater for a partially crystallized Vitreloy 1 alloy when compared to that of the fully amorphous Vitreloy 1 alloy.

Slight compositional changes in BMGs can also significantly affect S-N behavior, which is depicted in Figure 2-13. The S-N data in this figure are from a number of different Zr-based BMGs tested under the same TT cyclic loading conditions. The cyclic loading frequency employed during fatigue testing could also be another factor. The tests performed by Gilbert et al. were done at a frequency of 25 Hz [19], while the experiments conducted by Wang et al. were done at 10 Hz [136]. Other factors that could affect the S-N behavior of BMGs include mean stress, testing environment, temperature, residual stresses.

The fatigue damage mechanisms for TT and bending fatigue appear to be very similar [7, 17, 34, 128, 130, 136]. Even though they are not well understood, some basic observations have been made. During cyclic loading, damage first initiates as shear bands. For a defect free

material, shear bands could initiate from regions of higher free volume. Cameron et al. [31] used a Lennard-Jones model to characterize the free volume evolution during fatigue deformation. It was found that cyclic loading in shear or tension increased the overall free volume with each cycle, and that localization of free volume during cyclic loading could lead to eventual shear band formation.

However, BMGs inevitably will contain some amount of defects. Therefore, under TT and bending fatigue, fatigue damage nearly always originates at the surface from stress concentrators [17, 34, 145], such as scratches or inclusions. Menzel et al. [34] observed that the shear bands initiate and grow at an angle > 45° with respect to the loading axis. Once the shear bands reach a critical length, they abruptly change direction and grow as mode I cracks, perpendicular to the loading direction, until failure occurs. Since the shear band is thought to contain excess free volume [39, 41], it is mechanically weak relative to the surrounding volume. Thus, a shear band is a potential site for the nucleation of a fatigue crack.

Under TT and bending fatigue, the fracture surface of BMGs can exhibit four distinct regions (Figure 2-14a): the crack initiation site, crack propagation, unstable fast fracture, and apparent melting regions [17, 34, 129]. The fracture surface as a whole is basically perpendicular to the loading direction. Once the crack initiates, it then propagates towards the inside of the specimen. The propagation region (Figure 14b), where stable-crack growth occurred, is thumb-nail in shape and exhibits striation-like features [2]. These characteristics are thought to be the result of some type of a cyclic crack tip blunting and resharpening process. However, striation spacing is often larger than da/dN (Figure 2-9), suggesting that there is an accumulation of damage necessary prior to crack advance. The striation-like features usually do

not extend over the entire crack front, which suggests that the crack front grows in non-uniform manner during steady-state fatigue crack growth. The transition from the crack propagation region to the unstable fast fracture region is distinct (Figure 2-14c), indicating that the two regions are controlled by different fracture mechanisms. The unstable fast fracture region (Figure 2-14d) occupies the majority of the fracture surface, and appears somewhat similar to monotonic tensile fracture surfaces. Finally, an apparent melting region (Figure 2-14e) has been observed, which exhibits distinct melting marks and vein patterns.

Compared to the fatigue behavior of BMGs under TT and bending cyclic loading, very little effort has been put towards understanding the fatigue behavior of BMGs under CC cyclic loading. Nevertheless, several observations have been made, which distinguish CC fatigue from TT or bending fatigue [29, 38, 130]. Again, fatigue damage first initiates in the form of shear bands, leading to the formation of fatigue cracks. As cyclic loading continues, areas of severe surface damage sometimes form on the outside surfaces (Figure 2-15a), where small fragments of material have chipped away. Zhang et al. [29] proposed that ultimate failure occurs when the effective surface area is no longer able to support the load.

Fracture surfaces of BMGs cyclically loaded in CC are drastically different than those of TT and bending fatigue. Although the overall fracture surface is again relatively flat, failure occurs by unstable fracture in a shear mode (Figure 2-15b), with the angle of the fracture plane with respect to the loading axis being less than 45°. A vein-like structure (Figure 2-15c), similar to the monotonic compression fracture surface (Figure 2-7), forms on the CC fatigue fracture surface. The vein-like structure nearly covers the entire fracture surface, and is uniformly oriented along the shear direction. In addition to the severely damaged surface areas, many shear

bands and cracks are observed on the outside surfaces of the fatigue specimens (Figure 2-14b). A major distinction between CC fatigue and TT and/or bending is the absence of the striation-like features on CC fatigue fracture surfaces. Moreover, failure appears to be the result of a damage accumulation process with contributions from multiple fatigue cracks.

3. EXPERIMENTAL PROCEDURE

3.1. Material

3.1.1. $Cu_{45}Zr_{45}Al_5Ag_5$ BMG

The $Cu_{45}Zr_{45}Al_5Ag_5$ (in atomic percent) BMGs used in this study were prepared by arc melting mixtures of pure [(> 99.5 weight % (wt.%)] Cu, Zr, Ag, and Al metals in an argon atmosphere. The ingots were re-melted four times to ensure chemical homogeneity. Glassy alloys were produced by injection copper mold casting to produce rod samples with a length of 45 mm and a diameter (d) of 3 mm. The as-cast samples were, subsequently, polished to a 6.5 μm finish. Laboratory x-ray diffraction (XRD) analyses was conducted on selected samples using a Philips X'pert x-ray diffractometer (Almelo, The Netherlands) to characterize the structure.

3.1.2. $(Zr_{53}Cu_{30}Ni_9Al_8)_{99.5}Si_{0.5}$ BMG

The $(Zr_{53}Cu_{30}Ni_9Al_8)_{99.5}Si_{0.5}$ (in atomic percent) BMGs used in this study were provided by I-SHOU University, Kaohsiung, Taiwan. The alloy ingots were prepared by arc melting of the appropriate mixture of pure elements, including Zr (99.8 wt% purity), Ni (99.9 wt% purity), Cu (99.99 wt% purity), Al (99.99 wt% purity), and Si (99.99 % purity), under a Ti-gettered argon atmosphere. The alloy ingots were then remelted in an arc furnace under a purified argon atmosphere. After complete melting, the liquid alloy was drop cast into the water-cooled Cu mold to form alloy rods with d of 2 and 4 mm. Laboratory XRD analyses was conducted on selected samples using a Philips X'pert x-ray diffractometer (Almelo, The Netherlands) to characterize the structure. The thermal properties were measured in a Perkin-Elmer Diamond differential scanning calorimeter (DSC) at a heating rate of 20 K/min.

3.1.3. $(Cu_{60}Zr_{30}Ti_{10})_{99}Sn_1$ BMG

The $(Cu_{60}Zr_{30}Ti_{10})_{99}Sn_1$ BMG samples were prepared by arc melting the mixtures of pure metals in a Ti-gettered, high-purity argon atmosphere. Bulk rectangular rods with dimensions of 50 x 3 x 3 mm were, then, produced by copper-mold casting. The as-cast samples were, then, machined and polished to a 9 μm finish. The final dimensions were 25 x 2.85 x 2.85 mm. XRD analyses was, subsequently, conducted on selected samples using a Philips X'pert X-Ray Diffractometer to characterize the structure.

3.2 Monotonic Compression

3.2.1. $Cu_{45}Zr_{45}Al_5Ag_5$ BMG

In order to investigate the monotonic compressive behavior of the $Cu_{45}Zr_{45}Al_5Ag_5$, uniaxial compression tests were performed. The compression experiments were carried out at a strain rate of 3 x $10^{-4}s^{-1}$ using a computer-controlled Materials Test System (MTS) servohydraulic-testing machine. All samples were polished to a 5 μm finish. The final d was 2.95 mm with an aspect ratio of 2. Sample ends were polished to ensure parallelism.

3.2.2. $(Zr_{53}Cu_{30}Ni_9Al_8)_{99.5}Si_{0.5}$ BMG

In order to investigate the monotonic compressive behavior of the $(Zr_{53}Cu_{30}Ni_9Al_8)_{99.5}Si_{0.5}$, uniaxial compression tests were performed on both directly cast 2 and 4 mm d samples. The as-cast 2 mm specimens for the compression tests were machined to heights (h) of 4 mm, with a d = 2 mm, corresponding to an aspect ratio of 2. The as-cast 4 mm specimens for the compression tests were machined to h = 2 and 8 mm, corresponding to aspect ratios of 0.5 and 2, respectively. All samples were polished to a 5 μm finish. The compression

experiments were carried out at a strain rate of 3 x $10^{-4}s^{-1}$ using a computer-controlled MTS servohydraulic-testing machine. Sample ends were polished to ensure parallelism.

3.3. Cyclic Loading

3.3.1. $Cu_{45}Zr_{45}Al_5Ag_5$ BMG

Fatigue lifetimes were measured over a range of cyclic stresses under CC loading conditions. A computer-controlled MTS servohydraulic-testing machine was used for fatigue experiments. The load ratio, R (where $R = \sigma_{min}/\sigma_{max}$, and σ_{min} and σ_{max} are the applied minimum and maximum stresses, respectively), was kept at 10 under a load-control mode using a sinusoidal waveform. Complete S-N curves were conducted at frequencies of 10 and 40 Hz. Testing was performed in an air environment (~ 45 – 50% relative humidity and 25 °C). All samples were polished to a 5 μm finish. The final d = 2.95 mm with an aspect ratio of 2. Sample ends were polished to ensure parallelism. After testing, the samples were stored for later examinations using a scanning electron microscope (SEM). In order to better characterize the fatigue damage evolution, fatigue testing for a selected sample was periodically stopped. This arrangement allowed for the examination of the fatigue damage evolution and fracture mechanisms in the SEM. Upon the completion of the examination, the test was, then, subsequently resumed. This process was repeated until the specimen failed. Thus, the progressive fatigue damage mechanisms could be elucidated for the cyclic compression behavior of the $Cu_{45}Zr_{45}Al_5Ag_5$ BMG.

3.3.2. $(Zr_{53}Cu_{30}Ni_9Al_8)_{99.5}Si_{0.5}$ BMG

Fatigue lifetimes were measured over a range of cyclic stresses under $_{CC}$ loading conditions. A computer-controlled MTS servohydraulic-testing machine was used for fatigue

experiments. R was kept at 10 under a load-control mode using a sinusoidal waveform. Complete S-N curves were conducted for both directly cast 2 and 4mm samples. Testing was performed in an air environment (~ 45 – 50% relative humidity and 25 °C). All samples had an aspect ratio of 2. Sample ends were polished to ensure parallelism. After testing, the samples were stored for later examination using a SEM.

Fatigue lifetimes were also measured for as-cast specimens with h = 2 and h = 8 mm, with d = 4 mm, corresponding to aspect ratios of 0.5 and 2, respectively. These specimens were measured over a range of cyclic stresses under $_{CC}$ loading conditions. A computer-controlled MTS servohydraulic-testing machine was used for fatigue experiments. R was kept at 10 under a load-control mode using a sinusoidal waveform Sample ends were polished to ensure parallelism. Complete S-N curves were conducted for both aspect ratios of 0.5 and 2. Testing was performed in an air environment (~ 45 – 50% relative humidity and 25 °C). After testing, the samples were stored for later examination using a SEM.

3.3.3. $(Cu_{60}Zr_{30}Ti_{10})99Sn_1$ BMG

Fatigue lifetimes were measured over a range of cyclic stresses by cycling under 3PB and 4PB conditions. The outer span for 3PB was 20 mm. For the case of 4PB, the inner and outer spans were 10 and 20 mm, respectively. A MTS servohydraulic-testing machine was used for fatigue experiments. The R was kept at 0.1 under a load-control mode, using a sinusoidal waveform at a frequency of 10 Hz. Testing was conducted in an air environment (~ 45 - 50% relative humidity and 25°C). After testing, the samples were stored for later examination using SEM. Energy-dispersive spectroscopy (EDS) was employed to detect if any foreign elements were present near failure sites.

The microhardness of the material at room temperature was also determined. A Buehler Micromet 2101 microhardness tester fitted with a diamond Vickers indenter was used with a load of 500 g and loading time of 15 s.

4. RESULTS

4.1 Monotonic and Cyclic Compression Behavior of a CuZr-based Bulk Metallic Glass

4.1.1. Material

Recently, it has been reported that BMGs can be found in the binary Cu-Zr system [148, 149]. Moreover, by introducing additional alloying elements, the GFA of the binary Cu-Zr system can be increased [150]. Zhang et al. [151] studied the effects of additional Ag and Al on the GFA of Cu-Zr binary alloys. It was found that the $Cu_{45}Zr_{45}Al_5Ag_5$ alloy could be cast into d = 9 mm rods using a copper mold casting technique. The laboratory XRD patterns obtained in this study for d = 3 mm $Cu_{45}Zr_{45}Al_5Ag_5$ BMG showed a broad diffraction maximum, characteristic of metallic glasses, with no evidence of any obvious crystalline peaks. This result is consistent with those reported previously [151].

4.1.2. Monotonic Compression

Figure 4-1 shows the monotonic compressive stress–strain curve for the $Cu_{45}Zr_{45}Al_5Ag_5$ BMG at a strain rate of $3 \times 10^{-4} s^{-1}$. The BMG displays a compressive plastic strain (ε_p) of 0.004. The σ_F reaches 1,845 MPa, while the measured Young's modulus (E) is approximately equal to 90 GPa. The present results are consistent with those reported previously for the $Cu_{45}Zr_{45}Al_5Ag_5$ BMG [151, 152].

Fracture under monotonic compression occurred in a pure shear mode (Figure 4-2). The fracture plane forms an angle (θ_c) of 41° with respect to the compressive loading axis. On the outside surfaces of the fractured samples, only a few shear bands were observed. Most were near the fracture plane and at a similar angle. This trend is in agreement with the limited plasticity.

The observation of the fracture surface reveals that it is relatively flat and exhibits three distinct features: (1) a vein-like pattern that covers the majority of the fracture surface (area 1 in Figure 4-3), and is uniformly oriented along the shear direction (indicated in Figure 3 by an arrow), (2) a river-like pattern, which covers a small proportion of the fracture surface (area 2 in Figure 4-3), and (3) intermitting smooth regions (area 3 in Figure 4-3) throughout the vein-like and river-like features, and covering an even smaller proportion of the fracture surface. A similar fracture surface morphology was found on the fracture surfaces of a Cu-based BMG and a Zr-based BMG composite [153].

4.1.3. Cyclic Compression

The number of cycles to failure, N_f, measured as a function of the applied σ_R, is presented in Figure 4-4 for both 10 and 40 Hz. The fatigue-endurance limit (σ_L, defined as the applied σ_R below which fatigue failure does not occur after 10^7 cycles) was found to be at least 1,418 MPa for both frequencies tested. The fatigue-endurance limit can also be expressed in terms of the fatigue ratio (σ_L/σ_F). The present alloy was found to have a $\sigma_L/\sigma_{cf} = 0.77$.

At higher stresses above σ_L, the behavior was very similar for both frequencies. Thus, it is concluded that this BMG is not significantly affected by changes in frequencies in the range of 10 Hz up to 40 Hz. The relationship between σ_R and N_f for the data points above the endurance limits can be described by the following equations:

$$\sigma_R = -12.384\log(N_f) + 1624.9 \qquad \text{for 10 Hz} \qquad (6)$$

$$\sigma_R = -15.608\log(N_f) + 1669.1 \qquad \text{for 40 Hz} \qquad (7)$$

The R^2 value was found to be 0.28 and 0.66 for 10 Hz and 40 Hz, respectively. These low R^2 values (especially for 10 Hz) indicates the large scatter observed. The large scatter is thought to

be due to misalignment and critical defects found near the specimen/platen interface, which resulted in premature fracture in some cases.

Fracture under cyclic compression always occurred in a purely shear mode, as displayed in Figure 4-5. The fracture plane forms an angle (θ_{cc}) of 41° with respect to the loading axis, which is identical to the monotonic compressive fracture. On the outside surfaces of the fatigue specimens, significant damage was observed, as shown in Figure 4-6. Damage was in the form of: (1) shear bands and/or cracks (areas indicated by 1 in Figure 4-6), and (2) fragmentation (areas indicated by 2 in Figure 4-6), i.e. the metallic glass "chips" off from the outside surfaces. This "chipping" feature is unique to the outside surfaces of the cyclic compression specimens and was not observed on the monotonic compression outside surfaces. This feature was noticed on the outside surfaces of a Zr-based BMG specimen subjected to CC fatigue loading [29]. Moreover, further examination of the locations where "chipping" occurred revealed that the fracture surfaces of these areas formed an angle (θ_{chip}) of 41° with respect to the loading axis, as shown in Figure 4-7.

The fatigue fracture surface (Figure 4-8) is relatively flat and exhibits features very similar to the monotonic fracture surface, namely: (1) a vein-like pattern (area 1 in Figure 4-8) comprising the majority of the fracture surface and is uniformly oriented along the direction of shear (indicated in Figure 4-8 by the arrow), (2) small isolated regions of a river-like pattern (area 2 in Figure 4-8), and (3) smooth regions intermitting throughout the regions of the vein-like and river-like features (area 3 in Figure 4-8).

In order to understand the fatigue damage process under cyclic compression more clearly, a fatigue test ($\sigma_{max.}$ = 1,600 MPa) was stopped periodically so that the sample could be observed

in the SEM. Thus, damage initiation and growth mechanisms could be observed. The progression of fatigue damage shown here is from one location (a shallow surface pit) only. However, there were a number of surface defects acting as stress concentrators found on the surface, and many were observed to have fatigue damage initiate and grow from them. Many sites were analyzed, and the damage behavior described here was typical of that observed at other defect sites, and not just isolated occurrences.

Figure 4-9a displays fatigue damage that occurred after only 100 cycles. Damage first initiates from pre-existing surface defects in the form of shear bands or mixed-mode cracks very early in the fatigue process. The pre-existing surface defects that caused damage were usually shallow surface pits that formed during the casting process. The initial damage originates from the base of the shallow pit. The initial damage propagates at an angle that appears to be slightly $> 45°$ with respect to the loading axis. After 1,000 cycles, fatigue damage looks very much like that in Figure 4-9a.

With further cyclic loading (10,000 cycles), the crack growth direction has changed (Figure 4-9b, arrows indicate where the crack growth direction changes) to basically perpendicular to the loading direction. The first evidence of a "chipped" area is observed at this stage. After 30,000 cycles (Figure 4-9c), the cracks have continued to grow in a direction normal to the loading direction (indicated by arrows in Figure 4-9c). Many times, the cracks would propagate along polishing scratches. Commonly, the cracks would slightly change directions and "jump" onto other polishing scratches and continue to propagate, maintaining the overall crack growth generally perpendicular to the loading direction (Figure 4-9d). In a similar

manner, cracks would interact with other surface defects, resulting in a brief change in the growth direction or crack branching.

Moreover, a new area of surface damage has developed after 30,000 cycles (Figure 4-9c). New cracks can develop and propagate from the chipped areas (Figure 4-9c). Initially, these new cracks will be at an angle < 45° to the compression axis. Eventually, the cracks will change orientation and grow perpendicular to the loading direction.

As cyclic loading progressed to 50,000 cycles (Figure 4-9e), the cracks continue to propagate in a direction perpendicular to the loading axis (arrows labeled with a 1 in Figure 4-9e). The crack that developed from a damaged area in Figure 4-9c (after 30,000 cycles) turns over and begins growing in a direction perpendicular to the loading axis (arrows labeled with 2 in Figure 4-9e).

The sample shown in Figure 4-9 failed around 72,000 cycles (σ_{max} = 1,600 MPa). Cracks continue to grow up until failure, basically in a direction perpendicular to the loading axis. The "chipped" areas presented in Figure 4-9 did not progress on going from 30,000 cycles to 50,000 cycles. However, in many cases, they did sporadically grow in length, always perpendicular to the loading direction, as cyclic loading continued. Final failure occurred in a purely shear mode similar to that shown in Figure 4-5.

At times, the fracture plane would cut through areas containing cracks and chipped regions, allowing the crack propagation path toward the inside of the specimen to be seen. Figure 4-10 displays such an occurrence. On the right hand side of Figure 4-10 is a chipped area. The crack can be observed starting from this chipped area and propagating from right to left in a direction basically perpendicular to the loading direction. This is similar to that found in

crystalline metals, where the application of cyclic compressive loads can result in the propagation of fatigue cracks from stress concentrations (i.e. notches, voids, surface pits, etc.) in a direction normal to the compression axis [154]. The fact that stable crack propagation is normal to the loading direction suggests that final failure does not occur on the plane of a stable fatigue crack, since the final fracture occurred at a 41° angle with respect to the loading direction (Figure 4-5).

4.2 Effect of Specimen Size on the Monotonic and Cyclic Compression Behavior of a Bulk Metallic Glass

4.2.1. Material

The laboratory XRD patterns obtained in this study for both the 2 and 4 mm diameter $(Zr_{53}Cu_{30}Ni_9Al_8)_{99.5}Si_{0.5}$ alloy showed broad diffraction maximum, characteristic of metallic glasses, with no evidence of any obvious crystalline peaks. Figure 4-11 shows the DSC curves for both the 2 and 4 mm samples. The enthalpy of crystallization (ΔH) for the 2 and 4 mm samples are - 44.9 J/g and - 27.0 J/g, respectively. The greater crystallization peak for the 2 mm sample suggests that it has more free volume when compared to the 4 mm sample.

These results are consistent with those reported previously [155]. Jang et al. [156] has studied the $Zr_{53}Cu_{30}Ni_9Al_8$ amorphous alloy. The alloy was computationally designed using thermodynamics and the deep eutectic methodology [157]. The addition of Si improves the thermal stability by increasing the atomic packing density as well as the strong atomic bonding between Zr–Si and Ni–Si [155]. Moreover, the Si addition promotes a thin coating layer of Si on the nanocrystalline Zr_2Ni phase [155].

4.2.2. Monotonic Compression

Figure 4-12 shows the monotonic compressive stress-strain behavior of the $(Zr_{53}Cu_{30}Ni_9Al_8)_{99.5}Si_{0.5}$ BMG for the 2 and 4 mm samples. For the 2 mm sample, the yield stress (σ_Y), the σ_F, and ε_P were approximately 1,750 MPa, 1,950 MPa, and 0.55, respectively. For the 4 mm sample, the σ_Y, σ_F, and ε_P were approximately 1,650 MPa, 1,705 MPa, and 0.18, respectively. Thus, the as-cast specimen size (d) has an effect on the monotonic compressive properties for the present $(Zr_{53}Cu_{30}Ni_9Al_8)_{99.5}Si_{0.5}$ BMG.

For both the 2 (Figure 4-13a) and 4 mm (Figure 4-14a) specimens, fracture under monotonic compression occurred in a pure shear mode. The fracture planes of both the 2 and 4 mm form $\theta_C = 42°$ with respect to the compressive loading axis. Since plastic deformation in BMGs is confined to narrow shear bands [39-41], it is expected that the number and/or density of shear bands scale with ε_p. On the outside surfaces of the 2 mm fractured samples (Figure 4-13b), at least several shear bands are usually visible (indicated by arrows in Figure 4-13b). However, on the outside surfaces of the 4 mm fractured samples (Figure 4-14b), only one or two shear bands are visible (indicated by the arrow in Figure 4-14b), and are usually located near the fracture surface. These trends are in agreement with the stress-strain behavior and the observed plasticity for the 2 and 4 mm samples.

The fracture surfaces of the 2 (Figure 4-13c) and 4 mm (Figure 4-14c) monotonic compression specimens show three distinct features: (1) a vein-like pattern (areas with a 1), and is uniformly oriented along the shear direction (indicated by an arrow), (2) a river-like pattern (areas with 2), and (3) intermitting smooth regions (areas with 3). A similar fracture surface

morphology was found and the possible origins were discussed for a Cu-based BMG and a Zr-based BMG composite [153].

4.2.3. Cyclic Compression

The N_f measured as a function of the applied σ_R, is presented in Figure 4-15 for both 2 and 4 mm samples. The σ_L for the 4 mm sample was found to be at least 720 MPa, while σ_L was found to be at least 990 MPa for the 2 mm samples. The σ_L/σ_F were approximately 0.36 and 0.50 for the 4 and 2 mm samples, respectively. Decreasing the specimen d from 4 mm down to 2 mm led to a 27% and 39% increase in σ_L and σ_L/σ_F, respectively.

At high σ_R above σ_L, the 2 mm samples showed the longest fatigue lives. However, as σ_R reached the highest levels, the fatigue lives for both the 2 and 4 mm samples began to trend toward the similar values. The relationship between σ_R and N_f for the data points above the endurance limits can be described by the following equations:

$$\sigma_R = -63.802\log(N_f) + 2089.6 \qquad \text{for 2 mm samples} \qquad 8$$

$$\sigma_R = -86.223\log(N_f) + 2165.4 \qquad \text{for 4 mm samples} \qquad 9$$

The correlation coefficient (R^2) value was found to be 0.996 and 0.987 for the 2 and 4 mm samples, respectively.

Fracture under cyclic compression always occurred in a purely shear mode for both the 2 and 4 mm samples, as displayed in Figures 4-16a and 4-17a, respectively. The fracture planes formed an θ_{cc} of 42° with respect to the loading axis, which was identical to the monotonic compressive fracture.

On the outside surfaces of the 2 mm specimens, numerous shear bands and cracks were visible (Figure 4-16b). Comprising the majority of the fatigue damage were numerous primary shear bands and cracks, which were perpendicular to the loading direction. Still, many branching secondary shear bands were visible, which were at an angle to the loading direction. For the 4 mm specimens, a few shear bands and/or cracks (areas indicated by 1 in Figure 4-17b) were visible and were perpendicular to the loading direction. The number and/or density of the shear bands and cracks were significantly less than for the 2 mm samples. In addition, fragmented areas (indicated by 2 in Figure 4-17b) were visible. For these areas, the metallic glass "chips" off from the outside surfaces. This "chipping" feature was only found on the outside surfaces of the 4 mm cyclic compression specimens and was not observed on the 2 mm or 4 mm monotonic compression or 2 mm cyclic compression specimens. Further examination of the locations where "chipping" occurred revealed that the fracture surfaces of these areas also formed an θ_{chip} of 42° with respect to the loading axis, as shown in Figure 4-17c. This type of fracture feature was found on a Zr-based BMG [29] and Cu-Zr-based [158] BMG subjected to cyclic compression.

The fatigue fracture surfaces for the 2 and 4 mm samples are shown in Figure 4-16c and 4-17d, respectively. Both 2 and 4 mm fracture surfaces are relatively flat and exhibit fracture morphology very similar to the monotonic fracture surface, namely: (1) a vein-like pattern (areas with a 1), and is uniformly oriented along the shear direction (indicated by an arrow), (2) a river-like pattern (areas with a 2), and (3) intermitting smooth regions (areas with a 3).

4.3 Effect of a Confined Geometry on the Monotonic and Cyclic Compression Behavior of a Bulk Metallic Glass

4.3.1. Material

The $Zr_{53}Cu_{30}Ni_9Al_8$ BMG has been studied previously by Jang et al. [156]. The alloy was computationally designed using thermodynamics and the deep eutectic methodology [157]. The thermal stability can be improved by adding Si. This is accomplished by increasing the atomic packing density and strong atomic bonding between Zr-Si and Ni-Si [155]. A thin coating layer of Si is also created on the nanocrystalline Zr_2Ni phase [155]. The laboratory XRD patterns obtained in this study for the $(Zr_{53}Cu_{30}Ni_9Al_8)_{99.5}Si_{0.5}$ alloy showed a broad diffraction maximum, characteristic of metallic glasses, with no evidence of any obvious crystalline peaks. These results are consistent with those reported previously [155].

4.3.2. Monotonic Compression

Figure 4-18 shows the monotonic compressive stress-strain behavior of the $(Zr_{53}Cu_{30}Ni_9Al_8)_{99.5}Si_{0.5}$ BMG for both aspect ratios of 0.5 and 2. For the specimens with an aspect ratio = 2, the yield stress (σ_Y), the σ_F, and ε_P were approximately 1,650 MPa, 1,705 MPa, and 0.18, respectively. This is the usual expected stress-strain behavior for an unconstrained BMG. However, the specimens with an aspect ratio = 0.5 had a dramatically different behavior. Although the yield strengths are similar, the smaller aspect ratio resulted in a significant increase in the compressive plasticity. The flow stress continuously increases from the yield strength (~ 1,700 MPa) up to 3,750 MPa without failure. However, the result shown in Figure 4-18 for the aspect ratio of 0.5 was the maximum plasticity (near 35%) and maximum σ_F for all the specimens tested. The plasticity and σ_F varied when the aspect ratio was 0.5. The plasticity ranged from about 18% up to 35%, while the σ_F ranged from 2,500 MPa up to 3,750 MPa. As

the plasticity increased, so did the σ_F. With increasing deformation, d increased, their h decreased, all while maintaining their cylindrical shape. This behavior is similar to that observed by Jiang et al. [55].

The fracture features for monotonic compression when aspect ratio was 2 were discussed in Section 4.2.2 (4 mm sample) and are displayed in Figure 14. Failure occurred in a purely shear mode (Figure 4-14a) and the fracture plane was at an angle of 42° with respect to the compressive loading axis. On the outside surfaces of the fractured samples with an aspect ratio of 2 (Figure 4-14b), usually only several shear bands are visible (indicated by arrows in Figure 4-14b). This limited shear band development is in agreement with the observed plasticity for the specimens with an aspect ratio of 2. The fracture surfaces had three distinct features (Figure 4-14c): (1) a vein-like pattern (areas with 1), and is uniformly oriented along the shear direction (indicated by an arrow), (2) a river-like pattern (areas with 2), and (3) intermitting smooth regions (areas with 3).

A dramatically different behavior was observed when the aspect ratio was 0.5. Figure 19a displays the outside surface of a specimen that was strained to 29% without catastrophic failure. Numerous shear bands were visible on the outside surfaces. Primary shear bands were at an angle of 49° to the loading axis, and stop at the interface between the upper and lower surfaces of the specimen and the platens. This type of behavior has been seen before [55, 58]. The spacing between the primary shear bands range from 100 μm up to 150 μm.

Closer to the interface between the specimen surfaces and the platens, significantly more damage was found. In addition to the primary shear bands, many secondary shear bands and branching of shear bands are visible in this region (Figure 19b). The secondary shear bands

intersect the primary shear bands and are perpendicular to the loading direction. The shear offset at the intersection of the primary and secondary shear bands range from 5 μm up to 10 μm. The significant damage visible near the interfaces is thought to be caused by friction between the specimen and platen.

Upon failure of the specimens with an aspect ratio of 0.5, the specimens fractured into several small fragments (Figure 4-19c). Close examination of the small fragments found that their fracture surfaces were very similar to those found on the fracture surfaces of the specimens with an aspect ratio of 2. Three distinct features were observed (Figure 4-19d): (1) a vein-like pattern (areas with 1), and is uniformly oriented along the shear direction, (2) a river-like pattern (areas with 2), and (3) intermitting smooth regions (areas with 3).

4.3.3. Cyclic Compression

The N_f measured as a function of the applied σ_R, is presented in Figure 4-20 for both aspect ratios 2 and 0.5. The σ_L when the aspect ratio was 2 was at least 720 MPa. However, when the aspect ratio was 0.5, σ_L was not as definitive. Much like the monotonic compression stress-strain behavior when the aspect ratio was 0.5, the fatigue lives displayed were inconsistent. For example, of the three specimens tested at σ_R = 1,170 MPa, two failed well before 10^7 was reached. However, the third sample reached the endurance limit. At σ_R = 1,215 MPa, two samples were tested and both specimens failed before 3 x 10^6 cycles occurred. When σ_R was 1,260 MPa, one sample failed at 2.1 x 10^6 cycles. Surprisingly, the other sample tested at σ_R = 1,260 MPa did not fail after 10^7 cycles. Above σ_R = 1260 MPa, fatigue lives generally decreased with increasing σ_R. For the sake of this study, when the aspect ratio is 0.5, σ_L is said to be at least 1,170 MPa.

When the aspect ratio is 2, σ_L/σ_F is 0.36. However, when the aspect ratio is 0.5, σ_L/σ_F is difficult to define because of the range of σ_F. To define σ_L/σ_F for this study, σ_F is taken as the low end value (2,500 MPa), and σ_L/σ_F is 0.47. However, it is possible for σ_L/σ_F to be as low as 0.31, slightly lower than σ_L/σ_F when the aspect ratio is 2.

At high σ_R above σ_L, the longest fatigue lives were found when the aspect ratio was 0.5. The relationship between σ_R and N_f for the data points above the endurance limits can be described by the following equations:

$$\sigma_R = -86.223\log(N_f) + 2165.4 \qquad \text{for an aspect ratio of 2} \qquad 10$$

$$\sigma_R = -80.44\log(N_f) + 2218.2 \qquad \text{for an aspect ratio of 0.5} \qquad 11$$

The R^2 values were found to be 0.996 and 0.6247 for aspect ratios of 2 and 0.5, respectively.

The fracture features when the aspect ratio was 2 under cyclic compression were discussed in Section 4.2.3 (4 mm sample) and displayed in Figure 4-17. Fracture under cyclic compression always occurred in a purely shear mode (Figure 4-17a). The fracture planes formed $\theta_{cc} = 42°$, which was identical to the monotonic compressive fracture. On the outside surfaces, a few shear bands and/or cracks (areas indicated by 1 in Figure 4-17b) were visible and were perpendicular to the loading direction. In addition, chipped areas (indicated by 2 in Figure 4-17b) were visible. Again, the fracture surfaces of these areas also formed $\theta_{chip} = 42°$ with respect to the loading axis, as shown in Figure 4-17c. The fracture surface (Figure 4-17d) is relatively flat and exhibit fracture morphology very similar to the monotonic fracture surface, namely: (1) a vein-like pattern (areas with 1), and is uniformly oriented along the shear direction (indicated by an arrow), (2) a river-like pattern (areas with 2), and (3) intermitting smooth regions (areas with 3).

When the aspect ratio was 0.5, a slightly different behavior was found. Analogous to the monotonic compressive fracture, the samples fractured into several small fragments (Figure 4-21a). Many shear bands and/or cracks were visible on the outside surfaces of the small fragments (Figure 4-21b). The majority of the shear bands and/or cracks were oriented basically perpendicular to the loading direction. Compared to the cyclic compression samples with an aspect ratio of 2, the samples with an aspect ratio of 0.5 developed much more visible shear bands and/or cracks on the outside surfaces.

Close examination of the small fragments found that their fracture surfaces were very similar to that found on the fracture surfaces of the specimens with an aspect ratio of 2. Three distinct features were observed (Figure 4-21c): (1) a vein-like pattern (areas with 1), and is uniformly oriented along the shear direction, (2) a river-like pattern (areas with 2), and (3) intermitting smooth regions (areas with 3).

4.4 Cyclic Bending Behavior of a Cu-based Bulk Metallic Glass

4.4.1. Material

XRD patterns of these samples showed a broad diffraction maximum characteristic of metallic glasses with no evidence of any crystalline Bragg peaks. Although no transmission electron microscopy TEM work was done is this study, Zhang et al. did perform TEM work on this material [159], and the results were in agreement with the XRD pattern. The glass-transition temperature, T_g, for this material is 730 K, while the ΔT_{xg} is 46 K [159]. The microhardness (H_v) for this material at room temperature was found to be 5.5 GPa. Based on the empirical relationship between the H_v and σ_F, this material should have a σ_F near 1.8 GPa. Also, based on the linear relationship between H_v and E for other BMGs [85], E was estimated to be ~ 90 GPa.

4.4.2. Cyclic Bending

The N_f measured as a function of the applied σ_R, for both 3PB and 4PB conditions are presented in Figure 4-22. For all stress levels tested, the fatigue lifetimes tended to be higher for the 3PB condition than the 4PB condition. The values of σ_L, based on the applied σ_R, for 3PB and 4PB conditions were approximately 475 MPa and 350 MPa, respectively. The relationship between σ_R and N_f for the data points above the endurance limits can be described by the following equations

$$\sigma_R = -61.394 \log(N_f) + 1186.6 \qquad \text{for 3PB} \qquad 12$$

$$\sigma_R = -72.741 \log(N_f) + 1218.9 \qquad \text{for 4PB} \qquad 13$$

The R^2 value was found to be 0.85 and 0.71 for 3PB and 4PB, respectively. The large depths relative to the spans employed in this study can cause appreciable errors, due to both friction and wedging, when calculating stresses using conventional beam theory [160]. Analysis suggests that errors in the calculated stresses could be as high as 3 - 5% due to these effects.

To compare the results with those of others [19-21, 35], all the results were plotted together in Figure 4-23. All data, including those of others and this work, is from 4PB fatigue results. The fatigue lives of the present Cu-based BMG are lower than those of the $Zr_{47}Ti_{12.9}Nb_{2.8}Cu_{11}Ni_{9.6}Be_{16.7}$ BMG composite [20, 21] when the σ_R is higher than ~ 500 MPa. The fatigue lives are also lower than those of the $Zr_{41.2}Ti_{13.8}Cu_{12.5}Ni_{10}Be_{22.5}$ BMG [19] when σ_R is above ~ 350. The fatigue lives of the present alloy are lower than those of the $(Zr_{58}Ni_{13.6}Cu_{18}Al_{10.4})_{99}Nb_1$ BMG [35] for all stresses tested. The endurance limit of the present alloy was found to be ~ 350 MPa. This value is well above that of the $Zr_{41.2}Ti_{13.8}Cu_{12.5}Ni_{10}Be_{22.5}$ BMG (~ 135 MPa), while only slightly higher than that of the $Zr_{47}Ti_{12.9}Nb_{2.8}Cu_{11}Ni_{9.6}Be_{16.7}$

BMG composite (~ 292 MPa). However, the endurance limit of $(Zr_{58}Ni_{13.6}Cu_{18}Al_{10.4})_{99}Nb_1$ BMG (~ 560 MPa) is well above that of the present alloy.

The present alloy was found to have a fatigue ratio of $\sigma_R/\sigma_f \sim 0.26$ and $\sigma_R/\sigma_f \sim 0.19$ for 3PB and 4PB, respectively. The 4PB result is comparable to those (Figure 4-23) of the $Zr_{41.2}Ti_{13.8}Cu_{12.5}Ni_{10}Be_{22.5}$ BMG (~ 0.09) and $Zr_{47}Ti_{12.9}Nb_{2.8}Cu_{11}Ni_{9.6}Be_{16.7}$ BMG composite (~ .0.20). However, the $(Zr_{58}Ni_{13.6}Cu_{18}Al_{10.4})_{99}Nb_1$ BMG has the highest σ_L/σ_F (~ 0.328) of the four. Therefore, the fatigue properties of the $(Cu_{60}Zr_{30}Ti_{10})Sn_1$ BMG are comparable to that of the Zr-based BMG and BMG composites.

Figure 4-24 shows an overall fatigue fracture surface of a specimen tested under 3PB loading conditions at a σ_R = 580 MPa and failed after ~ 21,000 cycles. The fracture surfaces were found to be comprised of four main regions: a crack-initiation site, a stable crack-growth region, an unstable fast-fracture region, and a melting region. Similar features have been observed on fatigue fracture surfaces of Zr-based alloys [22-25, 35]. Figure 4-24a depicts a failure site of a sample tested under 4PB conditions at a σ_R of 650 MPa and failed after ~ 12,000 cycles, while Figure 4-24b shows the initiation site of the same sample at higher magnification. Cracks originated from the tensile side only, and were found to be associated with pre-existing defects, such as gas pores or surface trenches. The size of the initiation site ranged from ~ 5 – 10μm. EDS analyses showed no evidence of any foreign elements near initiation sites. For 3PB, cracks initiated near the region where the maximum stress was experienced, while cracks initiated between the inner loading points for 4PB. Corner cracks and surface cracks were found to occur with an equal probability.

Surrounding the initiation site was a stable crack-growth region (Figure 4-24a), which had a thumbnail shape appearance. The aspect ratio (c/a), defined as the crack width (2c) over the crack depth (a), was found to be ~ 1.25. This region was basically perpendicular to the stress direction. Contained in this region are finely spaced parallel marks oriented somewhat perpendicular to the crack-growth direction (Figure 4-24c). These marks do not uniformly cover this region, and are especially evident in the outer portions (Figure 4-24a). There is a distinct boundary between the stable growth region and the unstable growth region (Figure 4-24d). Following the stable growth region, and covering the majority of the fracture surface, is the unstable fast-fracture region (Figure 4-24e). This region has a stretched vein morphology, which seems to point back to the crack origin. In the area of the final fracture is a region that has been referred to as a melting region. At a high magnification, distinct melting marks can be seen (Figure 4-24f). Crack-propagation paths were basically perpendicular to the loading axis. However, once unstable fracture reached the neutral axis, the fracture plane was no longer perpendicular to the loading axis. In fact, compression lips were observed (Figure 4-26), similar to those found in brittle ceramic specimens tested under 4PB [161]. Observations of the outside tensile surfaces in the SEM did not reveal any shear-band formation.

5. DISCUSSION

5.1 Monotonic and Cyclic Compression Behavior of a CuZr-based Bulk Metallic Glass

5.1.1 Monotonic Compression

As discussed earlier in Section 2.3.1, the Mohr-Coulomb criterion (Equation 4) can be used to describe yielding [3, 4, 108-110]. The value of α defines the extent to which the normal

stress (σ_θ) influences the effective shear yield stress. It can be shown that the friction coefficient α for compression is given by [4]:

$$\alpha = \left(\frac{\cos(2\theta_c)}{\sin(2\theta_c)} \right) = \cot(2\theta_c) \qquad 14$$

Donovan found experimentally that $\alpha = 0.113 \pm 0.03$ for a Pd-based metallic glass [108], which is consistent with simulations by Schuh et al., who came up with $\alpha = 0.123 \pm 0.004$ for a Cu-Zr model system [111].

Equation 14 clearly shows that θ_c strongly depends on α. For BMGs, the angle of the fracture plane with respect to the loading axis depends on the loading mode. For example, when subjected to tensile loads, the angle (θ_t) that the fracture plane makes with respect to the tensile loading axis, is usually larger than 45° (ranging between 48 and 60°) [162]. Under compressive loading, the value of θ_c is usually less than 45° (between 40 and 44°) [162]. Therefore, the angle of the fracture plane with respect to the loading axis is not the maximum shear stress plane (θ = 45°), as predicted by the von Mises or Tresca criterion [12]. The observed θ_c of 41° for the present $Cu_{45}Zr_{45}Al_5Ag_5$ BMG under monotonic compression is less than the maximum shear stress plane angle and is characteristic of BMGs under monotonic compression. Utilizing Equation 4, the value of α for the present $Cu_{45}Zr_{45}Al_5Ag_5$ BMG is approximately 0.14, in agreement with literature values [4].

For the present $Cu_{45}Zr_{45}Al_5Ag_5$ BMG, the uniaxial compression fracture surface morphology displays a mixture of three distinct patterns: vein-like, river-like, and smooth regions. Commonly, the uniaxial compression fracture surfaces of BMGs only consist of this vein-like structure and is uniformly distributed over the entire fracture surface [4]. This vein-like

structure is attributed to local heating within shear bands [163]. A significant amount of elastic energy is stored in the BMG during deformation as a result of the development of large elastic strains. The elastic energy is released within the highly localized shear bands and dissipated as heat causing local melting [163].

The river-like pattern on uniaxial compression fracture surfaces of BMGs has been observed in prior investigations [153, 164]. It is thought that the presence of the river-like patterns is an indication that the local stress state is comprised of both a normal and a shear component [165]. In fact, the river-like patterns are similar to the fracture surfaces of BMGs loaded in tension [4]. Kusy et al. [153] proposed that the river-like patterns develop because of the "easy separation along the secondary shear bands at the instability prior to failure due to the significant difference between values of critical strain accommodation along perpendicular and parallel direction with respect to the shear band planes". For BMGs with significant plasticity and, thus, a significant amount of secondary shear bands, a large proportion of the fracture surface could consist of the river-like pattern [153]. BMGs with little plasticity develop very few (if any) secondary shear bands, resulting in the absence of the river-like pattern [4]. Since the present $Cu_{45}Zr_{45}Al_5Ag_5$ BMG displays only a small amount of ε_p, the observed small proportion of fracture surface exhibiting the river-like pattern is in agreement this idea.

The smooth regions on uniaxial compressive fracture surfaces have been found previously on BMGs [153] and BMG composites [166]. These smooth regions intermit the vein-like and river-like features, and are thought to be created when a high rate of crack propagation is locally established after overcoming an obstacle (such as a crystalline particle) [166, 167]. Lee et al. [167] performed uniaxial compression tests on various Cu–Zr containing monolithic

amorphous alloys, several of which resulted in significant amounts of plasticity. Microscopic observations of the deformed alloys showed deformation-induced nanocrystallization in the specimens that exhibited the significant plasticity. Jiang et al. [168] attributed their observations of the smooth regions on compressed Cu-Zr-Al monolithic amorphous alloys to deformation-induced nanocrystallization, which could be similar to the present alloy. The development of the smooth regions on the fracture surfaces of present compressed $Cu_{45}Zr_{45}Al_5Ag_5$ BMG could indicate that deformation-induced nanocrystallization occurred. However, no microstructural investigations were performed in this study to verify this feature.

5.1.2. Cyclic Compression

Figure 5-1 gives a general comparison of the S-N behavior of BMGs under cyclic bending[19, 34, 128, 129, 131-133, 169], cyclic tension [7, 29, 30, 135-139], and cyclic compression [29, 38, 137] loading conditions. BMGs seem to give the longest lives, at both high and low stresses, under cyclic compression loading conditions. At lower stresses, cyclic tension loading conditions generally have longer lives than cyclic bending conditions. However, at higher stresses, cyclic tension and cyclic bending conditions appear to be very similar. The σ_L seems to be highest for cyclic compression, followed by cyclic tension and the least being cyclic bending conditions. Under cyclic tension loading, the σ_L/σ_F range from 0.06 [137] up to 0.52 [139]. For cyclic bending, reported σ_L/σ_F values range from 0.08 [19] up to 0.50 [128]. The highest σ_L/σ_F values are from cyclic compression, where the σ_L/σ_F range from 0.45 [38] up to 0.53 [137].

Also included in Figure 5-1 are the results for the present $Cu_{45}Zr_{45}Al_5Ag_5$ BMG alloy. The present alloy possesses remarkable fatigue resistance under cyclic compression. For both

high and low stresses, the present $Cu_{45}Zr_{45}Al_5Ag_5$ BMG displays the longest lifetimes of any BMG system reported in the literature. Moreover, the present alloy also has σ_L/σ_F of 0.76, the highest reported to date for any BMG system under any loading condition.

The cyclic compression fracture surface displays morphology nearly identical to the monotonic compression fracture surface. Specifically, three distinct patterns are distinguishable: (1) vein-like regions, (2) river-like regions, and (3) intermittent smooth regions. Each pattern is thought to develop in a similar manner to that under monotonic compression. The vein-like structure is the result of the release of elastic energy, dissipated as heat, within the highly localized shear bands causing local melting [163]. The river-like patterns are an indication that the stress state locally involves both a normal and a shear component [165]. These smooth regions are thought to be created when a high rate of crack propagation is locally established after overcoming an obstacle (such as a crystalline particle) [166, 167].

Final fracture surfaces of BMGs loaded in cyclic compression are drastically different than those of cyclic tension and/or bending fatigue. Although the overall fracture surface is again relatively flat, failure occurs by unstable fracture in a shear mode (Figure 4-5), with the angle of the fracture plane relative to the loading axis being less than 45°, similar to monotonic compression (Figure 4-2). Albeit there are several observable distinct regions (i.e. vein-like, river-like, and intermittent smooth regions) for the cyclic compression case, they bear little resemblance to the distinct regions (i.e. crack initiation site, crack propagation, unstable fast fracture, and apparent melting regions) found on cyclic tension and/or bending fatigue [22]. However, the final fracture plane is not the fatigue crack propagation plane. The crack propagation plane (Figure 4-10) is normal to the compression axis. The fracture surface

morphology suggests that final failure occurs in a similar manner to monotonic compression. Since fatigue crack propagation occurs perpendicular to the loading direction, it could be possible that the distinct regions do develop during cyclic compression along the crack propagation path. It could just be that the distinct regions were not observed because final failure does not occur along fatigue crack path.

Striation-like features are known to develop during fatigue of BMGs [2]. Although striation-like markings were not seen on the cyclic compression final fracture surfaces in the present study, it could be possible that they developed. Figure 4-10 shows the tip of a fatigue crack inside a specimen at higher magnification. Evident are what appear to be features that are similar to fatigue striations. Rough measurements of these features determined their width to be ~8 μm, in agreement with the "rough" striations on the fatigue fracture surfaces of Zr-based BMGs [17].

Shallow surface pits on the outside surfaces of the present $Cu_{45}Zr_{45}Al_5Ag_5$ BMG led to fatigue damage initiation. Even though the applied stresses in this study are well below the compressive strength ($\sigma_{max} = 0.81 - 0.92)\sigma_{cf}$, stress concentrators, in the form of shallow surface pits on the outside surfaces, can significantly increase the local stresses leading to damage initiation. Utilizing finite element analyses, Cerit et al. [170] developed a stress concentration factor (K_t) for semi-elliptical surface pits:

$$K_t = \frac{[1 + 6.6(a/2c)]}{[1 + 2(a/2c)]} \qquad 15$$

where a is the pit depth and 2c is the pit diameter. Analysis of 12 surface pits in this study found that K_t ranged from 1.2 up to 1.45. For $\sigma_{max} = 0.92\sigma_{cf}$, K_t would need to be at least 1.09,

allowing for easy initiation of fatigue damage. However, for $\sigma_{max} = 0.81\sigma_{cf}$, K_t would need to be at least 1.23, making damage initiation more unlikely.

The relationship between surface crack lengths and the number of fatigue cycles was analyzed, and two types of behaviors were found. A typical example of Type I behavior is shown in Figure 5-2, where the length of a fatigue crack is plotted as a function of fatigue cycles. Fatigue crack length (a) was measured from the defect site at which the crack initiated. Also plotted in Figure 5-2 is the crack growth rate (da/dN) for the measured crack length data as a function of fatigue cycles. It can be clearly seen that the fatigue crack growth is initially high and progressively declines. This type of behavior occurred when "chipped" areas did not develop during the fatigue process.

This crack growth behavior appears to be similar to that which occurs in crystalline metals and alloys [154]. The application of cyclic compressive loads to conventional alloys can result in the propagation of fatigue cracks from stress concentrations (i.e., notch, void, etc.), and will gradually decelerate until it completely arrests. The mechanism by which the fatigue crack propagates is determined by the formation of a cyclic plastic zone of residual tensile stresses ahead of the notch tip. This plastic zone develops upon unloading of the compressive load. Residual tensile stresses are created because there is no crack closure at the notch tip. However, as the length of the fatigue crack increases, the time that the crack remains open decreases, and will ultimately lead to a complete crack arrest. The crack length is a function of several factors, the size of the residual tensile zone, stress state, load range, notch tip geometry, and microscopic roughness of the fatigue crack faces.

Under cyclic tension and bending, the fatigue crack grows under Mode I conditions. Like crystalline alloys, Mode I fatigue crack growth behavior of BMGs can be described by the Paris equation (Equation 5). As shown in Figure 10, stable fatigue crack propagation under cyclic compression occurs under Mode I conditions for the present BMG alloy. Although the effective ΔK cannot be calculated directly due to the unknown stress field around the crack tip, it can be inferred based on equivalent growth rates for BMGs in cyclic tension fatigue [2]. In fact, the growth rates determined in this study are in good agreement with the growth rates found for BMGs in cyclic tension fatigue [2]. For example, the midrange of growth rates for a Zr-based BMG in cyclic tension were found to be 10^{-10} to 10^{-7} m/cycle [2], similar to the growth rates found in this study.

It has been argued [37] that, as the effective driving force (ΔK) responsible for crack advance in cyclic compression progressively decreases with increasing crack length, at the point of crack arrest the damage at the crack tip is equal to or smaller than that corresponding to the long crack threshold stress intensity factor range (ΔK_{th}). The lowest growth rates for Type I behavior (3×10^{-10} m/cycle) are approaching the growth rates ($\sim 10^{-10}$ m/cycle) occurring near ΔK_{th} for BMGs in cyclic tension fatigue [2]. This is further evidence that the mechanism by which the fatigue crack propagates for BMGs in cyclic compression is determined by the formation of a cyclic plastic zone of residual tensile stresses ahead of the notch tip.

A second type of behavior (Type II), one in which chipped areas developed, was observed. Accompanying the chipped areas is multiple crack initiation and bifurcation. A typical example of Type II behavior is shown in Figure 5-3, where the length of a fatigue crack is plotted as a function of fatigue cycles. Fatigue crack length (a) was measured from the defect

site at which the crack initiated. Also plotted in Figure 5-3 is the crack growth rate (da/dN) for the measured crack length data as a function of fatigue cycles. Initially, the crack growth rate would decrease in a similar manner to Type I behavior. However, the formation of a chipped area would result in an increase in the crack growth rate. The data points where chipped areas developed are indicated by a dashed ellipse in Figure 5-3. Moreover, the cracks grew too much longer lengths when compared to cracks not associated with chipped areas (Type I behavior). The formation of the chipped areas results in an increase in the driving force (ΔK) for crack propagation. As a resultμ, the majority of fatigue damage during cyclic compression is associated with the formation of the chipped areas.

It is not exactly clear how the "chipped" areas develop. However, it was noticed that the fracture planes of these chipped areas form $\theta_{chip} = 41°$ with respect to the compression axis (Figure 4-7), suggesting that fatigue crack propagation was not perpendicular to the compression axis very near the surface. Non-perpendicular fatigue crack growth, referred to as "shear lips", has been observed in Al-alloys and some steels [171]. Shear lips can develop where plane stress conditions exist and where the material structure allows for slip near 45° with the plate surface. In this case, plane stress conditions could exist due to the free surface, and the metallic glass could allow for slip in the form of shear bands in a direction 41° to the surface.

The fracture surfaces of these areas are very different from the overall fracture plane. The features found on the overall fracture plane (i.e., vein-like, river-like, and smooth regions) are not seen at all on the chipped fracture surfaces (Figure 5-4). Moreover, the two fracture surfaces are not identical to each other. On one fracture surface (top surface in Figure 5-4), many ridge-like features, perpendicular to the crack propagation direction, are present on the

chipped fracture surfaces. The fatigue crack growth mechanisms (development of striations) for shear lips are thought to be the same as in mode I fatigue crack growth [171]. It could be that these ridge-like markings are similar to the striation-like markings seen on BMGs subjected to cyclic tension [2]. The bottom surface in Figure 5-4 does not clearly exhibit the ridge-like marks. It has features that are commonly found when rubbing or sliding of two crack faces occur. The fact that the two faces show two different types of features suggests that two different fracture processes occurred.

Figure 5-5 schematically illustrates the development of the fatigue damage during cyclic compression for this BMG. Damage first initiates as a shear band or mixed-mode crack and propagates at an angle < 45° to the compression axis (Figure 5-5a). Cracks change orientation and begin propagating in a direction normal to the compression axis (Figure 5-5b). However, very near the surface, the cracks propagate in a direction that is not normal to the compression axis. It is suggested that these could be similar to shear lips due the plane stress condition near the surface. With further cyclic loading, the cracks continue to propagate in a direction normal to the compression axis (Figure 5-5c). In the area adjacent to the non-perpendicular crack propagation, shear bands and small cracks begin to develop due to rubbing and sliding of the crack faces. It could be that small debris form, resulting in a wedging effect that causes material to be chipped off. The fracture plane where stable non-perpendicular crack growth occurred exhibits ridge-like markings on the surface. The fracture plane where shear bands and small cracks develop do not form the ridge-like marks. With further cyclic loading, cracks continue to propagate, but at an ever decreasing rate due to the decrease in the driving force for crack propagation. Chipped areas can continue to develop as well.

Zhang et al. [29] proposed the concept of a "surface damage layer" to explain how final failure occurs during cyclic compression of BMGs, and appears to be in agreement with this study. During the CC cyclic loading process, a "surface damage layer" develops, which consists of shear bands, fatigue cracks, and the areas of chipping, and is a thin layer of material near the outside portions of the sample. As cyclic loading progresses, the surface damage layer develops and propagates inward, decreasing the effective area that can support the load. Zhang et al. suggested that, when the effective area becomes so small that the load can no longer be supported, failure occurs. Hence, fatigue damage during cyclic compression is distributed over the entire specimen surface rather than being localized in one dominant fatigue crack, as is the case for BMGs under cyclic tension or bending. Final failure of BMGs under cyclic compression occurs in a pure shear mode (Figure 5-6). The fracture plane is not on a plane of stable fatigue crack propagation, but rather is inclined at an angle $< 45°$ to the compression axis.

During cyclic compression of BMGs, cracks initiate and propagate. However, with further cyclic loading the cracks continue to propagate, but at an ever decreasing rate until presumably complete crack arrest. This is due to a decrease in the driving force (ΔK) for crack propagation. Due to the decrease in the crack propagation rate, the crack may not grow to a critical length that would result in failure. Therefore, in order for failure to occur, many cracks would need to develop and propagate under cyclic compression. It is thought that this is the reason for the longer fatigue lives found for BMGs when subjected to the cyclic compression loading mode.

5.2 Effect of Specimen Size on the Monotonic and Cyclic Compression Behavior of a Bulk Metallic Glass

5.2.1. Monotonic Deformation

As discussed earlier, Donovan [108] proposed that the Mohr-Coulomb criterion (Equation 4) to describe yielding of metallic glasses. The Mohr-Coulomb criterion has been supported by many studies [3, 4, 109, 110]. The observed θ_c of 42° for the present $(Zr_{53}Cu_{30}Ni_9Al_8)_{99.5}Si_{0.5}$ BMG under monotonic compression is less than the maximum shear stress plane angle and is characteristic of metallic glasses under monotonic compression. Utilizing Equation 14, the friction coefficient α for the present $(Zr_{53}Cu_{30}Ni_9Al_8)_{99.5}Si_{0.5}$ BMG is approximately 0.105, in reasonable agreement with literature values [4].

Free volume in a metallic glass is essentially "extra" volume, relative to a fully dense glass structure, that is frozen into the atomic structure and allows physical space for atomic movement under mechanical loading [39-41]. At high stress and low temperatures, plastic flow in metallic glasses is believed to occur via a diffusional process involving the rearrangement of a small number of atoms and their surrounding free volume [39-41]. The ability of a region to undergo this rearrangement depends on the local atomic density, i.e., the amount of free volume.

It has been shown that the amount of free volume in a metallic glass has significant effect on its ductility. Murali et al. [42] found that annealing a metallic glass below T_g can result in severe embrittlement. They concluded that a decrease in free volume was the fundamental cause for the embrittlement. Moreover, by minor alloying additions of Ti to a CuZrAl BMG, Chen et al. [43] were able to significantly increase the compressive plasticity. The increase in plasticity was attributed to an increase in free volume as a result of the minor alloying additions.

The amount of free volume is in a metallic glass depends on the cooling rate from a fixed temperature. Rehmet et al. [44] found that the amount of free volume increases with an increase in cooling rate. Moreover, near surface softening was found for a $Zr_{50}Cu_{50}$ BMG [172]. The softening was attributed to structural changes taking place as a result of changes in cooling rates. The effect of cooling rate on the ductility of a TiCu-based BMG was recently investigated [173]. The ductility of the BMG increased with increasing cooling rate and an accompanying increase in free volume.

It is expected that the cooling rate for a given composition will increase with a decrease in the specimen as-cast size (d) [45]. Therefore, it would be reasonable to assume that the free volume content would increase (as well as the ductility) with a decrease in specimen as-cast size. This trend of an increase in free volume (and ductility) with a decrease in specimen as-cast size has been observed previously [117]. Huang et al. found that for a Ti-based BMG alloy, the as-cast sample with a smaller size exhibits a larger compressive plasticity. The smaller as-cast sample had more visible shear bands and a higher shear band density. The observed increase in plasticity was attributed to an increase in free volume. The smaller samples with higher free volume could more easily initiate new shear bands, resulting in an increase in visible shear bands and plasticity.

BMGs contain varying amounts of free volume that is frozen in during solidification. DSC is one method that is utilized to characterize the structural relaxation that is related to the free volume in BMGs. In a DSC thermogram, the exothermic reaction just below T_g is the result of the annihilation of free volume and structural relaxation. The exothermic heat is proportional to the amount of the free volume that escapes [174] according to the equation:

$$(\Delta H)_{fv} = \beta' \Delta v_f \quad 16$$

where β' is a constant and Δv_f is the change of free volume per atomic volume. From Figure 4-11, it is apparent that exothermic heat for the 4 mm sample is significantly less than that for the 2 mm sample. This suggests that the 4 mm sample contains less free volume than the 2 mm sample. This is the result of the higher cooling rate during the solidification of the 2 mm sample. The higher cooling rate suppresses the escape of the free volume. However, a quantitative distinction of the free volume in the 2 and 4 mm samples was not done in this study. Nevertheless, a qualitative difference is clearly observed as a result of the different cooling rates experienced by the 2 and 4 mm samples.

The development of a small amount of plasticity during monotonic compression for the 2 mm samples and essentially none for 4 mm samples could be attributed to the faster cooling rate experienced by the 2 mm samples during solidification. As just mentioned, a higher cooling rate results in more free volume compared to a slower cooling rate. The DSC results show that the 2 mm samples have more free volume when compared to the 4 mm samples.

There are basically two ways in which free volume can effect the plasticity of BMGs. First, when the free volume is higher, the atomic mobility is higher due to a lower viscosity. The higher atomic mobility makes stress relaxation by viscoplastic flow easier at the crack tip. This provides a resistance to crack extension and results in an increase of the critical shear displacement required for fracture. Second, a larger amount of free volume increases the ability of the BMG to under shear banding and branching. The SEM observations of the shear band density agree well with these ideas. Moreover, the size of the plastic zone at the crack tip increases. This is reflected by the fracture morphology for the 2 and 4 mm samples. The 2 mm

sample seems to have somewhat of a finer vein pattern when compared to the of the 4 mm sample.

5.2.2. Cyclic Compression

The 4 mm sample appears to behave in a similar manner to the CuZr-based BMG discussed earlier. Cracks propagate in a direction normal to the compression axis. However, very near the surface, the cracks propagate in a direction that is not normal to the compression axis. Chipped areas develop due to the rubbing and sliding of the non-perpendicular crack growth. With further cyclic loading, cracks continue to propagate, but presumably at an ever decreasing rate due to the decrease in the driving force for crack propagation. Due to the decrease in the crack propagation rate, the crack may not grow to a critical length that would result in failure. Therefore, in order for failure to occur, many cracks would need to develop and propagate under cyclic compression.

The potential effects of free volume on the fatigue lifetimes of BMGs have only been investigated in a few studies, and the results are conflicting. Yokoyama et al. [46] studied how small additions of Pd to a ZrCuAl BMG effect the rotating-beam fatigue behavior. They found that the fatigue lives and σ_L were the highest for 3 % (atomic) Pd. In addition, Yokoyama et al. [46] also studied how small additions of Pd affected the free volume, and found that the free volume increase was the highest for 3 % Pd. The improved fatigue performance was attributed to a relaxation of the stress around the crack tip. However, it should be noted that a nanostructure also developed at 3 % Pd. Wang et al. [175] found similar results for TT fatigue.

In another study, Launey et al. [134] found that, in contrast to the work of Yokoyama et al. [46] and Wang et al. [175], σ_L under cyclic bending was higher for the BMG alloy with less

free volume. This was attributed to a slower cooling rate for the material showing the highest σ_L. Launey et al. [47] also found that the free volume content does not have an influence on da/dN or ΔK_{th}. Based on these findings, they concluded that the free volume only effects the crack initiation portion of the fatigue lifetimes. Since fatigue cracks initiate from shear bands, a larger amount of free volume would allow easier deformation and easier formation of slip bands, leading to faster crack initiation.

The effects of free volume of the fatigue behavior of BMGs under cyclic compression appear somewhat different than that under other loading modes (i.e., cyclic tension or bending). It is thought that initially, for both 2 and 4 mm samples, shear bands should preferably nucleate at weaker locations, such as casting defects and/or surface flaws. With further cyclic loading, new areas are needed for further strain accommodation. Since the 2 mm sample contains more free volume than the 4 mm sample, there are many more potential locations for easy shear band nucleation. So, rather than for fatigue cracks to develop and propagate, it is easier for shear bands to develop in the alloy with a higher free volume (Figures 16b and 17b). Thus, there is a reduction in the fatigue crack driving force (ΔK) because of the development of many shear bands. This could lead to an increase in the number of cycles required to cause failure for the material with higher free volume.

The fatigue failure of crystalline metals and alloys is dependent on the interaction of a large stress with a critical flaw. Fatigue is controlled by the weakest link of the material, and the probability of finding a weak link increases with increasing the material volume. In bending and axial loading, larger specimens have a higher probability of microstructural discontinuities in the highly stressed surface regions that contribute to the decrease in fatigue resistance. However, the

fatigue limit for crystalline metals and alloys in axial loading is usually lower than the bending fatigue limits. In bending, for a given nominal stress, the stress gradient depends upon the specimen's thickness. The larger the thickness, the smaller the bending stress gradient and hence the larger the average stress in a local region on the surface. The average stress in the local region, rather than the maximum stress, may be the governing stress for fatigue. For axial loaded unnotched specimens, a nominal stress gradient does not exist, and the average and maximum nominal stress have the same magnitude, resulting in less size effect than in bending.

In addition to the effect of the as-cast specimen size and the free volume content on the fatigue behavior, there could also be another size effect that could potentially be at play. When d is decreased from 4 mm down to 2 mm, the volume or surface will decrease. Since most fatigue damage initiates from the surface, it should expected that decreasing the surface area will reduce the chances of finding a surface defect that could result in fatigue damage initiation.

5.3 Effect of a Confined Geometry on the Monotonic and Cyclic Compression Behavior of a Bulk Metallic Glass

5.3.1. Monotonic Compression

The present results on the monotonic compression of low aspect ratio BMGs are similar to previous works [55, 56, 58]. The specimen geometry of BMGs can significantly affect their demonstration of ductility in compression. Jiang et al. [55] concluded that when the aspect ratio was larger than 0.75, failure occurred catastrophically with very little plasticity. When the aspect ratio was smaller than 0.75, substantial plastic deformation occurred. In fact, Jiang et al. [55] demonstrated 76.4% ε_p for a Zr-based BMG with an aspect ratio of 0.5. In this study, the specimens with an aspect ratio of 2 displayed very little plasticity. However, when the aspect ratio was reduced to 0.5, significant plasticity up 35% was promoted. This is in agreement with

the results of Jiang et al.[55]. Moreover, Bei et al. [56] developed a "deformation map" showing the combined effects of aspect ratio and strain rate on ε_p. In this study, a strain rate of 3×10^{-4} s^{-1} was employed for both aspect ratios. The current test conditions and ε_p demonstrated are in very good agreement with the deformation map of Bei et al. [56].

The reason for the observed increase in ductility has been addressed in a number of studies [55, 58, 59]. During monotonic compression, there is a uniaxial stress, σ, which is parallel to the loading direction. In addition to σ, there is also a lateral stress σ_L perpendicular to the loading direction. This stress is generated by friction between the upper and lower specimen surfaces and the platen. When the aspect ratio is large (Figure 5-7a), σ_f acts only close to the upper and lower surfaces of the specimen near the interface with the platen. In this situation, σ_f has very small effect on the deformation characteristics. The shear bands are free to operate without any barriers. Thus, the yield strength and ε_p to failure will not significantly be effected.

When the aspect ratio is small (Figure 5-7b), σ_f is believed to play a significant role in the deformation process. The primary shear bands develop but their continued propagation is hindered by the platens at the top and bottom surfaces of the specimen and the frictional stress σ_f. The interaction of the uniaxial stress σ, the platens, and σ_f produce a hydrostatic state of stress for samples with an aspect ratio of 0.5. The hydrostatic stress acts more homogeneously on the specimen. This could result in shear band multiplication and branching. As the load is increased, the density of the shear bands increases, resulting in a high compressive plasticity. Moreover, the hydrostatic state of stress could account for the observed decrease in E when the aspect ratio is 0.5.

When the aspect ratio is large, it is usually proposed that the Mohr-Coulomb criterion (Equation 13) can describe the fracture process. The observed θ_c of 42° when the aspect ratio is 2 is characteristic of BMGs under monotonic compression. Utilizing Equation 4, the friction coefficient α when the aspect ratio is 2 is approximately 0.105, in reasonable agreement with literature values [4].

The primary shear band angle observed on the surfaces when the aspect ratio was 0.5 was measured to be 49°. This is larger than the angle predicted by the Mohr-Coulomb criterion. A similar fracture mode was observed by Zhang et al. [176] for Ti-based composites. The deviation from the angle predicted by the Mohr-Coulomb criterion was explained by the rotation of the primary shear bands as a result of high compressive ε_p [176]. The deviation can be described by:

$$\sin\left(\theta_C^O\right) = \sqrt{1-\varepsilon_P}\,\sin(\theta_C^F) \qquad 17$$

where θ_C^O is the initial shear band angle and θ_C^F is the final measured shear band angle after rotation. Using this relationship, it is possible to estimate θ_C^O using the known values of θ_C^F and ε_P. Inserting θ_C^F = 49° and a compressive ε_P = 29%, the resulting value for θ_C^O is 41.6°. This value is very close to the angle found when the aspect ratio was 2 and that predicted by the Mohr-Coulomb criterion.

5.3.2. Cyclic Compression

In general, σ_L for conventional engineering alloys is expected to increase with increasing strength [154]. The σ_F when the aspect ratio was 0.5 was much higher (ranging from 2,500 up to 3,750 MPa) than σ_F for an aspect ratio of 2 (1,705 MPa). This considerable increase in σ_F could,

at least in part, explain the observed increase in σ_L when the aspect ratio is 0.5. Moreover, since σ_F varies greatly when the aspect ratio is 0.5, it seems reasonable to expect that σ_L would vary in a similar manner.

When the aspect ratio is 2, the fatigue behavior of the Zr-based BMG in this study appears to be similar to that for the CuZr-based BMG discussed previously. For BMGs with larger aspect ratios, fracture under cyclic compression occurs in a pure shear mode. The final fracture plane forms an angle respect to the loading axis that is similar to the monotonic compressive fracture plane (Figure 4-17a). The cyclic compression fracture surface displays morphology nearly identical to the monotonic compression fracture surface (Figure 4-17c). On the outside surfaces, shear bands and/or cracks are commonly observed (Figure 4-17b). In addition, the cyclic compressive loading can cause areas of "chipping" on the outside surfaces, which is not found with monotonic compression (Figures 4-17b and 4-17d).

During cyclic compression of BMGs with larger aspect ratios, cracks initiate and propagate. However, with further cyclic loading the cracks continue to propagate, but at an ever decreasing rate until presumably complete crack arrest. This is due to a decrease in the driving force (ΔK) for crack propagation. Due to the decrease in the crack propagation rate, the crack may not grow to a critical length that would result in failure. Therefore, in order for failure to occur, many cracks would need to develop and propagate under cyclic compression.

When cyclic compressive loads are applied to BMGs with smaller aspect ratios, a different behavior occurs. When the aspect ratio was 0.5, the samples fractured into several small fragments (Figure 4-21a), which is analogous to the monotonic compressive fracture. Many shear bands and/or cracks were visible on the outside surfaces of the small fragments

(Figure 4-21b), much more so than when the aspect ratio was 2. However, the majority of the shear bands and/or cracks were oriented basically perpendicular to the loading direction, very similar to when the aspect ratio is 2. It is believed that residual tensile stresses control fatigue crack propagation of BMGs under cyclic compression [177], which could result in the development of mode I crack growth.

It appears that the when the aspect ratio is small (0.5), the hydrostatic stress state produced from the interaction of the uniaxial stress σ, the platens, and σ_f again play a significant role during he fatigue damage process. Shear bands and/or cracks develop in a manner similar to the when the aspect ratio is 2. However, when the aspect ratio is 2, the hydrostatic stress state is not significantly effect the fatigue process. The shear bands and/or cracks growth is not suppressed by the hydrostatic stress state and can propagate freely. In contrast, when the aspect ratio is small, the shear bands and/or cracks are suppressed by the hydrostatic stress state, restricting their individual growth and development. This in turn causes the development of many new shear bands and/or cracks in order to accommodate the cyclic compressive loads. This prevents any previously formed shear band and/or cracks from reaching a critical size. This results in longer fatigue lives when the aspect ratio is small.

When the aspect ratio is larger, the shear band and/or crack growth under cyclic compression is not suppressed by the hydrostatic stress state and can propagate freely. Therefore, final failure occurs in a shear mode and can be described by the Mohr-Coulomb criterion. However, when the aspect ratio is small, shear band and/or crack growth under cyclic compression is suppressed by the hydrostatic stress state and cannot propagate freely. As a result many shear bands and/or cracks can develop and interact inside the BMGs. This results in

fragmentation at the moment of final failure, with many fracture planes developing. Thus, final failure cannot be described by the Mohr-Coulomb criterion.

5.4 Cyclic Bending Behavior of a Cu-based Bulk Metallic Glass

The fatigue lifetimes were found to be higher for 3PB conditions at all σ_R tested. This result should be expected when the stress distributions for each load condition is considered (Figure 5-8). The maximum stress for 4PB is given by

$$\sigma_{\max} = \frac{3Pa}{bh^2} \tag{18}$$

where a is the distance from the outer to inner loading points, P is the applied load, b is the beam width, and h is the beam height. This maximum stress is experienced over the entire outermost tensile surface in the region between the two inner loading points. For the case of 3PB, the maximum stress is given by

$$\sigma_{\max} = \frac{1.5PL}{bh^2} \tag{19}$$

where L is the span between the outer loading points. This maximum stress is only experienced at the center of the beam at the outermost tensile surface. Consequently, the volume of material experiencing the maximum stress is much greater for 4PB. Thus, longer fatigue lives would be expected for the 3PB case.

Some recent studies of the fatigue behavior of Zr-based BMGs [22-27] have reported σ_L/σ_F to be as high as ~ 0.50 for notched cylindrical bars loaded in $_{TT}$. However, other studies have reported σ_L/σ_F to be as low as ~ 0.09 [19] for similar BMG materials loaded in 4PB conditions. To account for this large difference, it has been proposed that sampling volume plays a major role in determining the fatigue-endurance limit of BMGs [24, 34]. The greater the

test volume is, the smaller the fatigue-endurance limits will be. This idea seems to be supported by the results presented here. The sampling volume for 4PB conditions is much greater when compared to that of 3-point loading conditions. Accordingly, it is likely that the 4PB endurance limit will be smaller than that of 3PB.

The stable crack-growth region had a thumbnail shape appearance and an aspect ratio of ~ 1.25. Using numerical stress-intensity solutions for semi-elliptical surface and quarter-elliptical corner cracks developed by Newman and Raju [178], the stress intensity factor, K, was calculated from the following equation

$$K = (H_c S_b)\sqrt{\pi\left(\frac{a}{Q}\right)}F\left(\frac{a}{c},\frac{a}{t},\frac{c}{b},\phi\right) \qquad 20$$

where H_c is the bending multiplier, S_b is the maximum stress, Q is the shape factor, F is the boundary-correction factor, a is the depth of the crack, c is the half length of the crack, t is the thickness, b is the width, and ϕ is the parametric angle of the ellipse with the unit deg. From the above equation, the apparent fracture-toughness was calculated and found to be ~ 14 - 15 MPa$\sqrt{m}$ for both 3PB and 4PB. This value is comparable to those previously reported for a $Zr_{41.25}Ti_{13.75}Cu_{12.5}Ni_{10}Be_{22.5}$ BMG studied under 4PB conditions, which had a value of 15 MPa$\sqrt{m}$. For the $(Zr_{58}Ni_{13.6}Cu_{18}Al_{10.4})_{99}Nb_1$ BMG shown in Figure 4-23, apparent fracture toughness values ranging from 26-40 MPa$\sqrt{m}$ were reported [35] for 4PB conditions. However, the $(Zr_{58}Ni_{13.6}Cu_{18}Al_{10.4})_{99}Nb_1$ BMG contained some nanocrystalline particles [35]. These nanocrystalline particles could improve the fracture toughness.

Found in the stable crack-growth region are finely spaced parallel marks (Figure 4-25c), similar to fatigue striations, oriented somewhat perpendicular to the crack-growth direction. This

striation-like morphology has been reported previously [2, 19, 22-25, 28-30, 32, 34, 35] on the fatigue fracture surfaces of Zr-based BMGs, and are thought to form via a mechanism similar to that which occurs in crystalline alloys, involving the repetitive blunting and resharpening of the crack tip. These striation-like marks were visible over the entire region. However, during the early stages of stable crack growth, the marks do not uniformly cover the entire crack front [Figure 4-25a], and are broken up into many places. Therefore, the crack front probably does not grow uniformly during the early stages of crack growth. However, it seems that once the crack reaches a critical size, the marks uniformly cover the entire outer region [Figure 4-25a]. Therefore, it appears that uniform growth of the crack front occurs during the latter stages of stable crack growth.

The spacings of these striation-like marks were measured as a function of the crack depth for several samples. A typical spacing measurement is shown in Figure 4-25c, indicated by the spacing between two arrows. The results were plotted in Figure 5-9 against the corresponding stress-intensity-factor range, ΔK, normalized by the E. Note that each data point represents the average of many striation measurements. The stress intensity factor range was calculated from the numerical stress intensity solutions developed by Newman and Raju [178]. Spacings were found to increase as ΔK increased. Note the striation spacing can be rationalized by ΔK, regardless of stress levels.

Also plotted in Figure 5-9 for comparative purposes is the relationship developed by Bates and Clark [179]. They found that, for the alloys tested (two aluminum alloys, one titanium alloy, and three steels), the striation spacings in the fatigue fracture surfaces is related to the

parameter, ΔK/E, by a single, linear, relatively narrow band. Thus, they concluded that ΔK for any crystalline metallic alloy could be estimated with the aid of the empirical relation

$$\text{Striation Spacing} \approx 6\left(\frac{\Delta K}{E}\right)^2 \qquad 21$$

Using this relationship, and with reasonable reliability, estimates of stress intensity, and ultimately the stress conditions which caused failure, can be obtained. This relation assumes that each striation represents the incremental advance of the crack front as a result of one loading cycle and that the extent of this advance varies with the σ_R. By fitting the data, the relation for the present alloy was found to be

$$\text{Striation Spacing} \approx 0.3467\left(\frac{\Delta K}{E}\right)^{1.127} \qquad 22$$

As can be seen in Figure 5-9, the Bates and Clark relation underestimates the spacing for BMGs. This trend suggests that there must be an accumulation of damage necessary ahead of the crack that occurs over many cycles, which causes the crack to jump suddenly, similar to the formation of discontinuous growth bands found on fatigue fracture surfaces of many polymer materials.

Looking closer at Figure 4-25c, even finer parallel marks can be seen between the two arrows. Crude measurements of these finer marks show that they have spacings in the range of ~ 0.1 μm to ~ 0.3 μm, which is closer to typical striation spacings of conventional crystalline alloys. In fact, when plotted against ΔK/E, the data falls closer to the Bates and Clark relation. Wang et al. [17] However, these spacings were difficult to measure accurately, and were not clearly evident in many areas. Future work will examine this further.

The unstable fast-fracture region (Figure 4-25e) covers the majority of the fracture surface. A Chevron-type pattern is observed in this region, which seems to point back toward

the crack origin. At higher magnifications, a vein-like morphology is observed, which is similar to tensile fracture surfaces [29, 30, 33]. This trend indicates that the temperature rise due to the release of stored elastic energy could be high enough to melt the glass locally. However, no evidence of a vein-like structure is observed in the stable crack-growth region, which means the temperature rise during this stage is too low to melt the glass. Moreover, in the melting region, the vein-like morphology and droplets are clearly visible [Figure 4-25f], evidence that the temperature rise is high at the moment of the final fracture. This type of feature has also been seen on the fatigue fracture surfaces of several Zr-based BMGs [22-24, 35].

Observations of the present material in the SEM did not reveal the formation of shear banding on the tensile surfaces. The presence of defects, such as gas pores or surface trenches, could have locally raised the stress to a level high enough that cracks easily formed without the formation of shear bands. A similar type of crack-initiation mechanism has been observed before in a Zr-based BMG [24]. Wang et al. did not find shear bands on the surface of notched samples tested in TT fatigue. Casting defects, such as porosities and oxide inclusions, were present in the material. The presence of these defects locally raised the stress high enough so that cracks could easily initiate from these defects without the formation of shear bands.

It is well known that in crystalline alloys, fatigue damage initiates at heterogeneous nucleation sites found within the material. The heterogeneous nucleation sites could be preexistent, such as inclusions or gas porosities, or could be generated during the cyclic-straining process itself (slip bands). Fatigue deformation in BMGs is usually associated with shear band formation. Cyclic loading normally initiates shear band formation at local sites where stress concentrations exist. The shear bands are weak sites in the material, and, as cyclic loading

continues, fatigue cracks will develop from these shear bands. Indeed, this type of deformation mechanism has been observed on the tensile surface of 4PB fatigued Zr-based BMGs [34, 35]. However, because of the presence of defects that are of sufficient size which could significantly raise the stress locally, fatigue cracks initiated without the formation of shear bands. If no defects, such as gas pores or surface trenches, were present that could raise the stress locally, it is thought that shear bands could form in the present material. The formation of shear bands could result in improved fatigue behavior and longer lifetimes. Thus, processing conditions of BMGs is critical for fatigue performance.

Based on the present results and observations in the SEM, a fatigue-damage mechanism for this material is proposed. During cyclic loading, cracks initiate from defects or flaws located on or just below the tensile surface [Figure 4-25b]. These stress concentrators could have locally raised the stress level high enough so that shear band formation was avoided all together. As cyclic loading continues, the crack then propagates perpendicular to the stress direction [Figure 4-25a]. No vein pattern is formed during this stage, indicative that the temperature rise is too low to locally melt the material. Striations are formed during the crack-propagation process [Figure 4-25c]. However, the striations are broken up and do not uniformly cover the propagation path, meaning that crack growth is not uniform during the early stages [Figure 4-25a]. At a critical crack size, the striations begin to cover the crack-growth region completely, and crack growth occurs uniformly along the crack front. There is a clear transition from the crack propagation to unstable fast fracture, creating a stretched vein pattern [Figure 4-25d]. The temperature during this stage could be high enough to melt the glass locally. At the moment of

final fracture, the temperature rise is large and melts the glass, leaving behind the characteristic melting droplets and vein pattern [Figure 4-25f].

6. CONCLUSIONS

6.1. Monotonic and Cyclic Compression Behavior of a CuZr-based Bulk Metallic Glass

Fracture under monotonic compression occurred in a pure shear mode. The fracture surface forms an θ_C of 41° with respect to the compressive loading axis. The uniaxial compression The fracture surface is relatively flat and displays a mixture of three distinct patterns: (1) vein-like, (2) river-like, and (3) smooth regions.

The present $Cu_{45}Zr_{45}Al_5Ag_5$ BMG was found to a fatigue-endurance limit of at least 1,418 MPa and $\sigma_L/\sigma_F = 0.77$, which are the highest values reported to date. Fracture under cyclic compression occurred in a pure shear mode. The fracture surface forms an angle of 41° with respect to the loading axis. This angle is similar to the monotonic compressive fracture angle for the present BMG. The cyclic compression fracture surface displays morphology nearly identical to the monotonic compression fracture surface. Specifically, three distinct patterns are distinguishable: (1) vein-like regions, (2) river-like regions, and (3) intermittent smooth regions. Each pattern is thought to develop in a similar manner to that under monotonic compression.

On the outside surfaces of the fatigue specimens, many shear bands and cracks were observed. In addition, the cyclic compressive loading caused areas of "chipping" on the outside surfaces. This type of feature was not observed on the monotonic compression outside surfaces.

Under cyclic compression, damage first initiates as a shear band or mixed-mode crack and propagates at an angle < 45° to the compression axis. Inside the specimen, cracks propagate in a direction normal to the compression axis. However, very near the surface, the cracks

propagate in a direction that is not normal to the compression axis. Chipped areas develop due to the rubbing and sliding or non-perpendicular crack growth. With further cyclic loading, cracks continue to propagate, but at an ever decreasing rate due to the decrease in the driving force for crack propagation.

Final failure occurs due to the development of the "surface damage layer". Fatigue damage during cyclic compression is distributed over the entire specimen surface rather than being localized in one dominant fatigue crack.

6.2. Effect of Specimen Size on the Monotonic and Cyclic Compression Behavior of a Bulk Metallic Glass

The as-cast specimen size, cooling rate, and thus the free volume content was found to significantly effect the monotonic compression and cyclic compression behavior of a Zr-based BMG. The smaller samples (2 mm) experienced a faster cooling rate, resulting in a higher free volume content when compared to the larger samples (4 mm). The 2 mm samples displayed superior monotonic compression and cyclic compression properties. During monotonic compression, the higher free volume allows for easy shear band formation resulting in higher plasticity. The smaller samples also resulted in a significant increase in σ_L. This trend was attributed again to a higher free volume content. Rather than for fatigue cracks to develop and propagate, it is easier for shear bands to develop in the alloy with a higher free volume. Thus, there is a reduction in the fatigue crack driving force (ΔK) because of the development of many shear bands. This could lead to increase in the number of cycles required to cause failure for the material with higher free volume.

6.3. Effect of a Confined Geometry on the Monotonic and Cyclic Compression Behavior of a Bulk Metallic Glass

The sample geometry was found to have a dramatic effect on the monotonic compressive and cyclic compressive behavior of a Zr-based BMG. Under monotonic compression, a smaller aspect ratio resulted in higher yield strengths and significant amounts of ε_p when compared to those with a larger aspect ratio. Under cyclic compressive loads, a smaller aspect ratio resulted in a higher σ_L and longer fatigue lives overall. The dramatic effect of sample aspect ratio was attributed to the development of a hydrostatic stress state from the interaction of the uniaxial applied load and the friction stress developed at the interface of the top and bottom specimen surfaces and the platens. Shear band and/or crack growth and development was suppressed, resulting in the improved monotonic compressive and cyclic compressive properties. The beneficial effects of the sample geometry on the mechanical behavior of BMGs should be utilized in such applications as thin films or thin discs for micromachines.

6.4. Cyclic Bending Behavior of a Cu-based Bulk Metallic Glass

The fatigue lives and σ_L were greater for 3PB conditions when compared to that of 4PB conditions. The σ_L, based on the applied σ_R, for 3PB and 4PB conditions were approximately 475 MPa and 350 MPa, respectively. This result can be attributed to the smaller sampling volume for the 3PB condition. The fracture surfaces consisted of 4 main regions: a crack-initiation site, a stable crack-growth region, an unstable fast-fracture region, and a melting region. Finely spaced parallel marks oriented somewhat perpendicular to the direction of crack propagation were observed, though not uniformly, in the stable crack-growth region. Analyses of these marks found that their spacing increased with increasing ΔK. The Bates and Clark relation underestimates the striation spacing, indicating that there must be an accumulation of

damage necessary ahead of the crack that occurs over many cycles which causes the crack to jump suddenly. Fatigue damage in the form of cracks initiates from stress concentrators, and shear band formation is avoided altogether. Cracks then propagate until the final failure occurs. Thus, processing conditions for BMGs are critical, since shear band formation could result in improved fatigue performance,

REFERENCES

[1] C. A. Schuh, T. C. Hufnagel and U. Ramamurty, Acta Mater. 55 (2007) 4067.

[2] C. J. Gilbert, V. Schroeder and R. O. Ritchie, Metall. Mater. Trans. A-Phys. Metall. Mater. Sci. 30 (1999) 1739.

[3] C. T. Liu, L. Heatherly, D. S. Easton, C. A. Carmichael, J. H. Schneibel, C. H. Chen, J. L. Wright, M. H. Yoo, J. A. Horton and A. Inoue, Metallurgical and Materials Transactions a-Physical Metallurgy and Materials Science 29A (1998) 1811.

[4] Z. F. Zhang, J. Eckert and L. Schultz, Acta Mater. 51 (2003) 1167.

[5] C. J. Gilbert, R. O. Ritchie and W. L. Johnson, Appl. Phys. Lett. 71 (1997) 476.

[6] Y. K. Xu, H. Ma, J. Xu and E. Ma, Acta Mater. 53 (2005) 1857.

[7] W. H. Peter, P. K. Liaw, R. A. Buchanan, C. T. Liu, C. R. Brooks, J. A. Horton, C. A. Carmichael and J. L. Wright, Intermetallics 10 (2002) 1125.

[8] X. K. Xi, D. Q. Zhao, M. X. Pan, W. H. Wang, Y. Wu and J. J. Lewandowski, Phys. Rev. Lett. 94 (2005) 4.

[9] B. C. Menzel and R. H. Dauskardt, Scr. Mater. 55 (2006) 601.

[10] B. C. Menzel and R. H. Dauskardt, Scr. Mater. 57 (2007) 69.

[11] G. Y. Wang, J. D. Landes, A. Peker and P. K. Liaw, Scr. Mater. 57 (2007) 65.

[12] T. H. Courtney, Mechanical Behavior of Materials (McGraw-Hill, New York, NY, 2000).

[13] H. Q. Li, C. Fan, K. X. Tao, H. Choo and P. K. Liaw, Adv. Mater. 18 (2006) 752.

[14] C. Fan, P. K. Liaw, V. Haas, J. J. Wall, H. Choo, A. Inoue and C. T. Liu, Phys. Rev. B 74 (2006) 6.

[15] H. Q. Li, K. X. Tao, C. Fan, P. K. Liaw and H. Choo, Appl. Phys. Lett. 89 (2006) 3.

[16] W. H. Jiang, F. X. Liu, D. C. Qiao, H. Choo and P. K. Liaw, Journal of Materials Research 21 (2006) 1570.

[17] G. Y. Wang, P. K. Liaw, Y. Yokoyama, A. Inoue and C. T. Liu, Mater. Sci. Eng. A-Struct. Mater. Prop. Microstruct. Process. 494 (2008) 314.

[18] R. Hertzberg, Deformation and Fracture Mechanics of Engineering Materials (Wiley, Hoboken, NJ, 1996).

[19] C. J. Gilbert, J. M. Lippmann and R. O. Ritchie, Scr. Mater. 38 (1998) 537.

[20] K. M. Flores and R. H. Dauskardt, Intermetallics 12 (2004) 1025.

[21] K. M. Flores, W. L. Johnson and R. H. Dauskardt, Scr. Mater. 49 (2003) 1181.

[22] G. Y. Wang, P. K. Liaw, W. H. Peter, B. Yang, Y. Yokoyama, M. L. Benson, B. A. Green, M. J. Kirkham, S. A. White, T. A. Saleh, R. L. McDaniels, R. V. Steward, R. A. Buchanan, C. T. Liu and C. R. Brooks, (2004) p. 885.

[23] G. Y. Wang, P. K. Liaw, W. H. Peter, B. Yang, M. Freels, Y. Yokoyama, M. L. Benson, B. A. Green, T. A. Saleh, R. L. McDaniels, R. V. Steward, R. A. Buchanan, C. T. Liu and C. R. Brooks, (2004) p. 1219.

[24] G. Y. Wang, P. K. Liaw, A. Peker, B. Yang, M. L. Benson, W. Yuan, W. H. Peter, L. Huang, A. Freels, R. A. Buchanan, C. T. Liu and C. R. Brooks, (2005) p. 429.

[25] G. Y. Wang, P. K. Liaw, A. Peker, M. Freels, W. H. Peter, R. A. Buchanan and C. R. Brooks, (2006) p. 1091.

[26] W. H. Peter, P. K. Liaw, R. A. Buchanan, C. T. Liu, C. R. Brooks, J. A. Horton, C. A. Carmichael and J. L. Wright, (Elsevier Sci Ltd, 2002) p. 1125.

[27] W. H. Peter, R. A. Buchanan, C. T. Liu and P. K. Liaw, J. Non-Cryst. Solids 317 (2003) 187.

[28] Y. Yokoyama, K. Fukaura and H. Sunada, Mater. Trans. JIM 41 (2000) 675.

[29] Z. F. Zhang, J. Eckert and L. Schultz, Metall. Mater. Trans. A-Phys. Metall. Mater. Sci. 35A (2004) 3489.

[30] Z. F. Zhang, J. Eckert and L. Schultz, J. Mater. Res. 18 (2003) 456.

[31] K. K. Cameron and R. H. Dauskardt, Scr. Mater. 54 (2006) 349.

[32] P. A. Hess, B. C. Menzel and R. H. Dauskardt, Scr. Mater. 54 (2006) 355.

[33] H. Zhang, Z. G. Wang, K. Q. Qiu, Q. S. Zang and H. F. Zhang, Materials Science and Engineering a-Structural Materials Properties Microstructure and Processing 356 (2003) 173.

[34] B. C. Menzel and R. H. Dauskardt, Acta Mater. 54 (2006) 935.

[35] D. C. Qiao, P. K. Liaw, C. Fan, Y. H. Lin, G. Y. Wang, H. Choo and R. A. Buchanan, (2006) p. 1043.

[36] S. Suresh, Fatigue of Materials (Cambridge University Press, Cambridge, 1991).

[37] S. Suresh, Eng. Fract. Mech. 21 (1985) 453.

[38] D. C. Qiao, G. Y. Wang, W. H. Jiang, Y. Yokoyama, P. K. Liaw and H. Choo, Mater. Trans. 48 (2007) 1828.

[39] F. Spaepen, Acta Metallurgica 25 (1977) 407.

[40] P. S. Steif, F. Spaepen and J. W. Hutchinson, Acta Metallurgica 30 (1982) 447.

[41] A. S. Argon, Acta Metallurgica 27 (1979) 47.

[42] P. Murah and U. Ramamurty, Acta Mater. 53 (2005) 1467.

[43] L. Y. Chen, Z. D. Fu, G. Q. Zhang, X. P. Hao, Q. K. Jiang, X. D. Wang, Q. P. Cao, H. Franz, Y. G. Liu, H. S. Xie, S. L. Zhang, B. Y. Wang, Y. W. Zeng and J. Z. Jiang, Phys. Rev. Lett. 100 (2008) 4.

[44] A. Rehmet, K. Gunther-Schade, K. Ratzke, U. Geyer and F. Faupel, Physica Status Solidi a-Applications and Materials Science 201 (2004) 467.

[45] X. H. Lin and W. L. Johnson, J. Appl. Phys. 78 (1995) 6514.

[46] Y. Yokoyama, M. Nishijima, K. Hiraga, P. K. Liaw and A. Inoue, Journal of Metastable and Nanocrystalline Materials 24-25 (2005) 677.

[47] M. E. Launey, R. Busch and J. J. Kruzic, Acta Mater. 56 (2008) 500.

[48] G. E. Dieter, Mechanical Metallurgy (McGraw-Hill, 1986).

[49] H. A. Bruck, A. J. Rosakis and W. L. Johnson, Journal of Materials Research 11 (1996) 503.

[50] H. A. Bruck, T. Christman, A. J. Rosakis and W. L. Johnson, Scr. Metall. Materialia 30 (1994) 429.

[51] C. C. Hays, C. P. Kim and W. L. Johnson, Phys. Rev. Lett. 84 (2000) 2901.

[52] A. H. Brothers and D. C. Dunand, Acta Mater. 53 (2005) 4427.

[53] J. Lu and G. Ravichandran, J. Mater. Res. 18 (2003) 2039.

[54] J. Schroers and W. L. Johnson, Phys. Rev. Lett. 93 (2004) 4.

[55] W. H. Jiang, G. J. Fan, H. Choo and P. K. Liaw, Mater. Lett. 60 (2006) 3537.

[56] H. Bei, S. Xie and E. P. George, Phys. Rev. Lett. 96 (2006) 4.

[57] H. M. Chen, Y. C. Chang, T. H. Hung, X. H. Du, J. C. Huang, J. S. C. Jang and P. K. Liaw, Mater. Trans. 48 (2007) 1802.

[58] F. F. Wu, Z. F. Zhang and S. X. Mao, Journal of Materials Research 22 (2007) 501.

[59] Z. F. Zhang, H. Zhang, X. F. Pan, J. Das and J. Eckert, Philos. Mag. Lett. 85 (2005) 513.

[60] W. Klement, R. H. Willens and P. Duwez, Nature 187 (1960) 869.

[61] P. Duwez and R. H. Willens, Transactions of the Metallurgical Society of Aime 227 (1963) 362.

[62] W. Buckel, Zeitschrift Fur Physik 138 (1954) 136.

[63] P. Pietrokowsky, Rev. Sci. Instrum. 34 (1963) 445.

[64] P. Duwez, R. H. Willens and R. C. Crewdson, J. Appl. Phys. 36 (1965) 2267.

[65] C. C. Tsuei and P. Duwez, J. Appl. Phys. 37 (1966) 435.

[66] P. Duwez and S. C. H. Lin, J. Appl. Phys. 38 (1967) 4096.

[67] H. S. Chen and D. Turnbull, Acta Metallurgica 17 (1969) 1021.

[68] H. S. Chen, Acta Metallurgica 22 (1974) 1505.

[69] A. J. Drehman, A. L. Greer and D. Turnbull, Appl. Phys. Lett. 41 (1982) 716.

[70] H. W. Kui, A. L. Greer and D. Turnbull, Appl. Phys. Lett. 45 (1984) 615.

[71] M. C. Lee, J. M. Kendall and W. L. Johnson, Appl. Phys. Lett. 40 (1982) 382.

[72] A. Inoue, T. Zhang and T. Masumoto, Mater. Trans. JIM 30 (1989) 965.

[73] A. Inoue, T. Zhang and T. Masumoto, Mater. Trans. JIM 31 (1990) 425.

[74] S. G. Kim, A. Inoue and T. Masumoto, Mater. Trans. JIM 31 (1990) 929.

[75] A. Inoue, A. Kato, T. Zhang, S. G. Kim and T. Masumoto, Mater. Trans. JIM 32 (1991) 609.

[76] A. Inoue, T. Nakamura, N. Nishiyama and T. Masumoto, Mater. Trans. JIM 33 (1992) 937.

[77] A. Inoue, T. Zhang and T. Masumoto, Mater. Trans. JIM 31 (1990) 177.

[78] T. Zhang, A. Inoue and T. Masumoto, Mater. Trans. JIM 32 (1991) 1005.

[79] A. Inoue, T. Zhang, N. Nishiyama, K. Ohba and T. Masumoto, Mater. Trans. JIM 34 (1993) 1234.

[80] A. Peker and W. L. Johnson, Appl. Phys. Lett. 63 (1993) 2342.

[81] A. Inoue, N. Nishiyama and H. Kimura, Mater. Trans. JIM 38 (1997) 179.

[82] A. Inoue, Proc. Jpn. Acad. Ser. B-Phys. Biol. Sci. 81 (2005) 156.

[83] A. Takeuchi and A. Inoue, Mater. Trans. 46 (2005) 2817.

[84] H. A. Davies, Amorphous Metallic Alloys (Butterworth & Co. Ltd., London, 1983).

[85] A. Inoue, Acta Mater. 48 (2000) 279.

[86] A. Inoue, N. Nishiyama and T. Matsuda, Mater. Trans. JIM 37 (1996) 181.

[87] A. Inoue, Mater. Trans. JIM 36 (1995) 866.

[88] Y. Yokoyama and A. Inoue, Mater. Trans. JIM 36 (1995) 1398.

[89] A. Inoue and T. Zhang, Mater. Trans. JIM 37 (1996) 185.

[90] A. Inoue, Sci. Rep. Res. Inst. Tohoku Univ. Ser. A-Phys. Chem. Metall. 42 (1996) 1.

[91] A. Inoue, Proc. Jpn. Acad. Ser. B-Phys. Biol. Sci. 73 (1997) 19.

[92] D. Turnbull, Contemp. Phys. 10 (1969) 473.

[93] Z. P. Lu and C. T. Liu, Acta Mater. 50 (2002) 3501.

[94] Z. P. Lu, H. Tan, Y. Li and S. C. Ng, Scr. Mater. 42 (2000) 667.

[95] A. L. Greer, Science 267 (1995) 1947.

[96] A. Inoue, B. L. Shen and C. T. Chang, (Elsevier Sci Ltd, 2006) p. 936.

[97] A. S. Argon and H. Y. Kuo, Materials Science and Engineering 39 (1979) 101.

[98] D. Deng, A. S. Argon and S. Yip, Philos. Trans. R. Soc. Lond. Ser. A-Math. Phys. Eng. Sci. 329 (1989) 613.

[99] M. L. Falk and J. S. Langer, Phys. Rev. E 57 (1998) 7192.

[100] M. L. Falk, Phys. Rev. B 60 (1999) 7062.

[101] A. C. Lund and C. A. Schuh, Acta Mater. 51 (2003) 5399.

[102] H. J. Leamy, H. S. Chen and T. T. Wang, Metallurgical Transactions 3 (1972) 699.

[103] K. M. Flores and R. H. Dauskardt, J. Mater. Res. 14 (1999) 638.

[104] B. Yang, M. L. Morrison, P. K. Liaw, R. A. Buchanan, G. Y. Wang, C. T. Liu and M. Denda, Appl. Phys. Lett. 86 (2005) 3.

[105] B. Yang, C. T. Liu, T. G. Nieh, M. L. Morrison, P. K. Liaw and R. A. Buchanan, J. Mater. Res. 21 (2006) 915.

[106] J. J. Lewandowski and A. L. Greer, Nat. Mater. 5 (2006) 15.

[107] W. J. Wright, R. B. Schwarz and W. D. Nix, Material Science and Engineering A 319 (2001) 229.

[108] P. E. Donovan, Acta Metallurgica 37 (1989) 445.

[109] R. Vaidyanathan, M. Dao, G. Ravichandran and S. Suresh, Acta Mater. 49 (2001) 3781.

[110] W. J. Wright, R. Saha and W. D. Nix, Material Transactions 42 (2001) 642.

[111] C. A. Schuh and A. C. Lund, Nat. Mater. 2 (2003) 449.

[112] H. Guo, P. F. Yan, Y. B. Wang, J. Tan, Z. F. Zhang, M. L. Sui and E. Ma, Nat. Mater. 6 (2007) 735.

[113] F. F. Wu, Z. F. Zhang and S. X. Mao, Acta Mater. 51 (2009) 257.

[114] S. Xie and E. P. George, Intermetallics 16 (2008) 485.

[115] C. J. Lee, J. C. Huang and T. G. Nieh, Appl. Phys. Lett. 91 (2007) 3.

[116] B. E. Schuster, Q. Wei, T. C. Hufnagel and K. T. Ramesh, Acta Mater. 56 (2008) 5091.

[117] Y. J. Huang, J. Shen and J. F. Sun, Appl. Phys. Lett. 90 (2007) 3.

[118] W. H. Jiang, F. X. Liu, Y. D. Wang, H. F. Zhang, H. Choo and P. K. Liaw, Mater. Sci. Eng. A-Struct. Mater. Prop. Microstruct. Process. 430 (2006) 350.

[119] Q. Zheng, S. Cheng, J. H. Strader, E. Ma and J. Xu, Scr. Mater. 56 (2007) 161.

[120] C. A. Volkert, A. Donohue and F. Spaepen, J. Appl. Phys. 103 (2008) 6.

[121] Z. W. Shan, J. Li, Y. Q. Cheng, A. M. Minor, S. A. S. Asif, O. L. Warren and E. Ma, Phys. Rev. B 77 (2008) 6.

[122] F. Szuecs, C. P. Kim and W. L. Johnson, Acta Mater. 49 (2001) 1507.

[123] R. D. Conner, W. L. Johnson, N. E. Paton and W. D. Nix, J. Appl. Phys. 94 (2003) 904.

[124] Y. Yokoyama, K. Yamano, K. Fukaura, H. Sunada and A. Inoue, (Japan Inst Metals, 2001) p. 623.

[125] L. A. Davis, J. Mater. Sci. 10 (1975) 1557.

[126] T. Ogura, K. Fukushima and T. Masumoto, Scripta Metallurgica 9 (1975) 979.

[127] A. T. Alpas, L. Edwards and C. N. Reid, Metallurgical Transactions a-Physical Metallurgy and Materials Science 20 (1989) 1395.

[128] M. L. Morrison, R. A. Buchanan, P. K. Liaw, B. A. Green, G. Y. Wang, C. Liu and J. A. Horton, Mater. Sci. Eng. A-Struct. Mater. Prop. Microstruct. Process. 467 (2007) 190.

[129] M. Freels, P. K. Liaw, G. Y. Wang, Q. S. Zhang and Z. Q. Hu, J. Mater. Res. 22 (2007) 374.

[130] G. Y. Wang, D. C. Qiao, Y. Yokoyama, M. Freels, A. Inoue and P. K. Liaw, Journal of Alloys and Compounds 483 (2008) 143.

[131] G. Y. Wang, P. K. Liaw, Y. Yokoyama, M. Freels and A. Inoue, Adv. Eng. Mater. 10 (2008) 1030.

[132] D. C. Qiao, G. J. Fan, P. K. Liaw and H. Choo, Int. J. Fatigue 29 (2007) 2149.

[133] D. C. Qiao, G. Y. Wang, P. K. Liaw, V. Ponnambalam, S. J. Poon and G. J. Shiflet, J. Mater. Res. 22 (2007) 544.

[134] M. E. Launey, R. Busch and J. J. Kruzic, Scr. Mater. 54 (2006) 483.

[135] G. Y. Wang, P. K. Liaw, W. H. Peter, B. Yang, Y. Yokoyama, M. L. Benson, B. A. Green, M. J. Kirkham, S. A. White, T. A. Saleh, R. L. McDaniels, R. V. Steward, R. A. Buchanan, C. T. Liu and C. R. Brooks, Intermetallics 12 (2004) 885.

[136] G. Y. Wang, P. K. Liaw, A. Peker, B. Yang, M. L. Benson, W. Yuan, W. H. Peter, L. Huang, A. Freels, R. A. Buchanan, C. T. Liu and C. R. Brooks, Intermetallics 13 (2005) 429.

[137] B. C. Menzel, Fatigue Behavior of Bulk Metallic Glasses, in "Materials Science" (Stanford, 2007).

[138] G. Y. Wang, P. K. Liaw, A. Peker, M. Freels, W. H. Peter, R. A. Buchanan and C. R. Brooks, Intermetallics 14 (2006) 1091.

[139] G. Wang, P. K. Liaw, Y. Yokoyama, A. Peker, W. H. Peter, B. Yang, M. Freels, Z. Y. Zhang, V. Keppens, R. Hermann, R. A. Buchanan, C. T. Liu and C. R. Brooks, Intermetallics 15 (2007) 663.

[140] Y. Yokoyama, N. Nishiyama, K. Fukaura, H. Sunada and A. Inoue, Mater. Trans. JIM 40 (1999) 696.

[141] Y. Yokoyama, K. Fukaura and A. Inoue, (Japan Inst Metals, 2004) p. 1672.

[142] Y. Yokoyama, P. K. Liaw, M. Nishijima, K. Hiraga, R. A. Buchanan and A. Inoue, Mater. Trans. 47 (2006) 1286.

[143] L. A. Davis, in "Metallic Glasses", edited by P. Duwez (ASM, Metals Park, 1978) p. 190.

[144] R. W. Hertzberg, Deformation and Fracture Mechanics of Engineering Materials (John Wiley & Sons, Inc., New York, NY, 1996).

[145] B. C. Menzel and R. H. Dauskardt, Acta Mater. 56 (2008) 2955.

[146] W. H. Peter, G. Y. Wang, P. K. Liaw, R. A. Buchanan, C. T. Liu, M. L. Morrison and C. R. Brooks, Key Engineering Materials 345-346 (2007) 217.

[147] C. T. Liu, M. F. Chisholm and M. K. Miller, Intermetallics 10 (2002) 1105.

[148] D. H. Xu, B. Lohwongwatana, G. Duan, W. L. Johnson and C. Garland, Acta Mater. 52 (2004) 2621.

[149] D. Wang, Y. Li, B. B. Sun, M. L. Sui, K. Lu and E. Ma, Appl. Phys. Lett. 84 (2004) 4029.

[150] D. H. Xu, G. Duan and W. L. Johnson, Phys. Rev. Lett. 92 (2004) 4.

[151] W. Zhang, F. Jia, Q. S. Zhang and A. Inoue, Materials Science and Engineering a-Structural Materials Properties Microstructure and Processing 459 (2007) 330.

[152] A. Kawashima, T. Okuno, H. Kurishita, W. Zhang, H. Kimura and A. Inoue, Material Transactions 48 (2007) 2787.

[153] M. Kusy, U. Kuhn, A. Concustell, A. Gebert, J. Das, J. Eckert, L. SchultZ and M. D. Baro, (Elsevier Sci Ltd, 2006) p. 982.

[154] S. Suresh, Fatigue of Materials (University Press, Cambridge, 1991).

[155] J. S. C. Jang, Y. W. Chen, L. J. Chang, H. Z. Cheng, C. C. Huang and C. Y. Tsau, Mater. Chem. Phys. 89 (2005) 122.

[156] J. S. C. Jang, C. F. Chang, Y. C. Huang, J. C. Huang, W. J. Chiang and C. T. Liu, Intermetallics 17 (2009) 200.

[157] Z. P. Lu, J. Shen, D. W. Xing, J. F. Sun and C. T. Liu, Appl. Phys. Lett. 89 (2006) 3.

[158] M. Freels, G. Y. Wang, W. Zhang, P. K. Liaw and A. Inoue, Cyclic Compression Behavior of a Cu-Zr-Al-Ag Bulk Metallic Glass, (2009).

[159] Q. S. Zhang, H. F. Zhang, Y. F. Deng, B. Z. Ding and Z. Q. Hu, Scr. Mater. 49 (2003) 273.

[160] F. Baratta, ASTM STP 844 (1984) 194.

[161] ASM International Handbook (ASM, Metals Park, OH, 1990).

[162] T. Mukai, T. G. Nieh, Y. Kawamura, A. Inoue and K. Higashi, Intermetallics 10 (2002) 1071.

[163] W. J. Wright, R. Saha and W. D. Nix, (Japan Inst Metals, 2001) p. 642.

[164] S. Pauly, J. Das, C. Duhamel and J. Eckert, Advanced Engineering Materials 9 (2007) 487.

[165] R. W. Cahn, Physical Metallurgy (Elsevier Science & Technology Books, 1996).

[166] R. D. Conner, H. Choi-Yim and W. L. Johnson, Journal of Materials Research 14 (1999) 3292.

[167] S. W. Lee, M. Y. Huh, E. Fleury and J. C. Lee, Acta Mater. 54 (2006) 349.

[168] F. Jiang, D. H. Zhang, L. C. Zhang, Z. B. Zhang, L. He, J. Sun and Z. F. Zhang, Materials Science and Engineering a-Structural Materials Properties Microstructure and Processing 467 (2007) 139.

[169] G. Wang, D. C. Qiao, Y. Yokoyama, M. Freels, A. Inoue and P. K. Liaw, Journal of Alloys and Compounds 483 (2009) 3.

[170] M. Cerit, K. Genel and S. Eksi, Eng. Fail. Anal. 16 (2009) 2467.

[171] J. Schijve, Fatigue of Structures and Materials (Springer Netherlands, 2009).

[172] Y. Liu, H. Bei, C. T. Liu and E. P. George, Appl. Phys. Lett. 90 (2007) 3.

[173] J. Shen, Y. J. Huang and J. F. Sun, Journal of Materials Research 22 (2007) 3067.

[174] A. Slipenyuk and J. Eckert, Scr. Mater. 50 (2004) 39.

[175] G. Y. Wang, P. K. Liaw, Y. Yokoyama, M. Freels and A. Inoue, Intenational Journal of Fatigue 32 (2010) 599.

[176] Z. F. Zhang, G. He, H. Zhang and J. Eckert, Scr. Mater. 52 (2005) 945.

[177] M. Freels, G. Y. Wang, W. Zhang, P. K. Liaw and A. Inoue, Cyclic Compression Behavior of a CuZrAlAg Bulk Metallic Glass, (The University of Tennessee, Knoxville, 2009).

[178] J. C. Newman and I. S. Raju, (1984) 85793.

[179] R. C. Bates and J. Clark, W.G., Transactions of the ASM 62 (1969) 380.

[180] C. A. Pampillo, J. Mater. Sci. 10 (1975) 1194.

[181] C. J. Gilbert, J. W. Ager, V. Schroeder, R. O. Ritchie, J. P. Lloyd and J. R. Graham, Appl. Phys. Lett. 74 (1999) 3809.

APPENDIX

Table 2-1: Comprehensive summary of the experimental conditions and the reported σ_L for BMGs.

System	Loading Method	Geometry (mm)	Frequency (Hz)	R-ratio	Surface Finish	Endurance Limit	Fatigue Ratio	Reference
$Zr_{41.2}Ti_{13.8}Cu_{12.5}Ni_{10}Be_{22.5}$	4PB	3 x 3 x 50	25	0.1	1 μm	152	0.08	[19]
$Zr_{41.2}Ti_{13.8}Cu_{12.5}Ni_{10}Be_{22.5}$	4PB	3 x 3 x 40	5	0.1	0.1 μm	190	0.10	[34]
$Zr_{52.5}Cu_{17.9}Ni_{14.6}Al_{10.0}Ti_{5.0}$	4PB	3.5 x 3.5 x 30	10	0.1	0.1 μm	850	0.50	[128]
$Fe_{48}Cr_{15}Mo_{14}Er_2C_{15}B_6$	4PB	3 x 3 x 25	10	0.1	6.5 μm	682	0.17	[133]
$Cu_{47.5}Zr_{47.5}Al_5$	4PB	3 x 3 x 25	10	0.1	6.5 μm	224	0.12	[132]
$Zr_{50}Al_{10}Cu_{37}Pd_3$	4PB	3.5 x 3.5 x 25	10	0.1	"polished"	630	0.33	[130]
$Zr_{50}Cu_{40}Al_{10}$	4PB	3 x 3 x 25	10	0.1	6.5 μm	542	0.30	[131]
$Zr_{50}Cu_{30}Ni_{10}Al_{10}$	4PB	3 x 3 x 25	10	0.1	6.5 μm	635	0.33	[131]
$(Cu_{60}Zr_{30}Ti_{10})_{99}Sn_1$	4PB	3 x 3 x 25	10	0.1	9 μm	350	0.19	[129]
$Zr_{41.2}Ti_{13.8}Cu_{12.5}Ni_{10}Be_{22.5}$	3PB	2 x 2 x 60	20	0.1	as-cast	768	0.40	[134]
$Zr_{41.2}Ti_{13.8}Cu_{12.5}Ni_{10}Be_{22.5}$	3PB	2 x 2 x 60	20	0.1	as-cast	359	0.19	[134]
$Zr_{50}Al_{10}Cu_{37}Pd_3$	3PB	3.5 x 3.5 x 25	10	0.1	"polished"	631	0.33	[130]
$(Cu_{60}Zr_{30}Ti_{10})_{99}Sn_1$	3PB	2.85 x 2.85 x 25	10	0.1	9 μm	475	0.26	[129]
$Zr_{52.5}Al_{10}Ti_5Cu_{17.9}Ni_{14.6}$	TT (notch)	∅2.98	10	0.1	9 μm	908	0.53	[7]
$Zr_{59}Cu_{20}Al_{10}Ni_8Ti_3$	TT	3 x 1.5 x 6	1	0.1	"mirror"	–	–	[30]
$Zr_{50}Cu_{40}Al_{10}$	TT (notch)	∅2.98	10	0.1	9 μm	752	0.41	[135]
$Zr_{50}Cu_{30}Ni_{10}Al_{10}$	TT (notch)	∅2.98	10	0.1	9	865	0.46	[135]
$Zr_{52.5}Cu_{17.9}Al_{10}Ni_{14.6}Ti_5$	TT	3 x 1.5 x 6	1	0.1	"mirror"	–	–	[29]
$Zr_{41.2}Ti_{13.8}Cu_{12.5}Ni_{10}Be_{22.5}$	TT (notch)	∅2.98	10	0.1	9 μm	703	0.38	[136]
$Zr_{41.2}Ti_{13.8}Cu_{12.5}Ni_{10}Be_{22.5}$	TT (notch)	∅2.98	10	0.1	9 μm	615	0.33	[136]
$Zr_{41.25}Ti_{13.75}Cu_{12.5}Ni_{10}Be_{22.5}$	TT (taper)	∅4	10	0.1	0.5 μm	114	0.06	[137]
$Zr_{41.2}Ti_{13.8}Cu_{12.5}Ni_{10}Be_{22.5}$	TT (taper)	∅2.98	10	0.1	9 μm	567	0.31	[138]
$Zr_{50}Cu_{37}Al_{10}Pd_3$	TT (notch)	∅2.98	10	0.1	9 μm	988	0.52	[139]
$Zr_{52.5}Cu_{17.9}Al_{10}Ni_{14.6}Ti_5$	CC	6 x 3	1	0.1	"mirror"	–	–	[29]
$Zr_{41.25}Ti_{13.75}Cu_{12.5}Ni_{10}Be_{22.5}$	CC	12 x 4	10	0.1	0.2 μm	1064	0.60	[137]
$Zr_{50}Al_{10}Cu_{37}Pd_3$	CC	10.66 x 5.33	10	0.1	"grind"	856	0.45	[38]

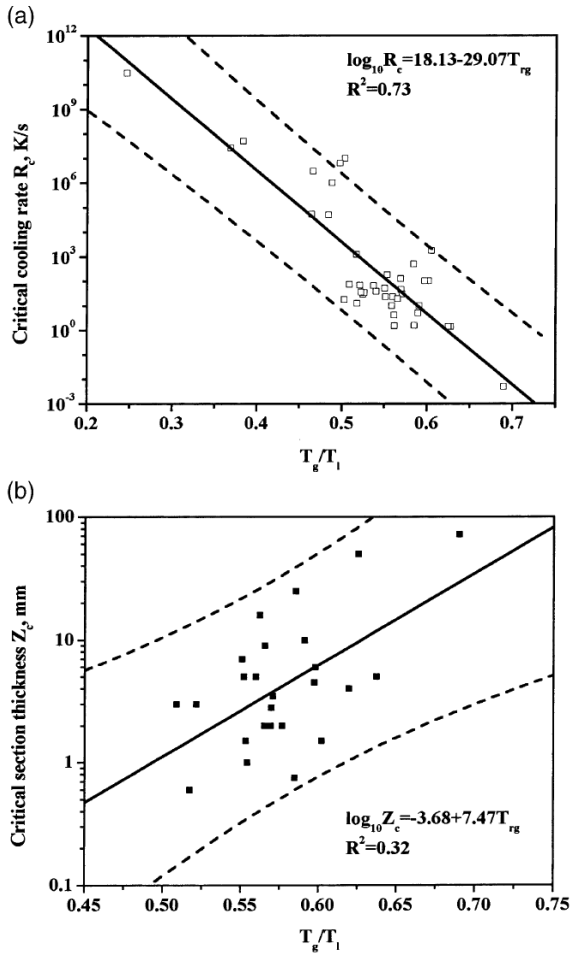

Figure 2-1: The correlation between T_g / T_l and (a) R_c, and (b) t_{max} [93].

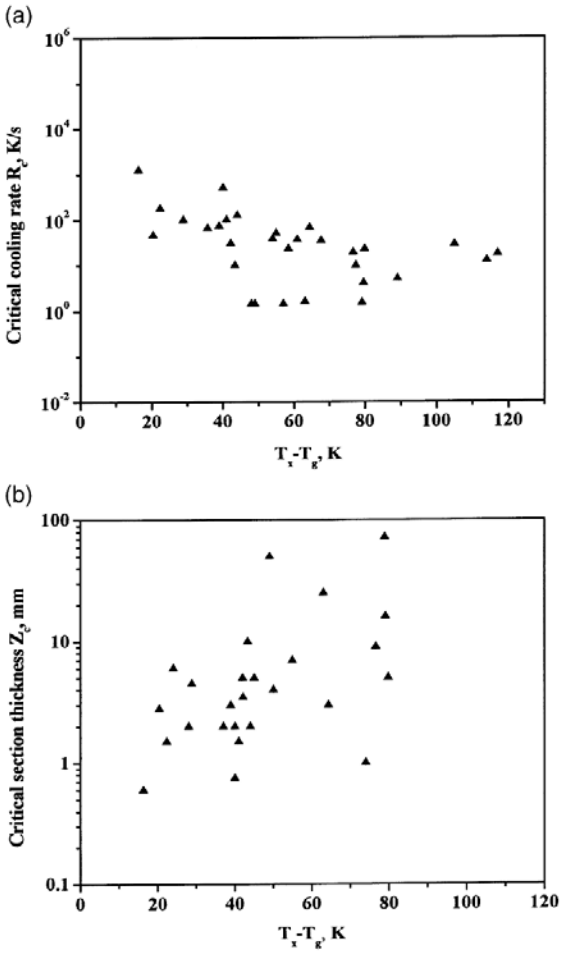

Figure 2-2: The correlation between ΔT_{xg} and (a) R_c and (b) t_{max} [93].

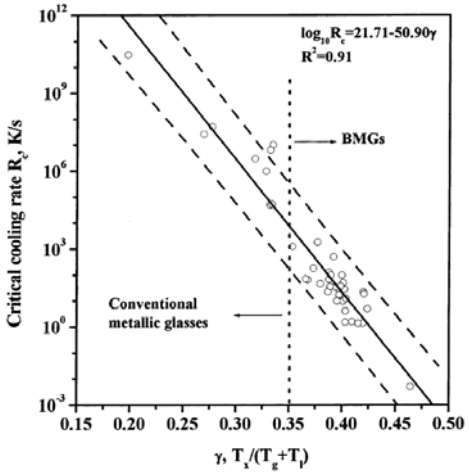

(a)

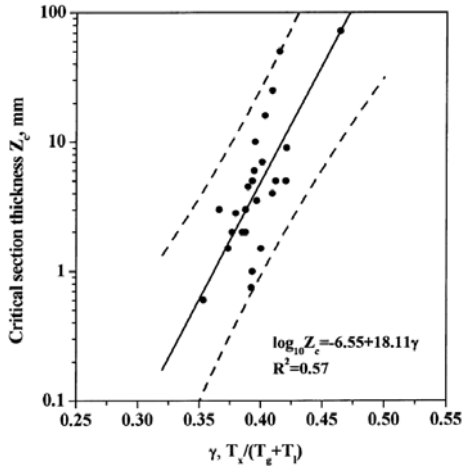

(b)

Figure 2-3: The correlation between γ and (a) R_c, and (b) t_{max} [93].

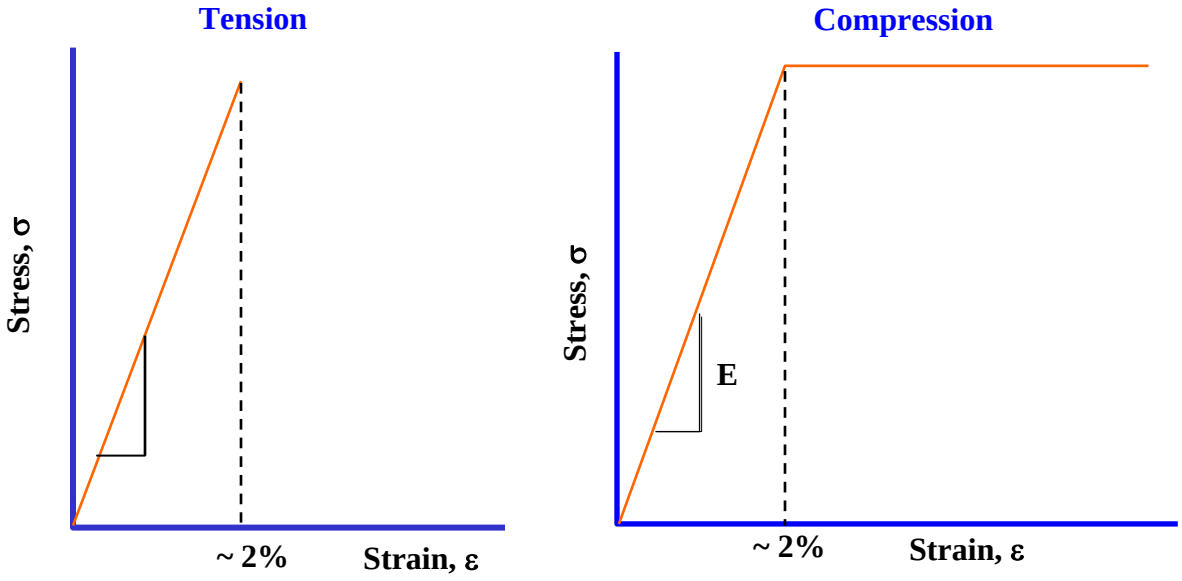

Figure 2-4: Typical room temperature stress-strain curves for BMGs; (a) tension and (b) compression.

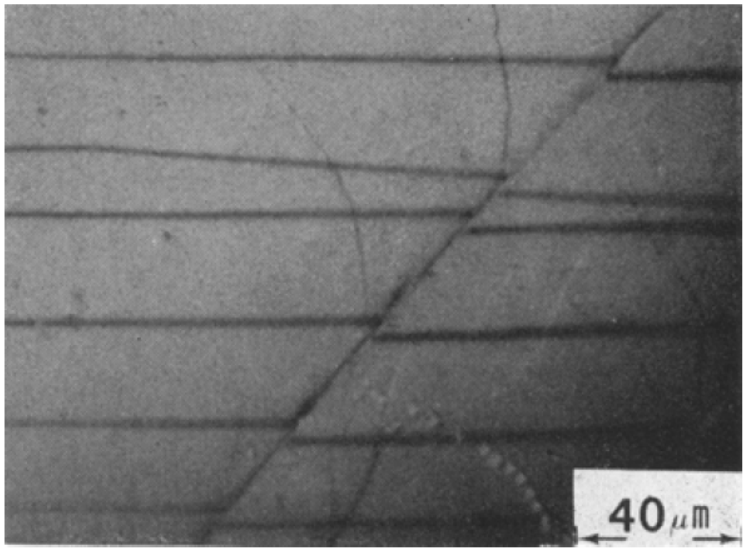

Figure 2-5: Shear bands in a Pd-based BMG [180].

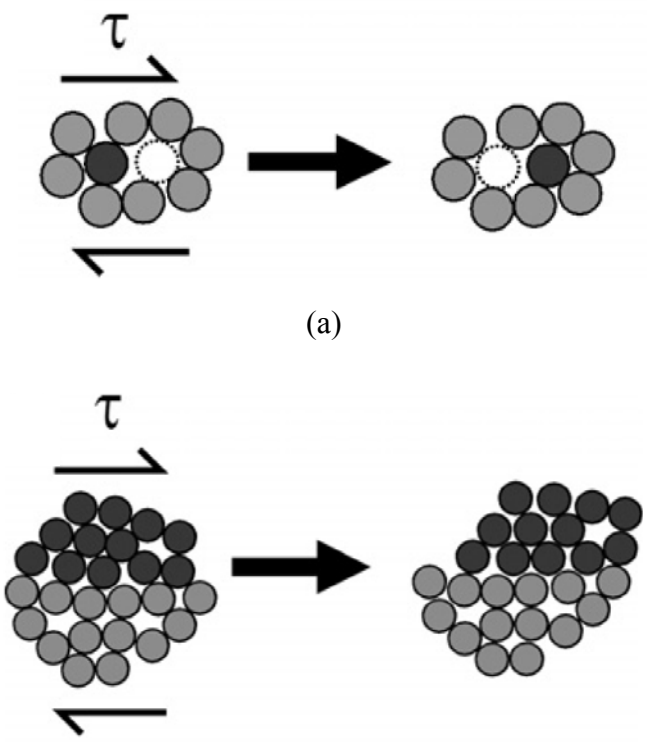

Figure 2-6: Schematics of the two main theories that exist in the literature that attempt to describe the deformation mechanisms of metallic glasses, including (a) a local atomic jump [39] and (b) a STZ [41].

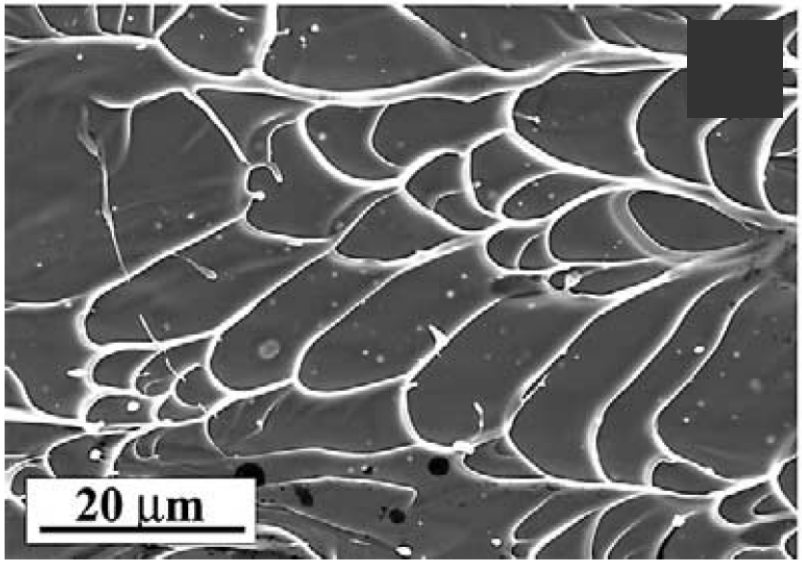

Figure 2-7: Compressive fracture surface of a Zr-based BMG [4].

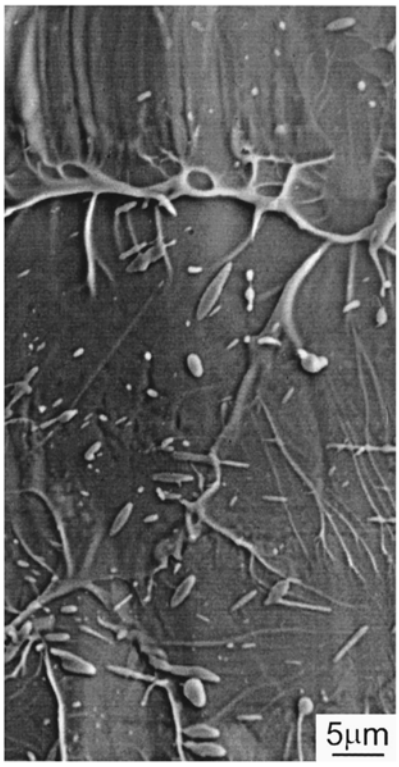

Figure 2-8: Liquid droplets on the fracture surface of a Zr-based BMG [181].

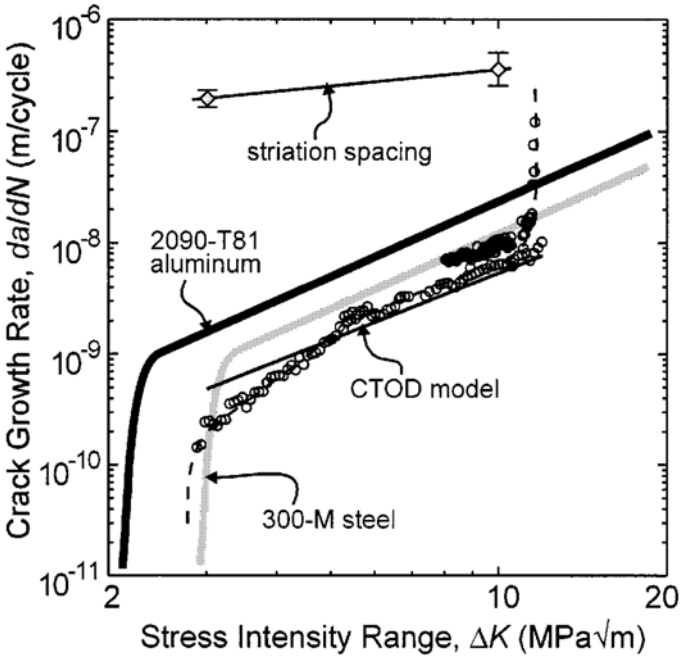

Figure 2-9: Crack growth rate (da/dN) as a function of ΔK for a Zr-based BMG [2]. Also shown are results for a high-strength steel and an age-hardened aluminum alloy for comparison.

.

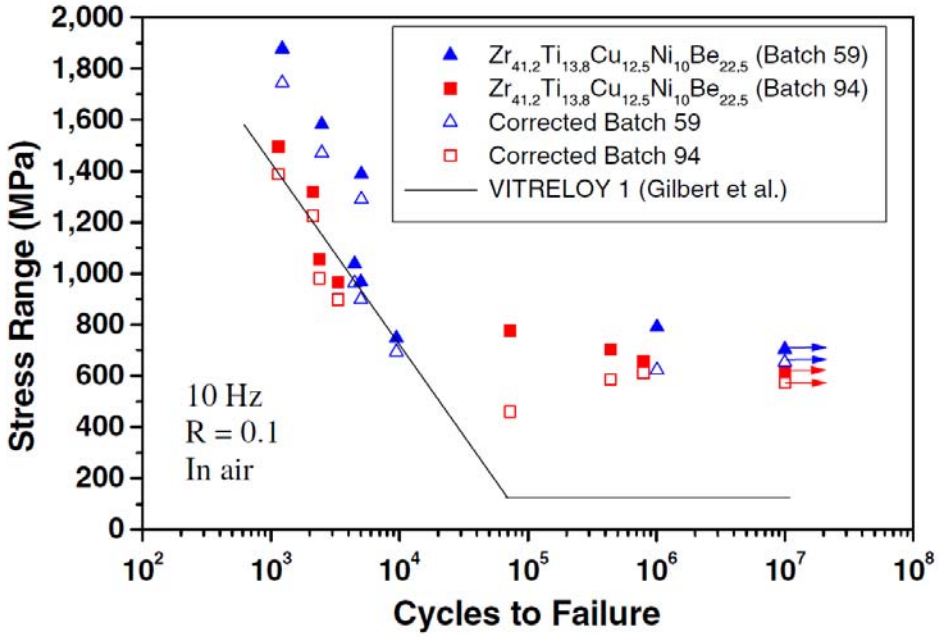

Figure 2-10: S-N data showing large variability in the S-N behavior of BMGs even for seemingly the same alloy [11].

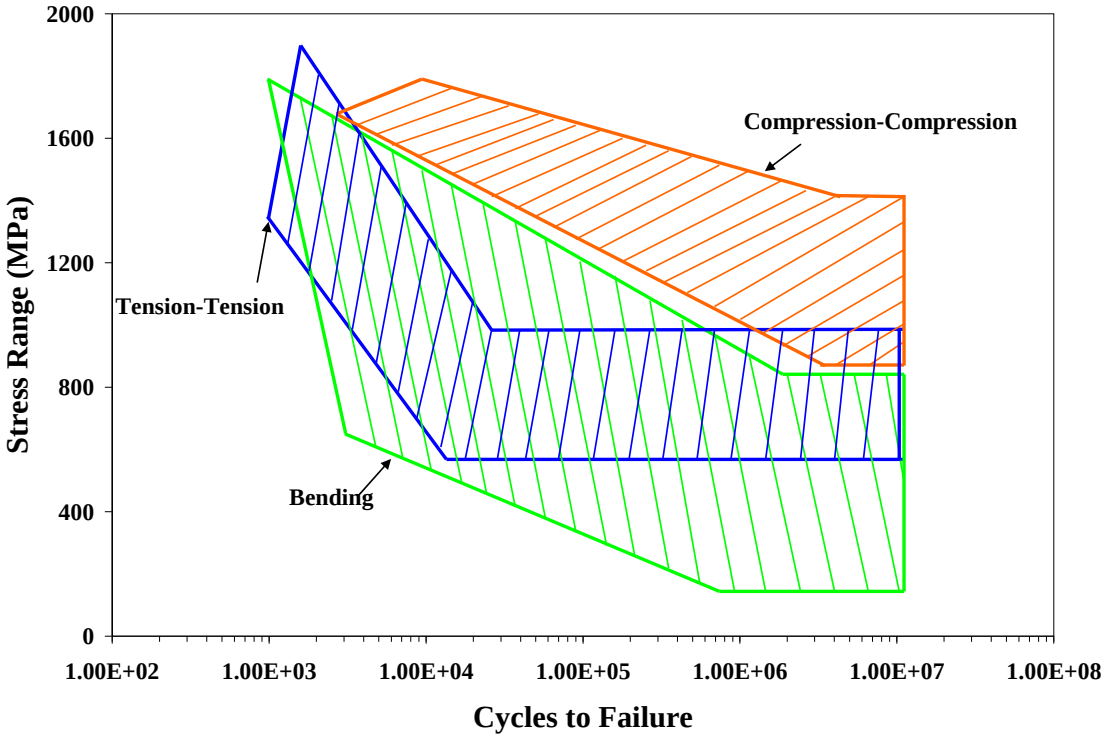

Figure 2-11: A comparison of the S-N behavior of all BMG compositions under cyclic bending [19, 34, 128-133], TT [7, 29, 30, 135-139], and CC [29, 38, 137] loading conditions.

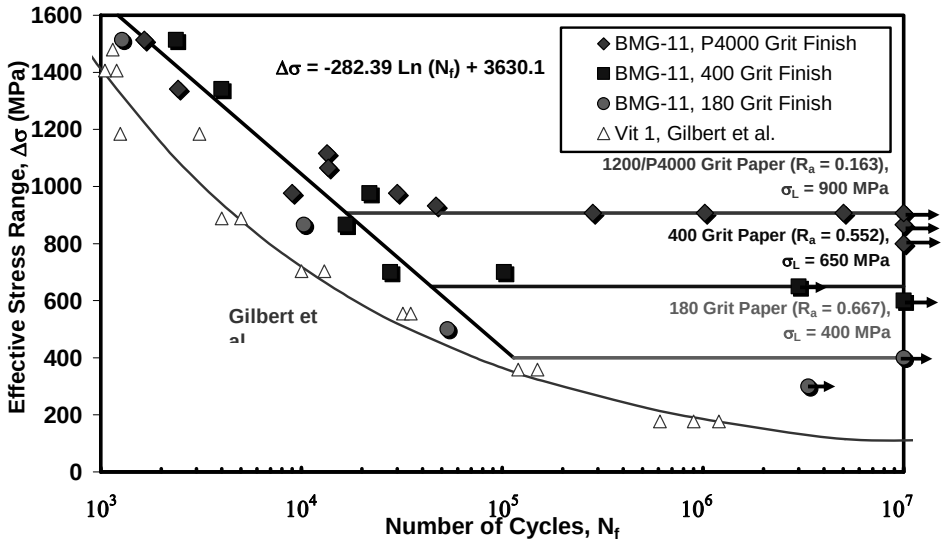

Figure 2-12: Comparing the S-N behavior of a Zr-based BMG with various finishes [146].

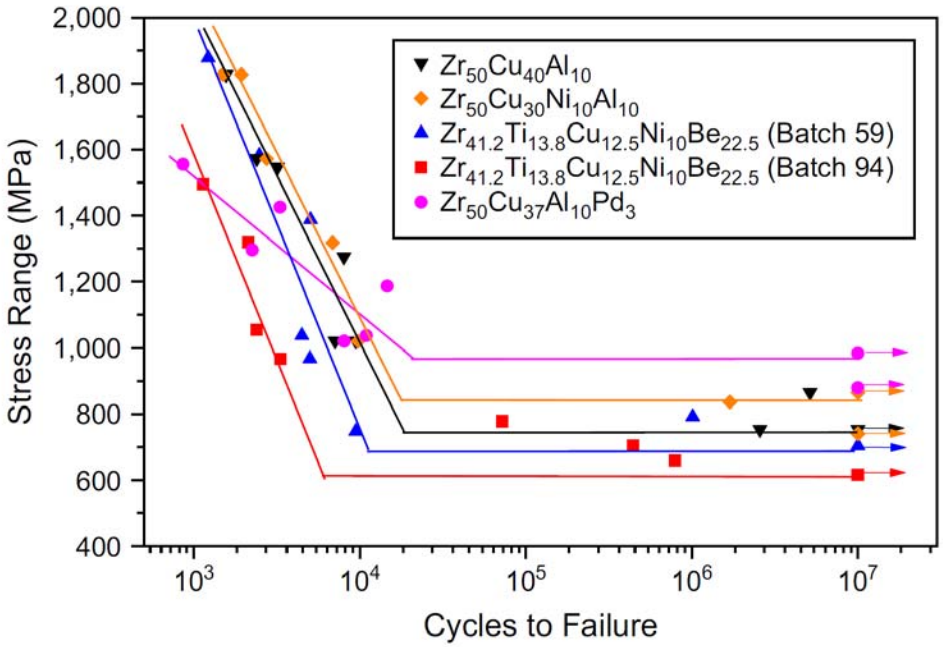

Figure 2-13: S-N data for various Zr-based BMGs tested under same TT cyclic loading conditions [139].

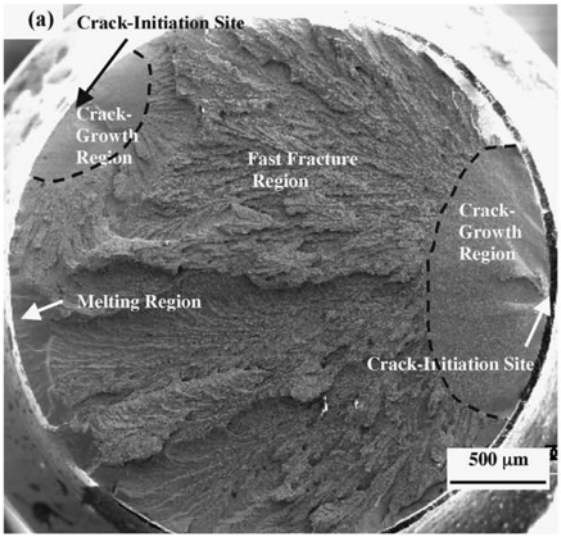

(a)

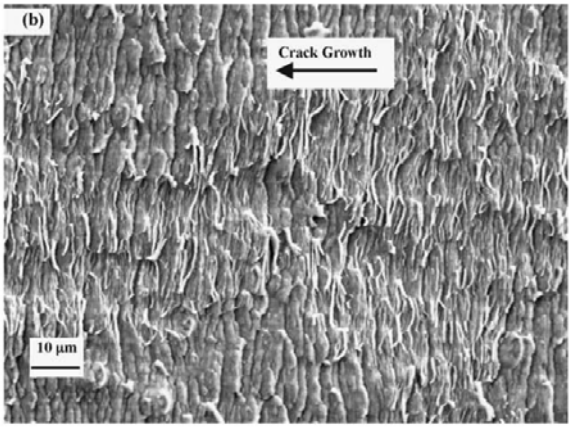

(b)

Figure 2-14: The fracture surface of a Zr-based BMG subjected to TT fatigue [135]; (a) over all fracture surface showing four distinct regions: the crack initiation site, crack propagation, unstable fast fracture, and apparent melting regions, (b) higher magnification of the crack propagation region.

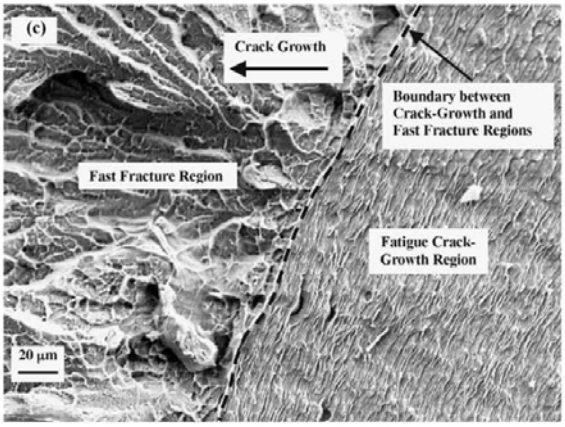

(c)

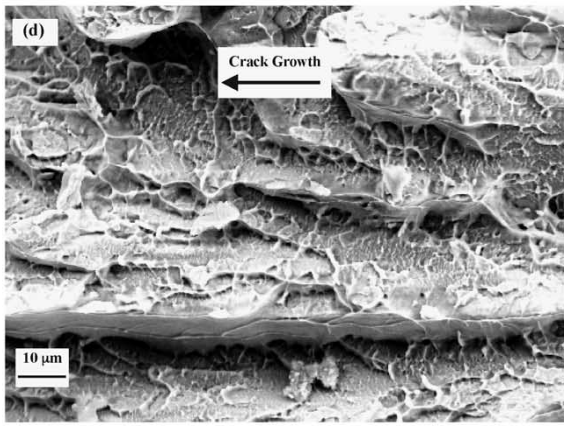

(d)

Figure 2-14: (continued) (c) transition from stable crack propagation to unstable crack propagation (fast fracture), (d) higher magnification of the unstable crack propagation region.

(e)

Figure 2-14: (continued) (e) melting region.

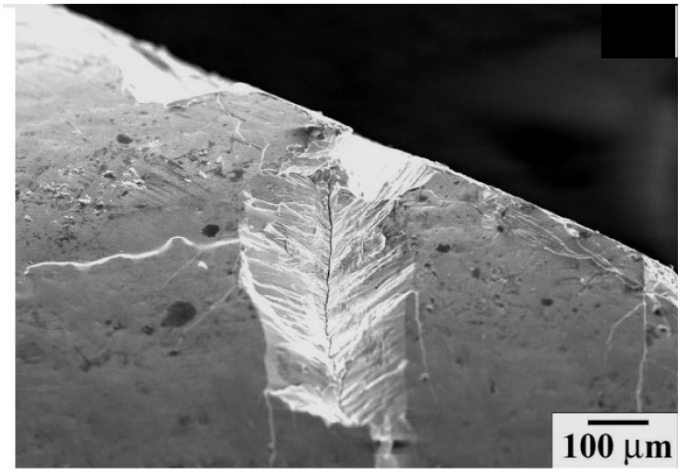

(a)

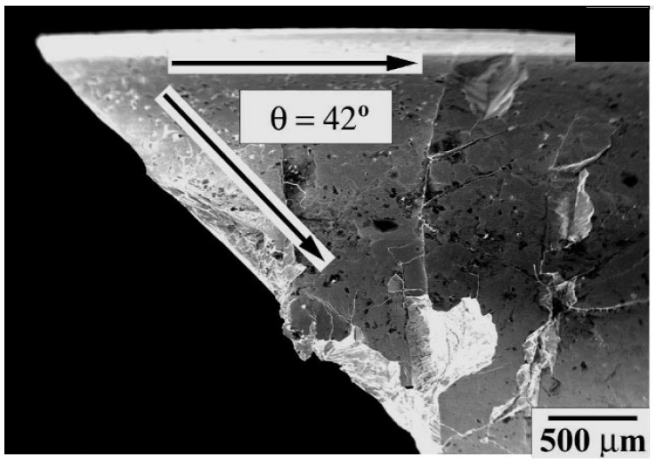

(b)

Figure 2-15: Fatigue fracture surface of a Zr-based BMG during CC cyclic loading [29]; (a) severely damaged surface area on the outside surface, (b) failure occurs by unstable fracture in a shear mode.

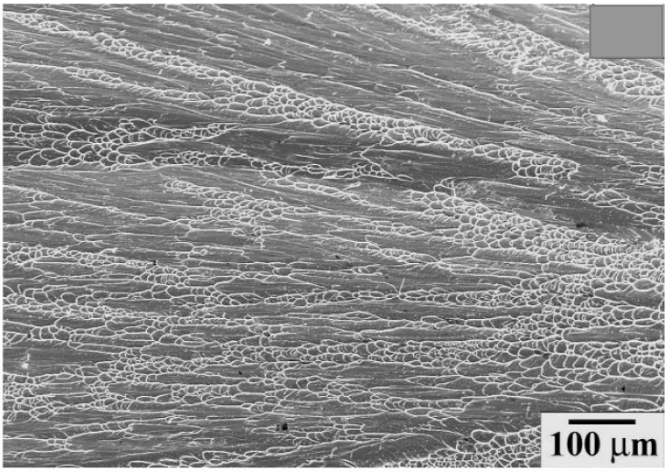

(c)

Figure 2-15: (continued) (c) vein-like structure that nearly covers the entire fracture surface.

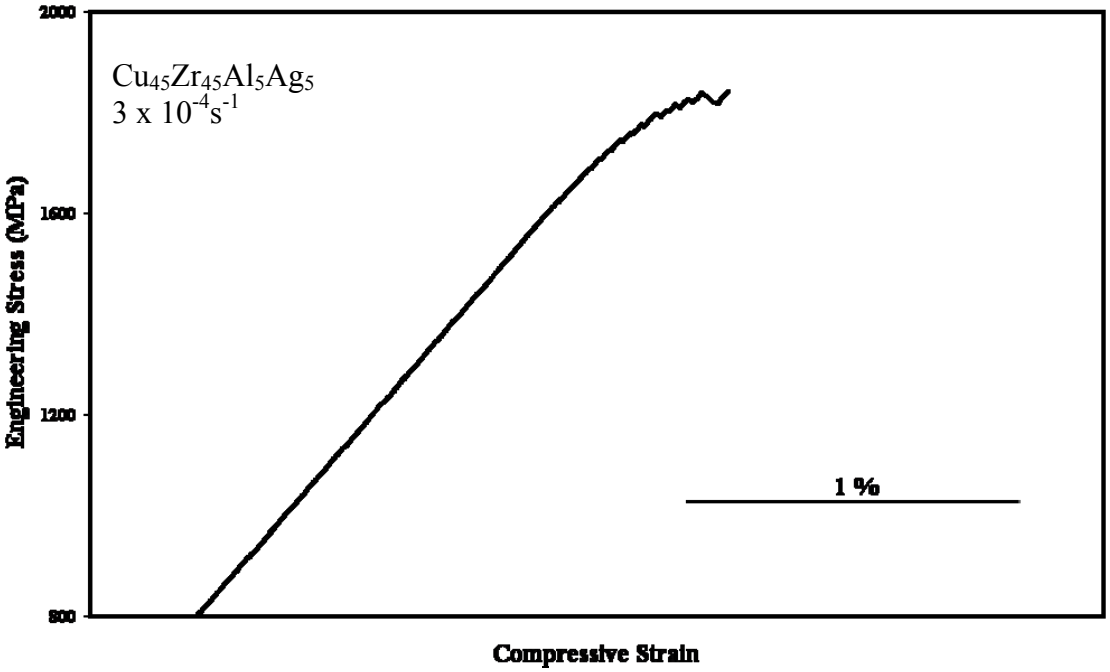

Figure 4-1: Monotonic compressive stress–strain curve for the $Cu_{45}Zr_{45}Al_5Ag_5$ BMG at a strain rate of 3 x $10^{-4}s^{-1}$. The BMG displays a compressive ε_p of 0.004. The σ_F reaches 1,845 MPa, while the measured E is approximately equal to 90 GPa.

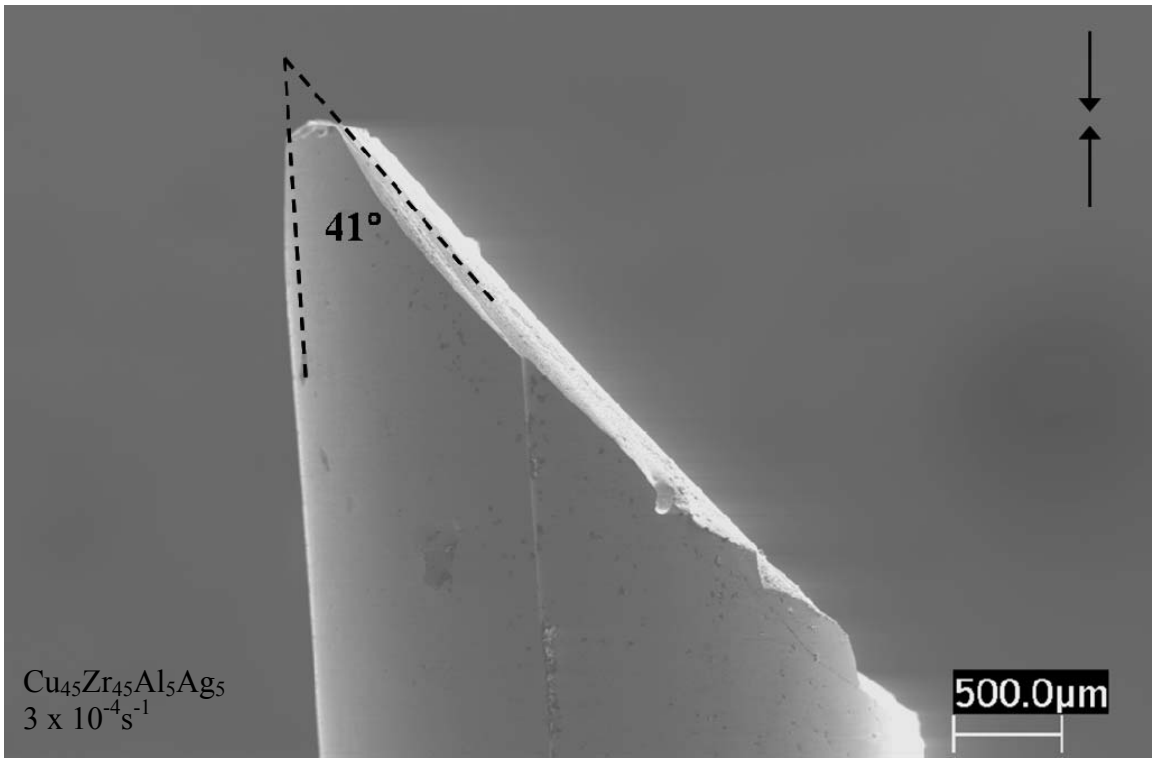

Figure 4-2: Fracture under compression occurring in a pure shear mode. The fracture plane forms an θ_c of 41° with respect to the compressive loading axis. The two arrows in the top right corner indicate the loading direction.

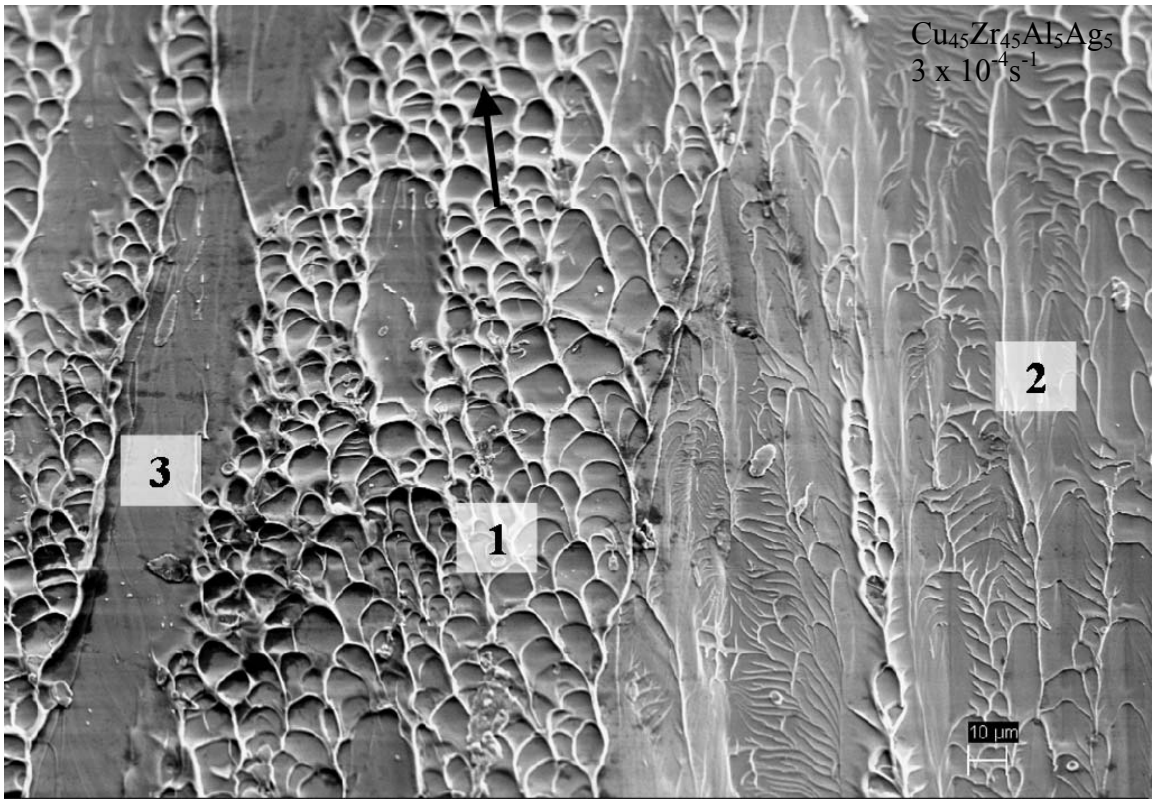

Figure 4-3: The monotonic fracture surface exhibiting three distinct features: (1) a vein-like pattern that covers the majority of the fracture surface (area 1), (2) a river-like pattern (area 2), and (3) intermitting smooth regions (area 3).

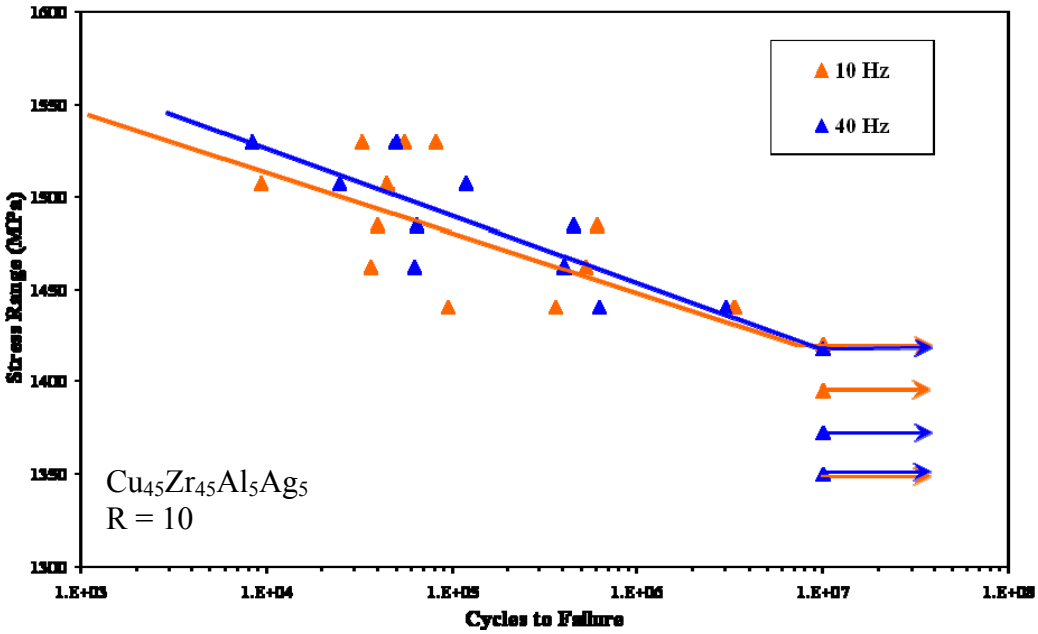

Figure 4-4: The N_f measured as a function of the applied σ_R, for both 10 and 40 Hz. The σ_L was found to be at least 1,418 MPa for both frequencies tested. The R was kept at 10 under a load-control mode using a sinusoidal waveform. Testing was conducted in an air environment at room temperature.

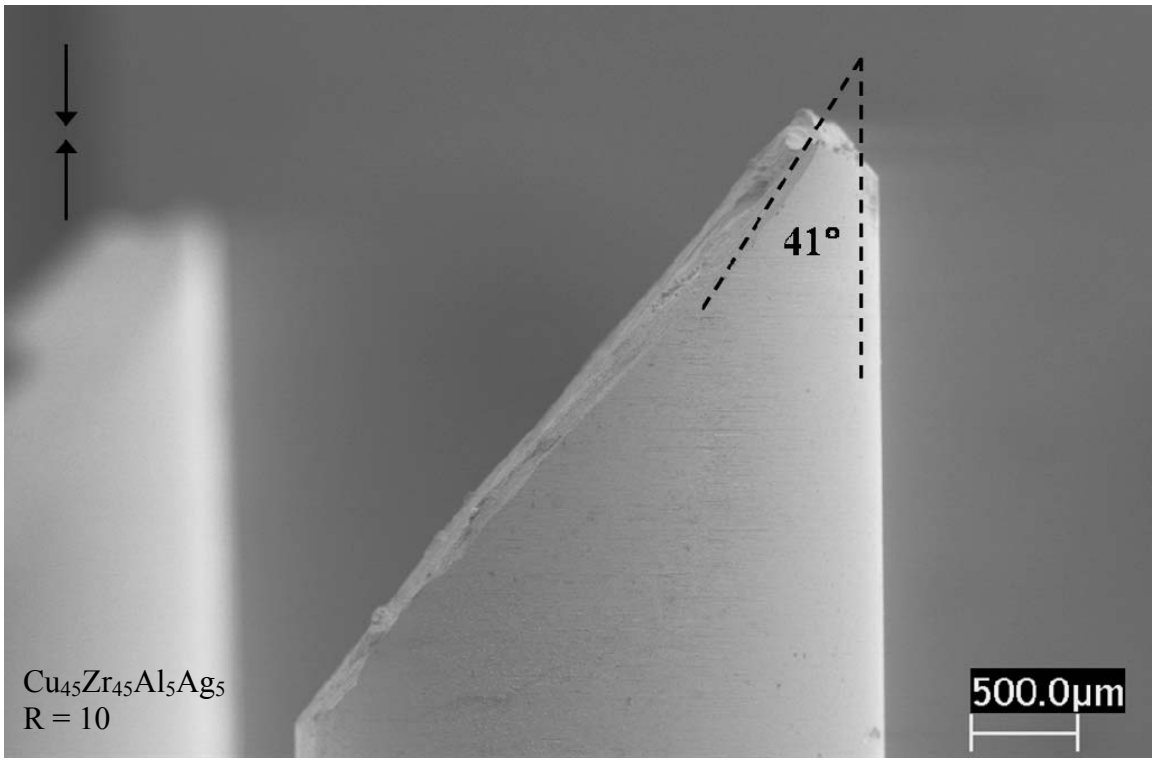

Figure 4-5: Fracture under cyclic compression always occurring in a purely shear mode. The fracture surface forms an θ_{cc} of 41° with respect to the loading axis, which is identical to the monotonic compressive fracture angle for the present $Cu_{45}Zr_{45}Al_5Ag_5$ BMG. The loading direction is indicated by the arrows in the top left corner.

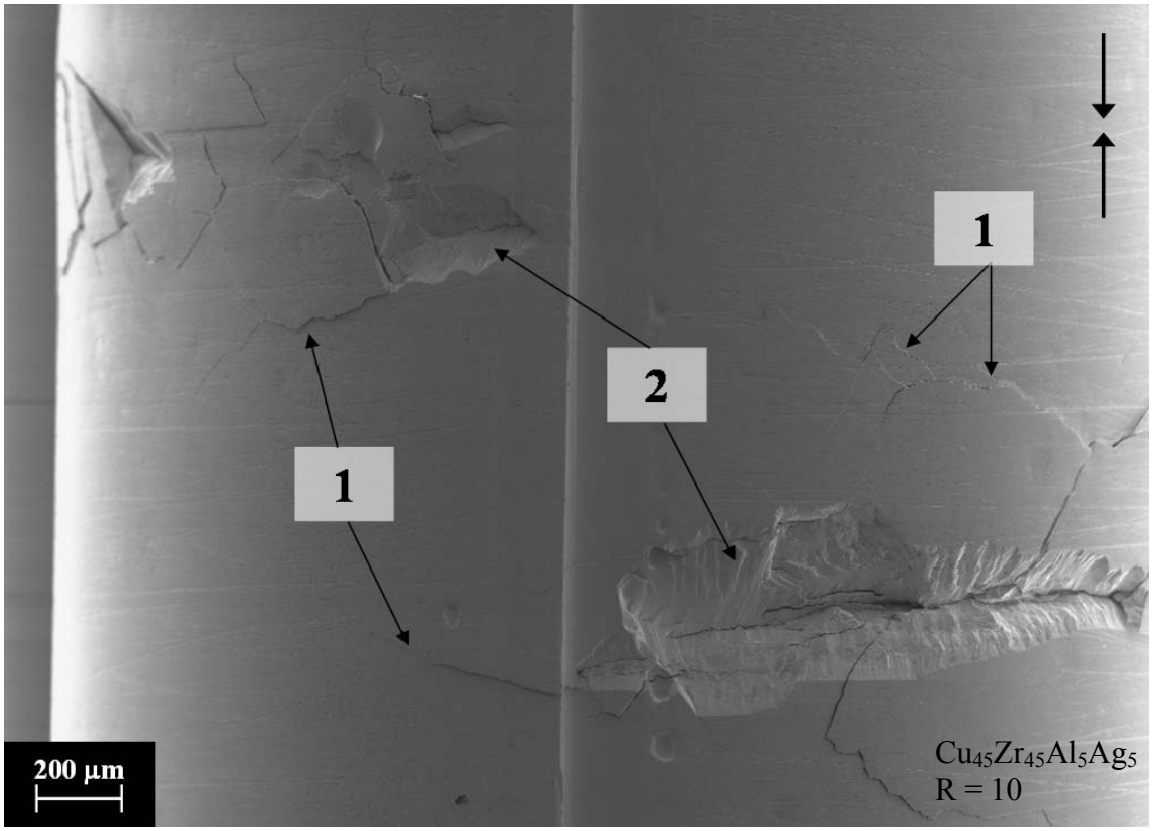

Figure 4-6: Significant damage on the outside surfaces of the fatigue specimens. Damage was in the form of: (1) shear bands and/or cracks (areas indicated by 1), and (2) chipped areas (indicated by 2). Arrows in the top right corner indicate the loading direction.

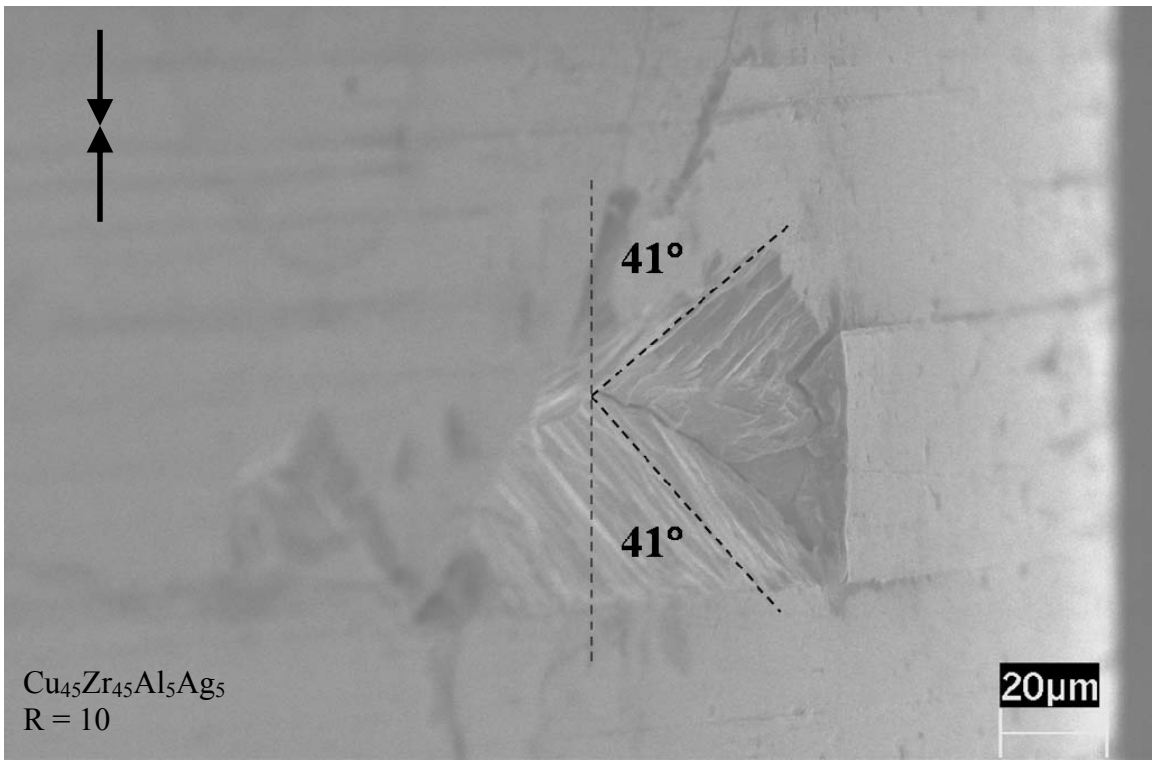

Figure 4-7: The fracture planes in the "chipped" areas also forming a θ_{chip} = 41° with respect to the loading axis. The arrows in the top left corner indicated the loading direction.

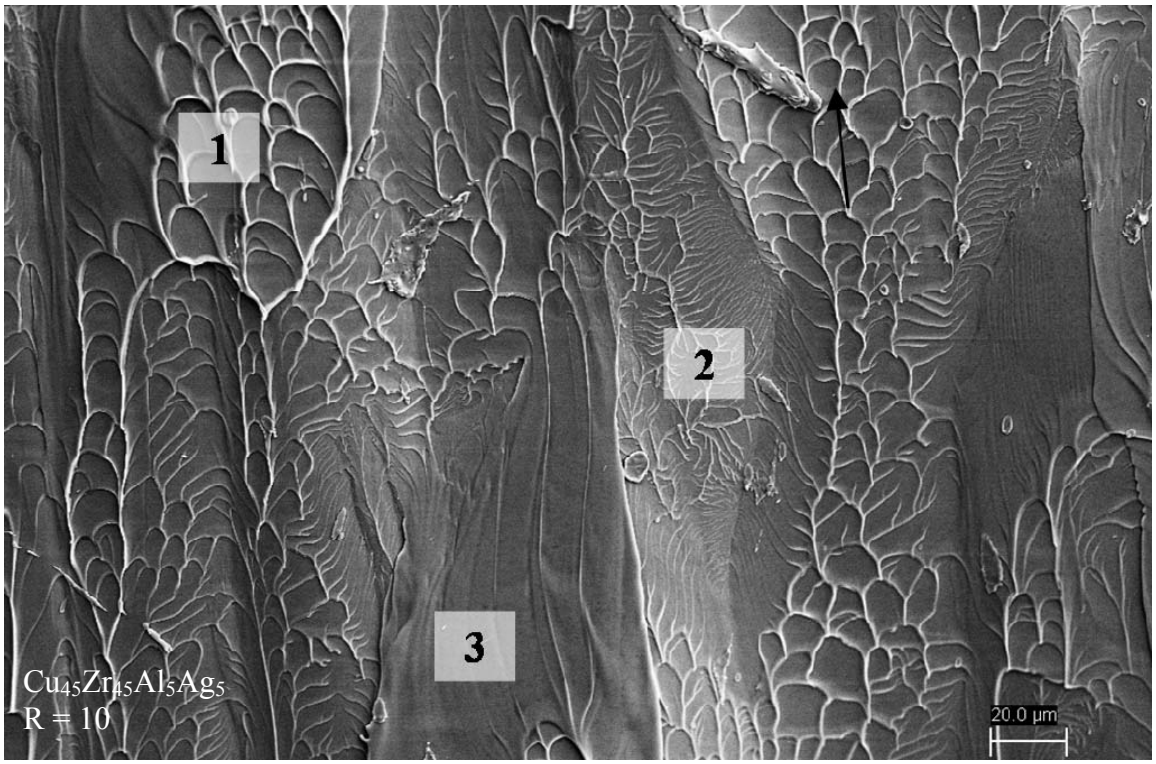

Figure 4-8: The fatigue fracture surfaces exhibiting features very similar to the monotonic fracture surface, namely: (1) a vein-like pattern (region 1), (2) small isolated regions of a river-like pattern (region 2), and (3) smooth regions (region 3). The arrow indicates the shear direction.

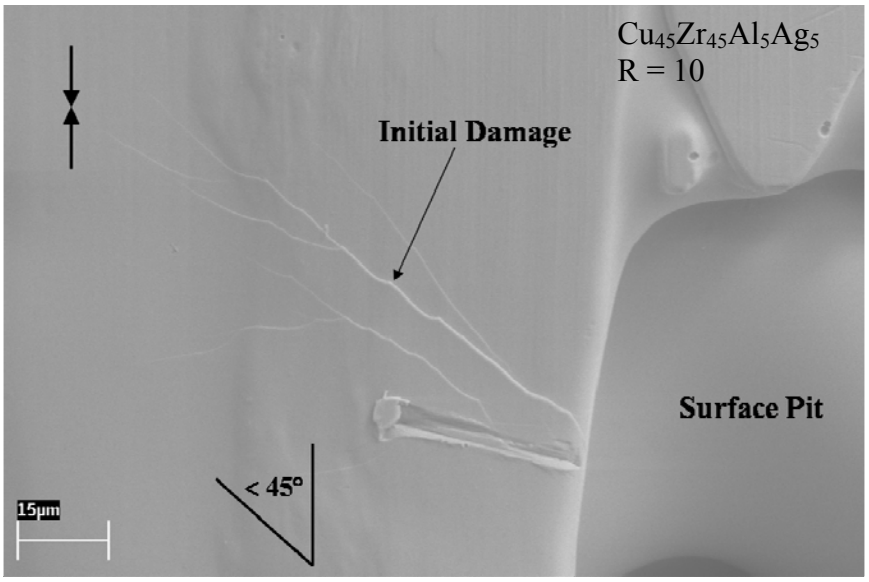

(a)

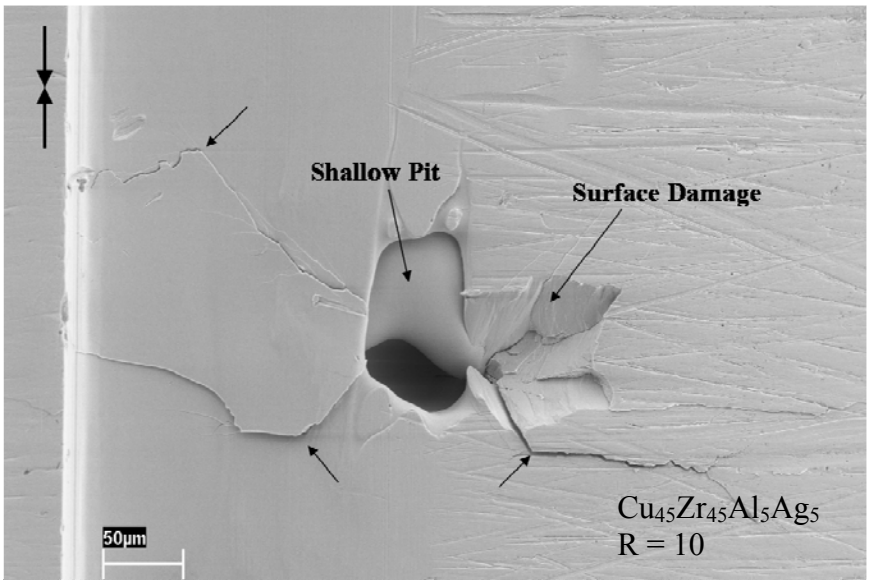

(b)

Figure 4-9: Fatigue damage evolution; (a) damage first initiating from a pre-existing surface pit, (b) cracks growing in size and the crack propagation direction changing.

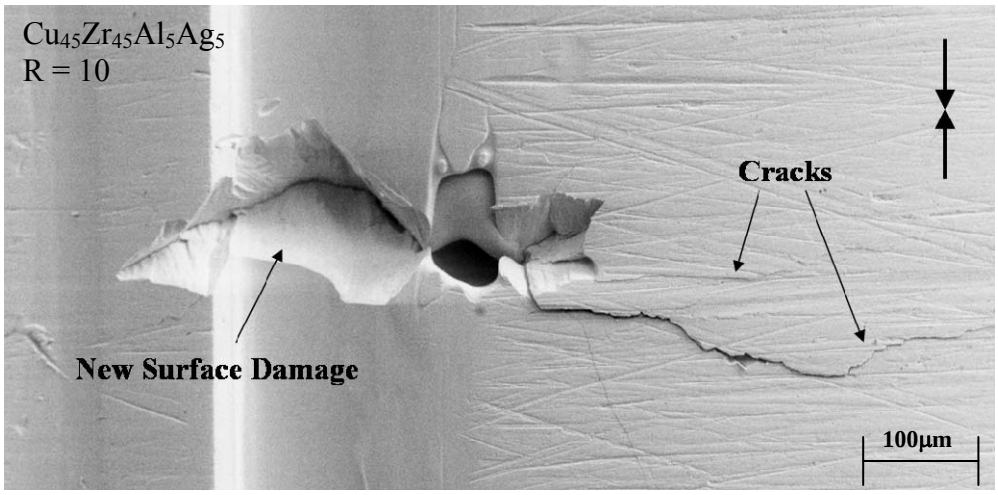

(c)

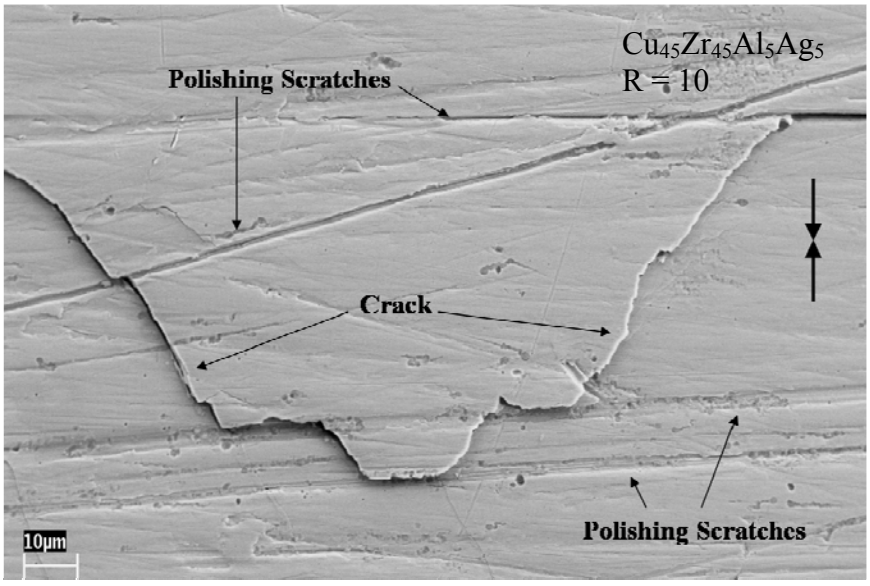

(d)

Figure 4-9: (continued) (c) cracks have continued to grow in a direction normal to the loading direction and a new area of surface damage has developed, (d) crack "jumping" from polishing scratches, and

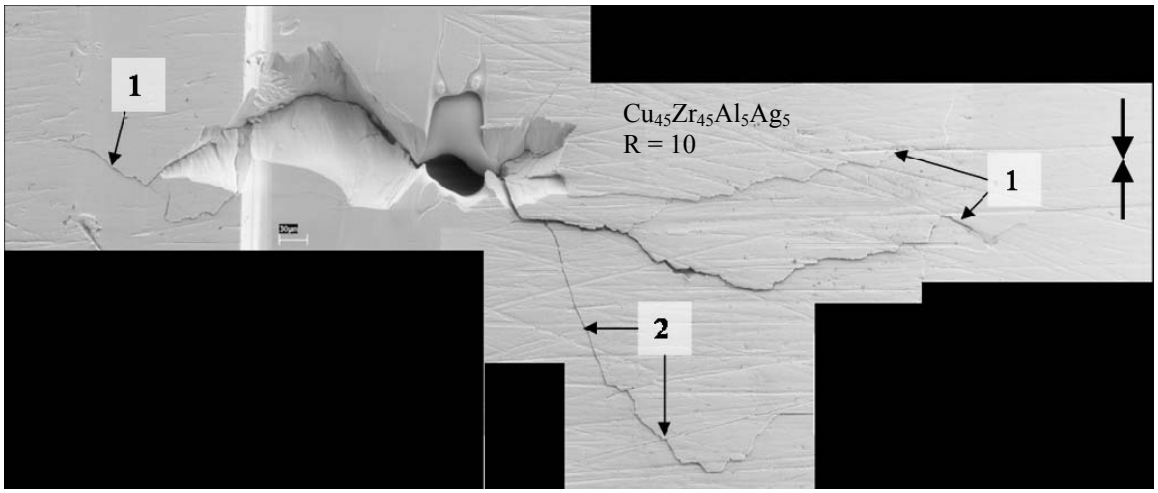

(e)

Figure 4-9: (continued) (e) cracks continuing to propagate in a direction perpendicular to the loading axis. Arrows indicated the loading direction.

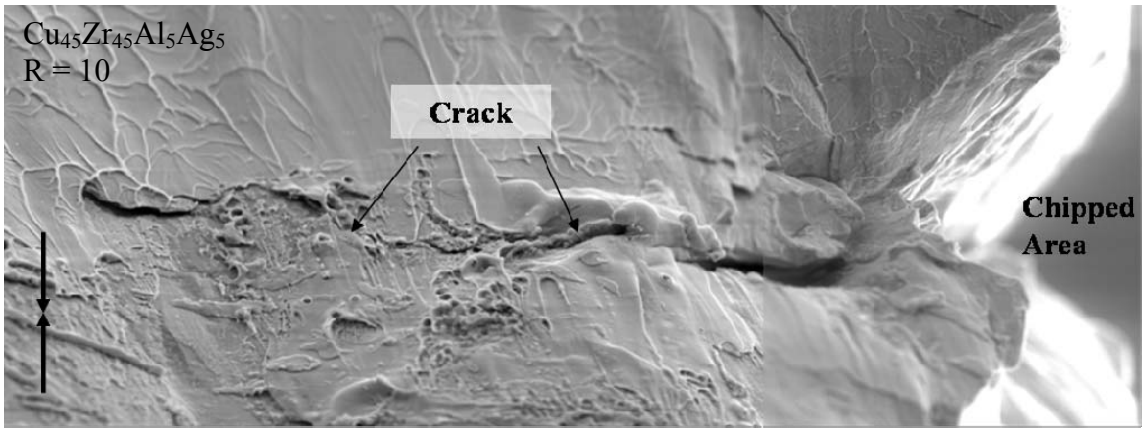

Figure 4-10: An area where the fracture plane cut through cracks and a chipped region. The crack propagation path is perpendicular to the loading direction.

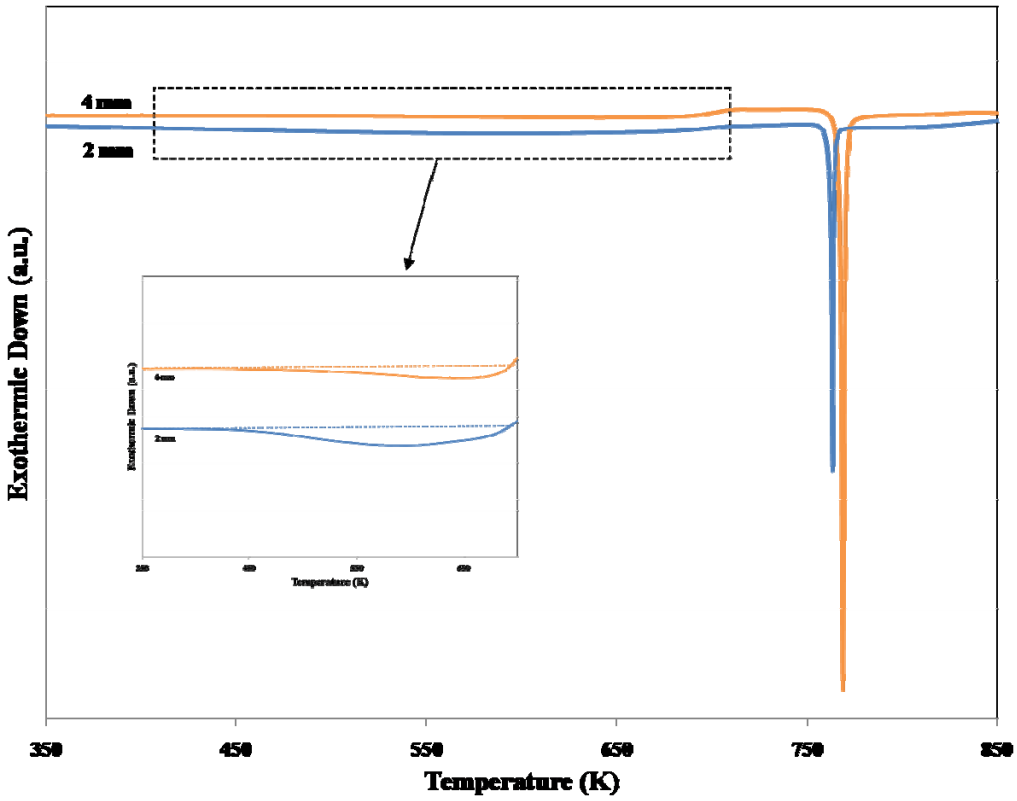

Figure 4-11: DSC curves for both the 2 and 4 mm samples. The ΔH for the 2 and 4 mm samples are - 44.9 J/g and - 27.0 J/g, respectively.

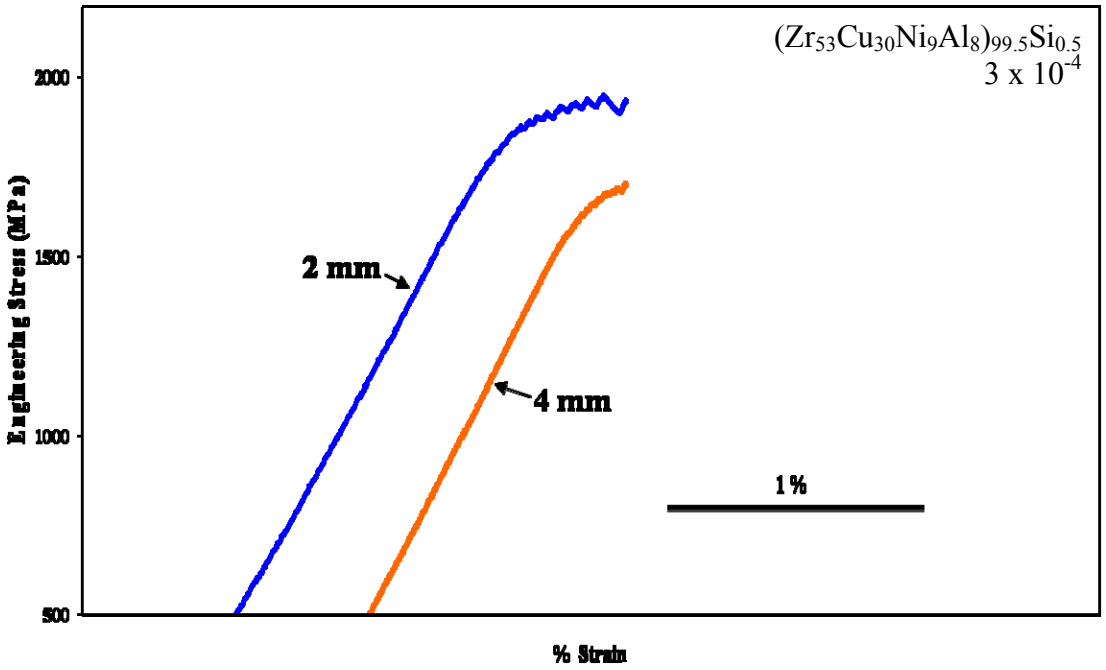

Figure 4-12: Monotonic compressive stress-strain behavior of the BMG for the 2 and 4 mm samples. For the 2 mm samples, σ_Y, σ_F, and ε_P were approximately 1750 MPa, 1950 MPa, and 0.55, respectively. For the 4 mm samples, the σ_Y, σ_F, and ε_P were approximately 1650 MPa, 1705 MPa, and 0.18, respectively.

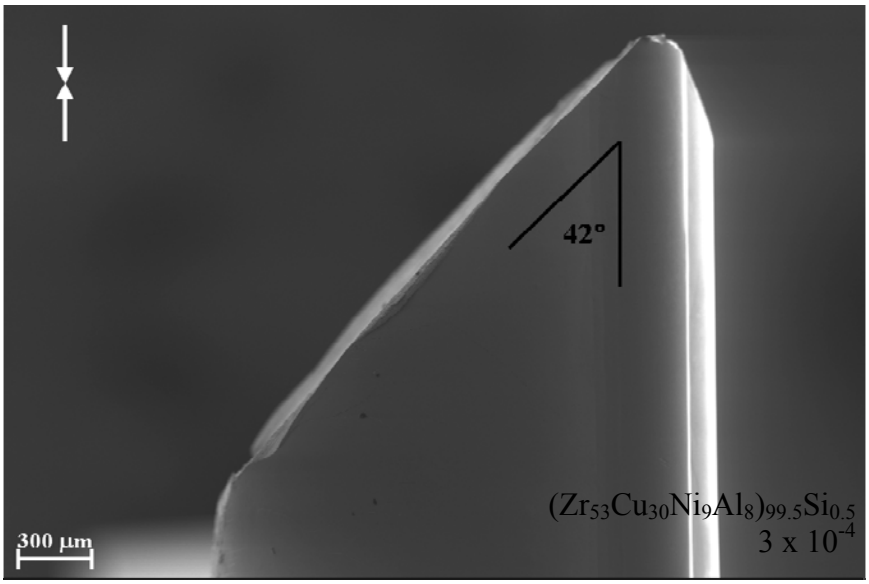

(a)

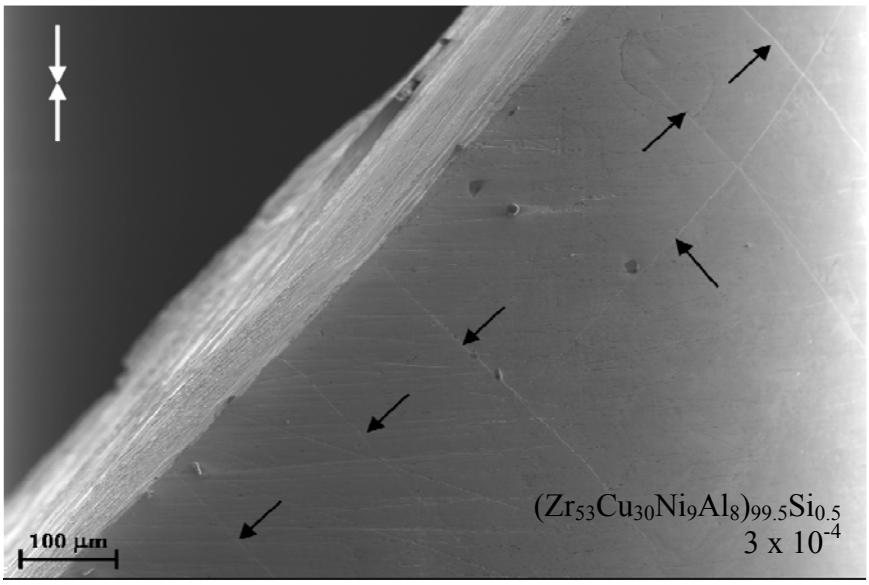

(b)

Figure 4-13: Monotonic compression fracture characteristics of the 2 mm $(Zr_{53}Cu_{30}Ni_9Al_8)_{99.5}Si_{0.5}$ BMG; (a) the fracture plane (loading direction is indicated by the arrows on the top left corner), (b) outside surfaces (loading direction is indicated by the arrows on the top left corner).

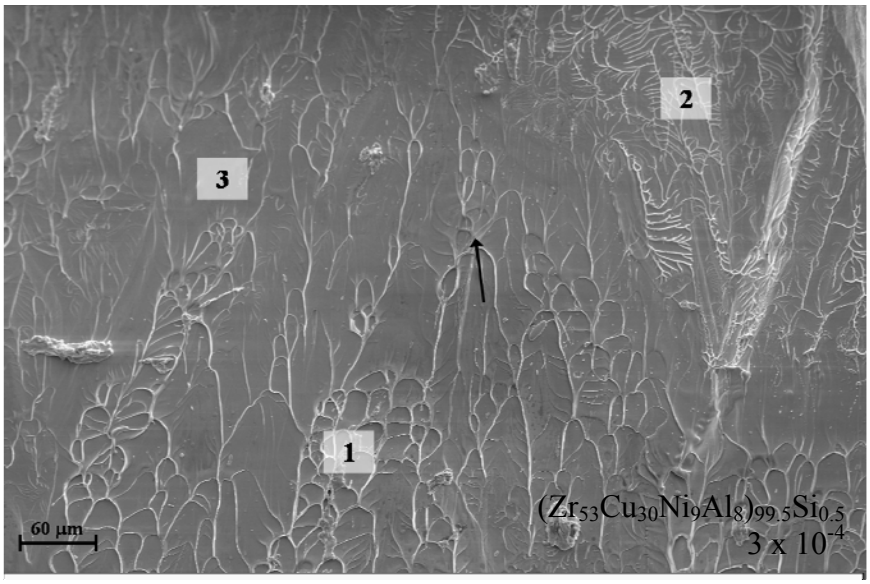

(c)

Figure 4-13: (continued) (c) fracture surface.

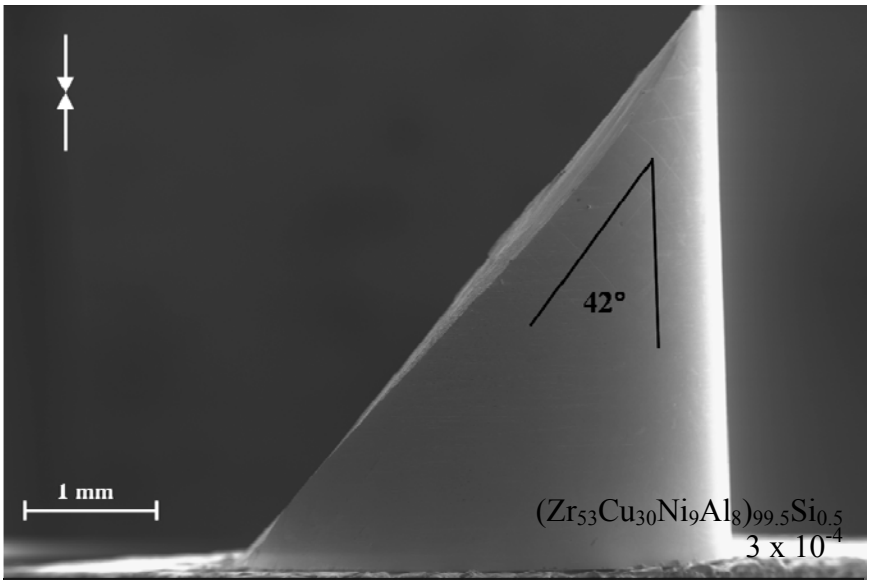

(a)

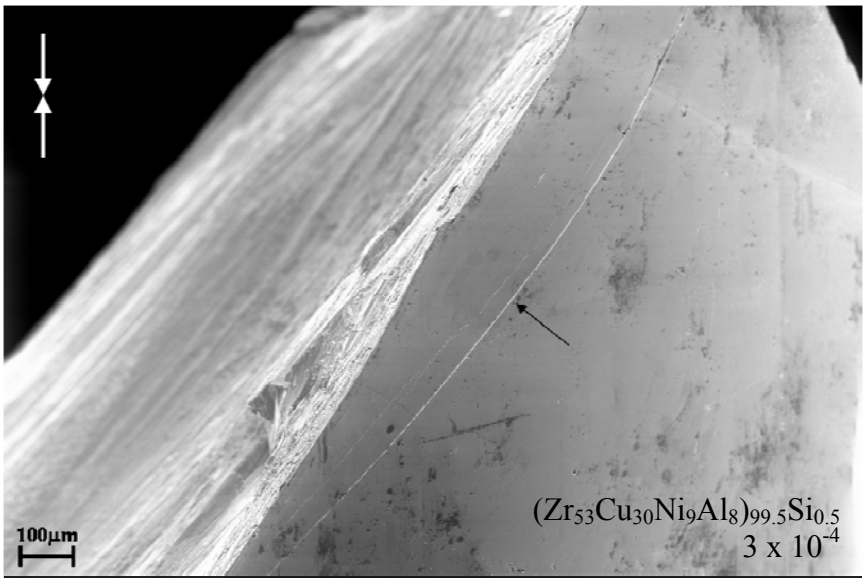

(b)

Figure 4-14: Monotonic compression fracture characteristics of the 4 mm $(Zr_{53}Cu_{30}Ni_9Al_8)_{99.5}Si_{0.5}$ BMG; (a) the fracture plane (loading direction is indicated by the arrows on the top left corner), (b) outside surfaces (loading direction is indicated by the arrows on the top left corner).

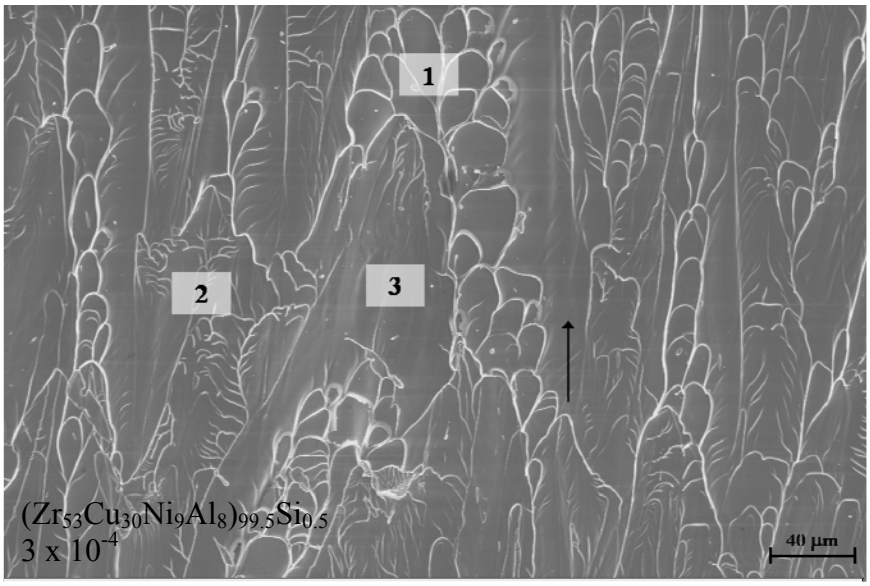

(c)

Figure 4-14: (continued) (c) fracture surface.

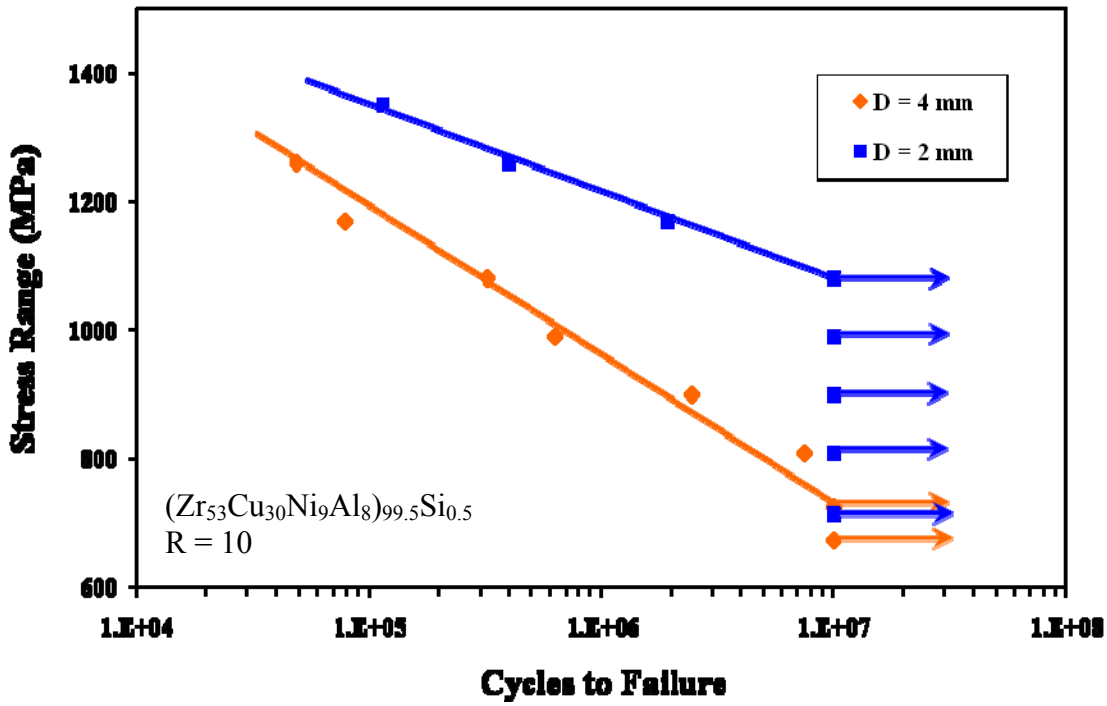

Figure 4-15: The N_f measured as a function of the applied σ_R for both 2 and 4 mm samples.

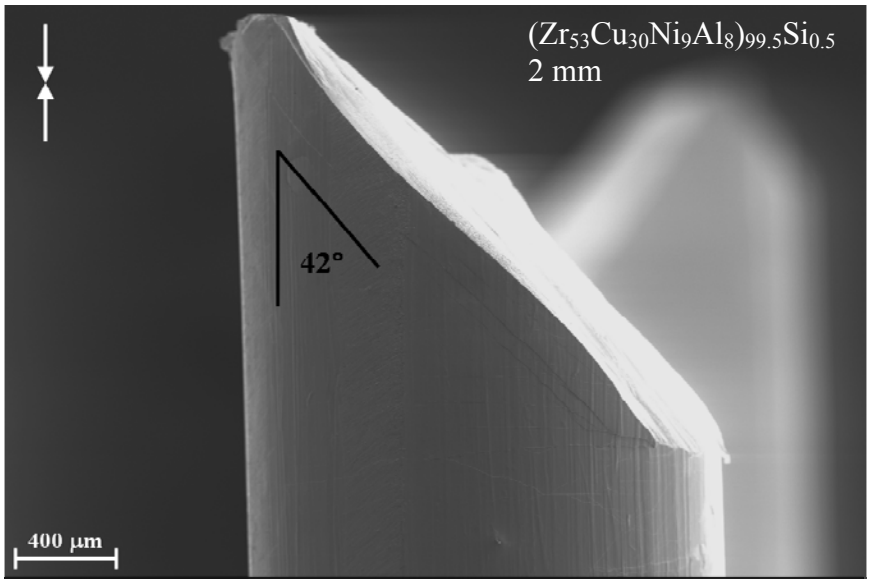

(a)

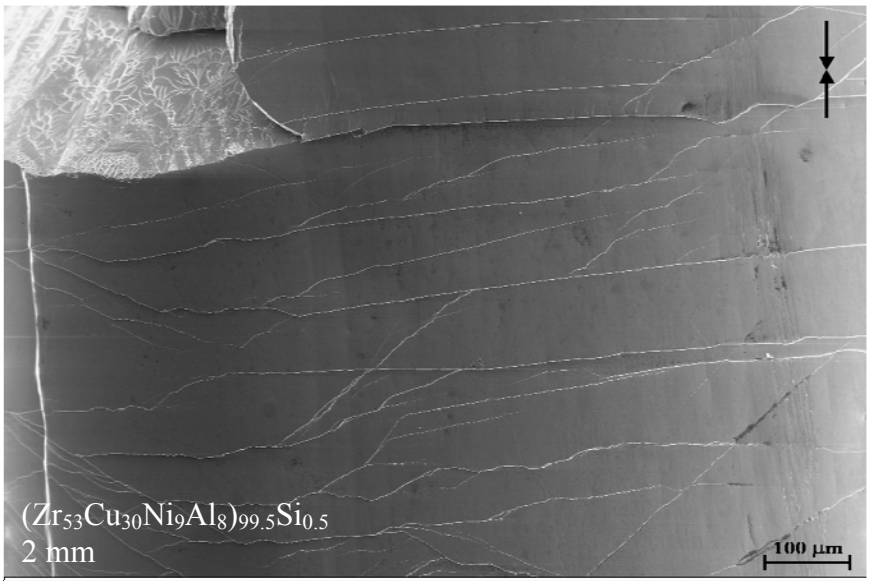

(b)

Figure 4-16: Cyclic compression fracture characteristics for the 2 mm $(Zr_{53}Cu_{30}Ni_9Al_8)_{99.5}Si_{0.5}$ BMG samples; (a) fracture plane (arrows in the top left corner indicate the loading direction); (b) outside surfaces (arrows in the top right corner indicate the loading direction).

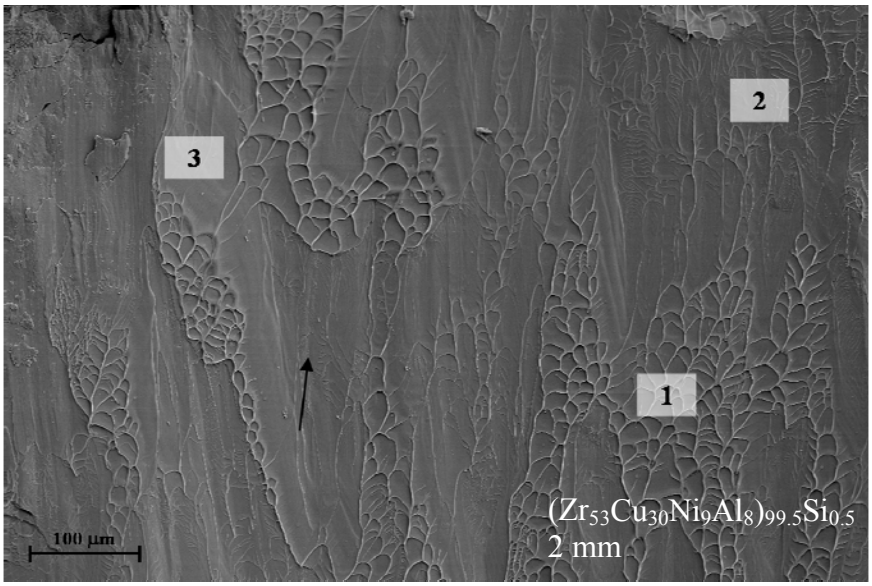

(c)

Figure 4-16: (continued) (c) fracture surface.

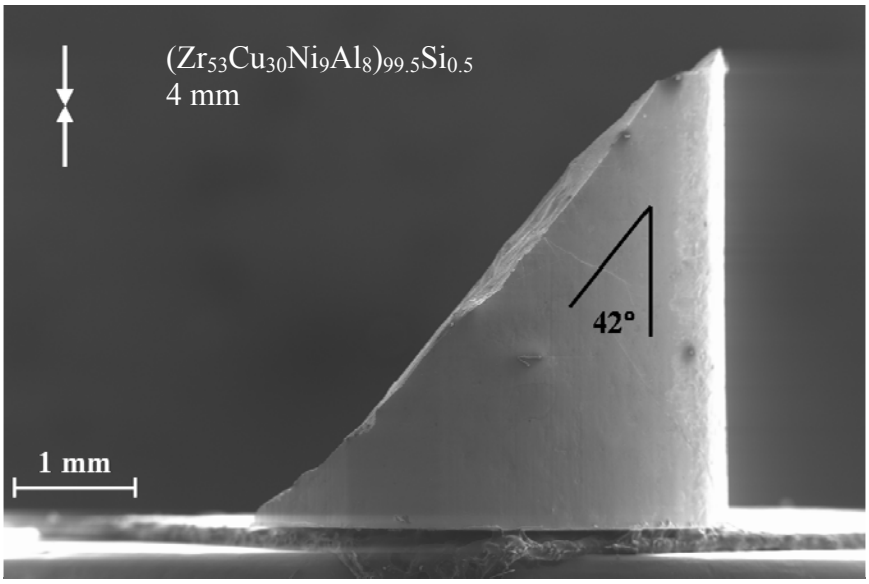

(a)

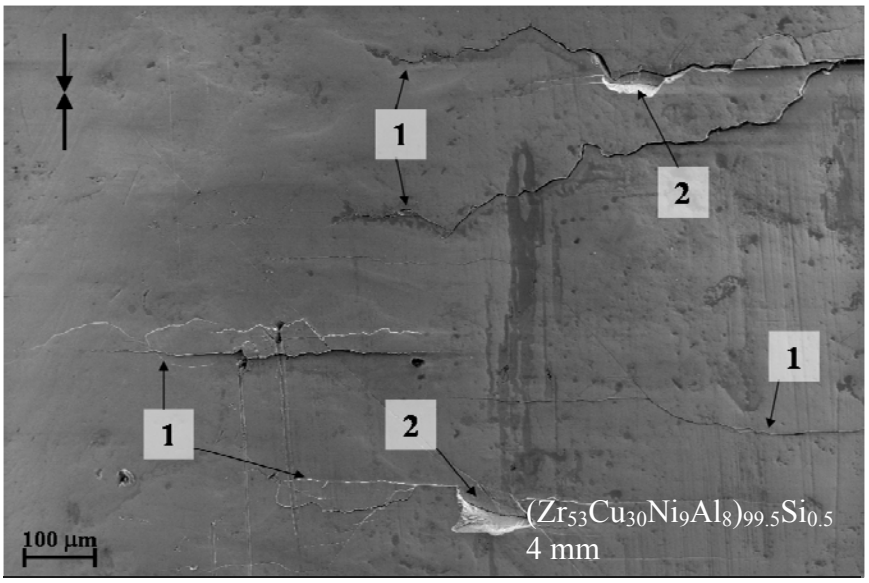

(b)

Figure 4-17: Cyclic compression fracture characteristics for the 4 mm $(Zr_{53}Cu_{30}Ni_9Al_8)_{99.5}Si_{0.5}$ BMG samples; (a) fracture plane (arrows in the top left corner indicate the loading direction); (b) outside surfaces (arrows in the top right corner indicate the loading direction).

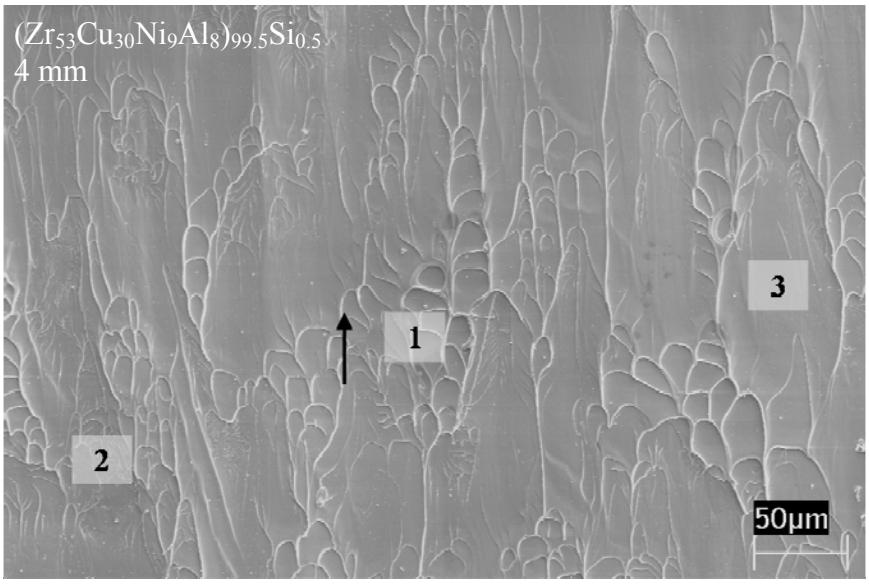

(c)

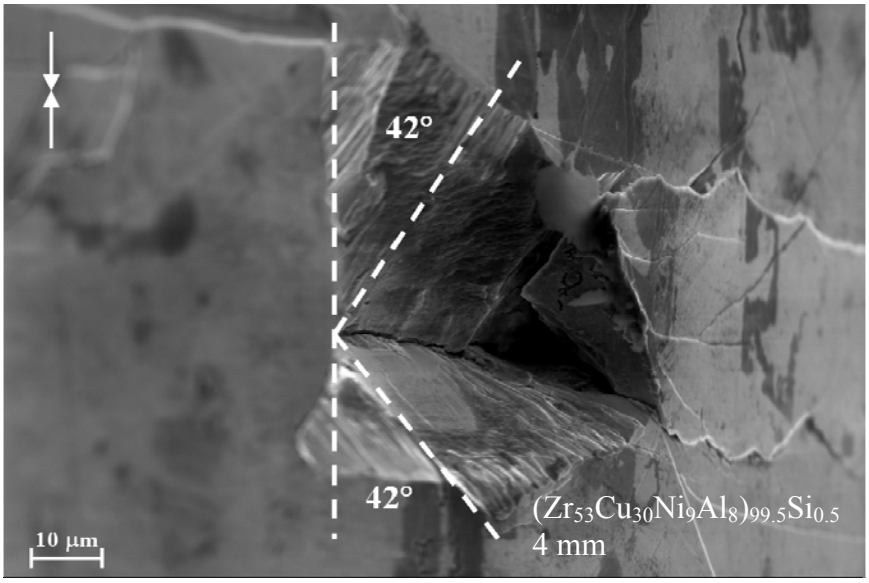

(d)

Figure 4-17: (continued) (c) fracture surface, and (d) chipped area.

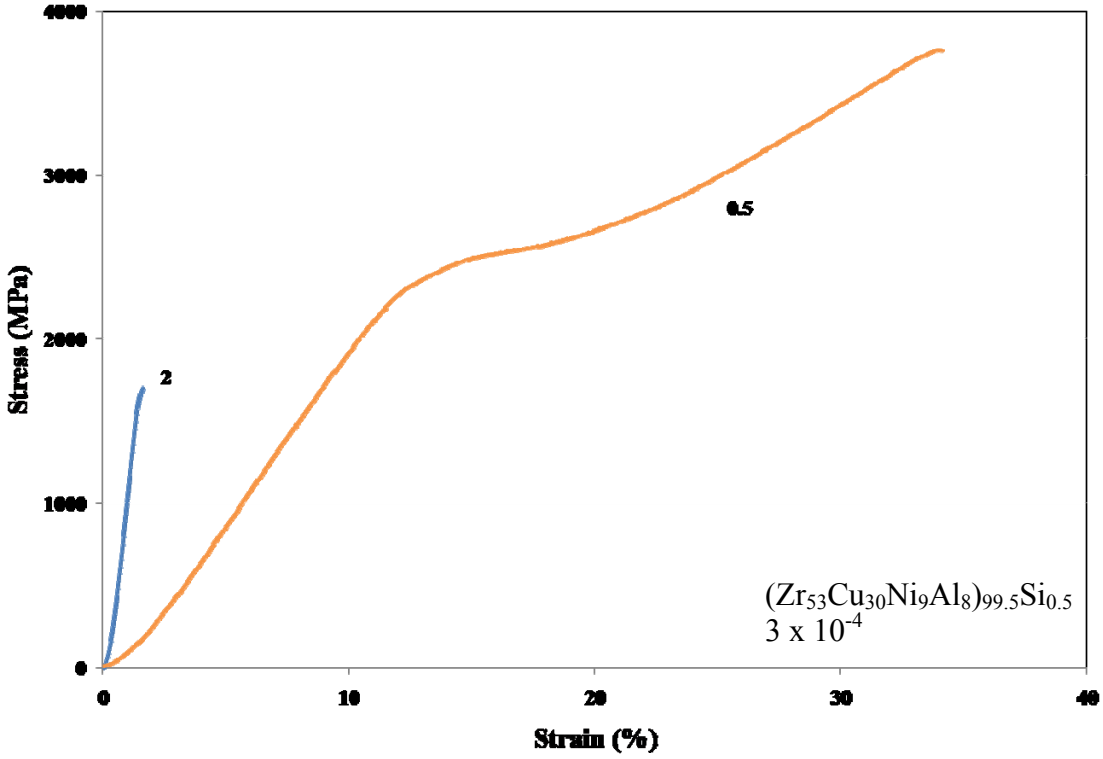

Figure 4-18: Monotonic compressive stress-strain behavior for the $Zr_{53}Cu_{30}Ni_9Al_8$ BMG for aspect ratios of 0.5 and 2.

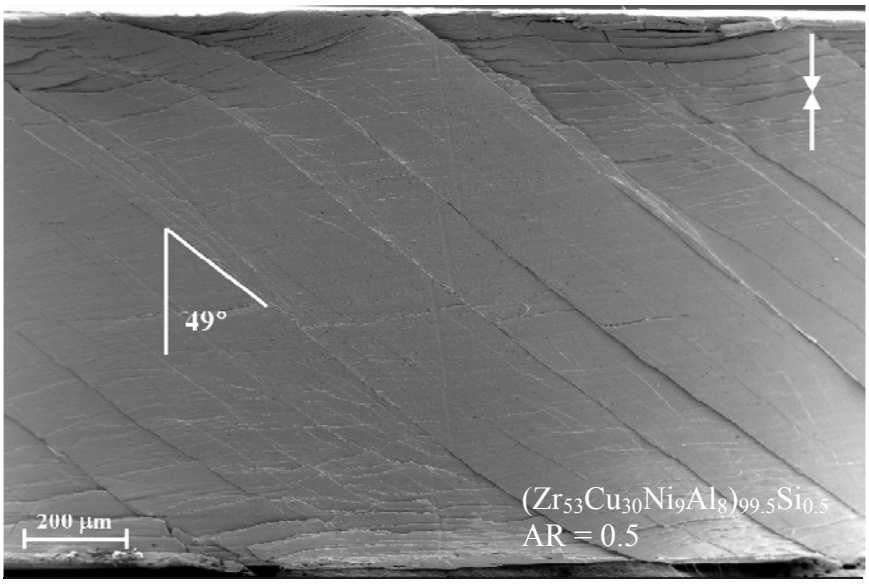

(a)

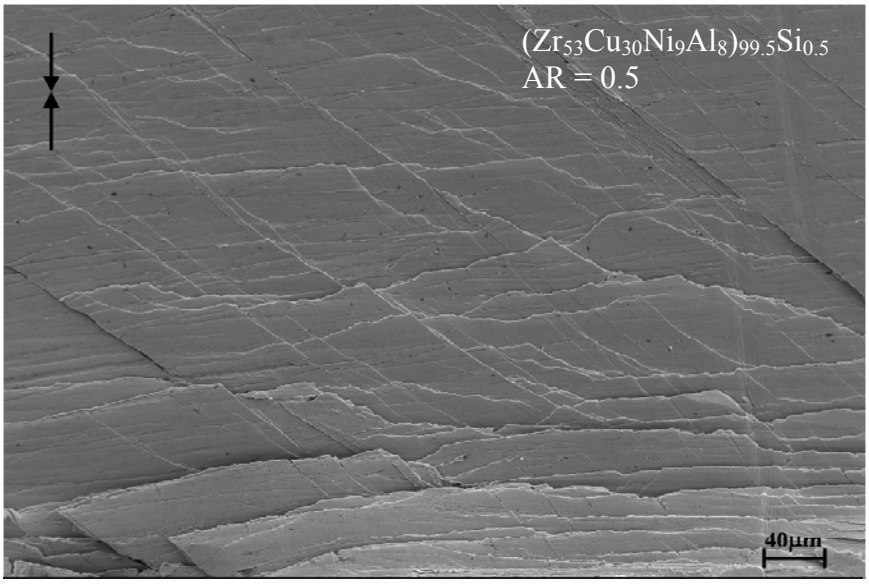

(b)

Figure 4-19: Monotonic compression fracture characteristics for the $Zr_{53}Cu_{30}Ni_9Al_8$ BMG with an aspect ratio of 0.5; (a) outside surface of a sample strained to 29%, (b) outside surface near the interface of the specimen and the platen.

(c)

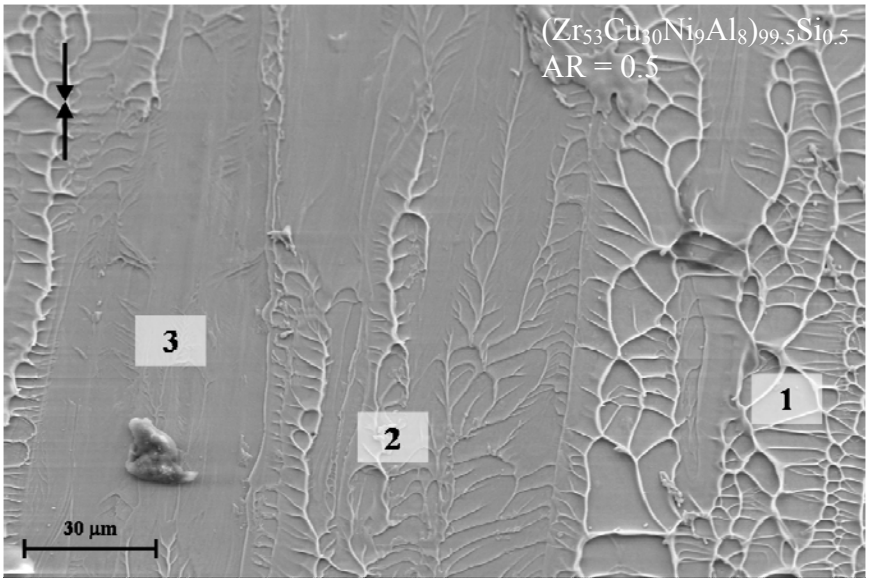

(d)

Figure 4-19: (continued) (c) fractured sample, and (d) fracture surface.

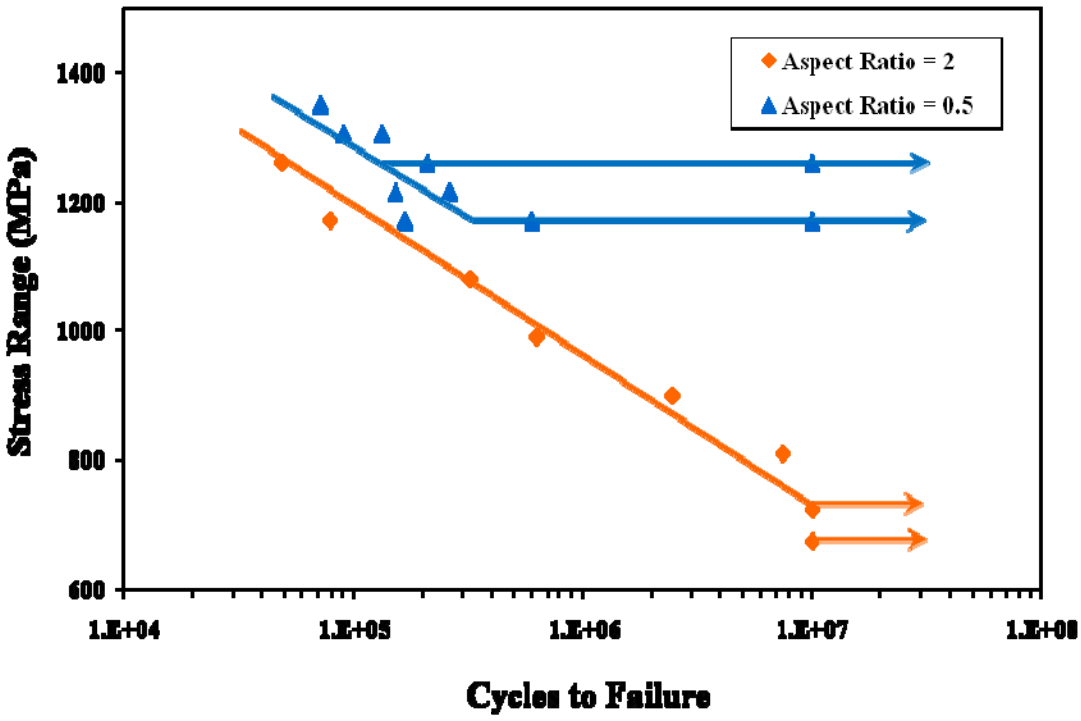

Figure 4-20: The N_f measured as a function of the applied σ_R for the $Zr_{53}Cu_{30}Ni_9Al_8$ BMG with aspect ratios of 0.5 and 2.

(a)

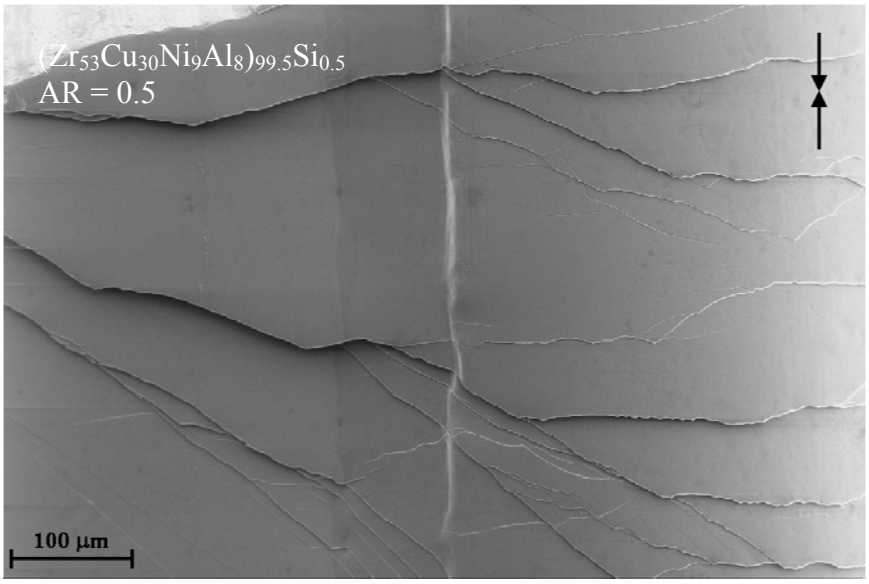

(b)

Figure 4-21: The cyclic compressive fracture characteristics for the $Zr_{53}Cu_{30}Ni_9Al_8$ BMG with an aspect ratio of 0.5; (a) fractured sample, (b) outside surface.

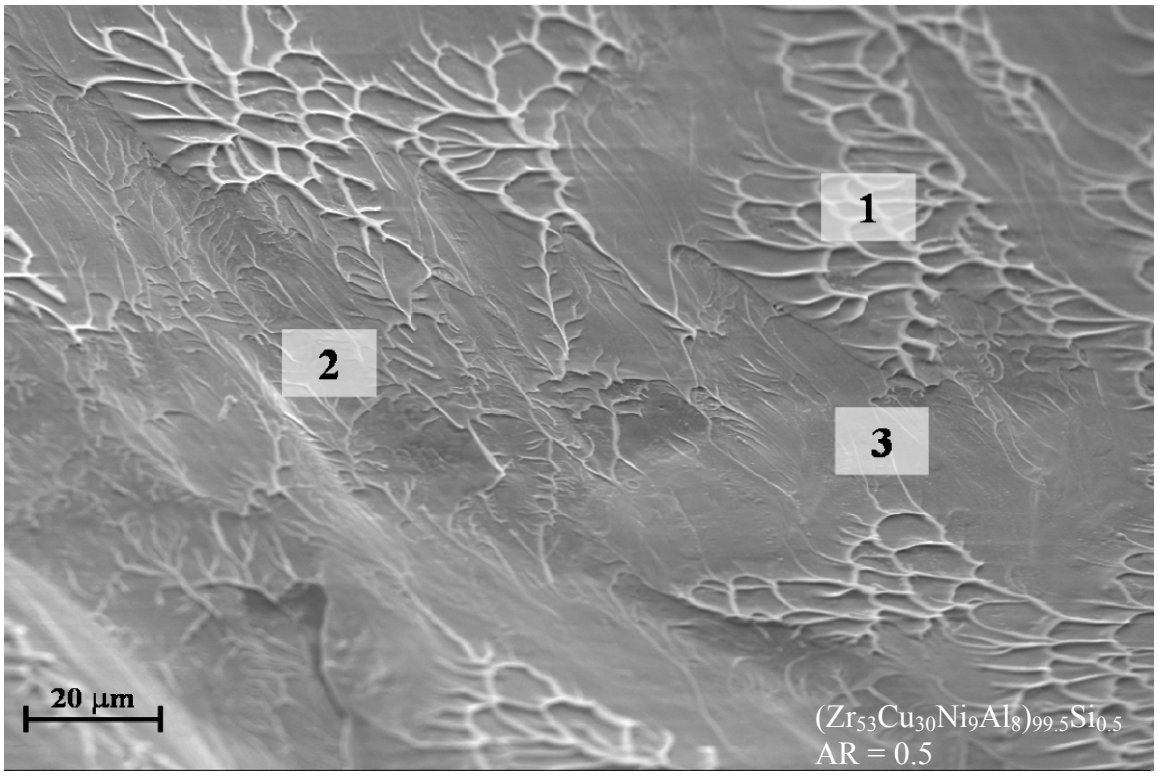

(c)

Figure 4-21: (continued) (c) fracture surface.

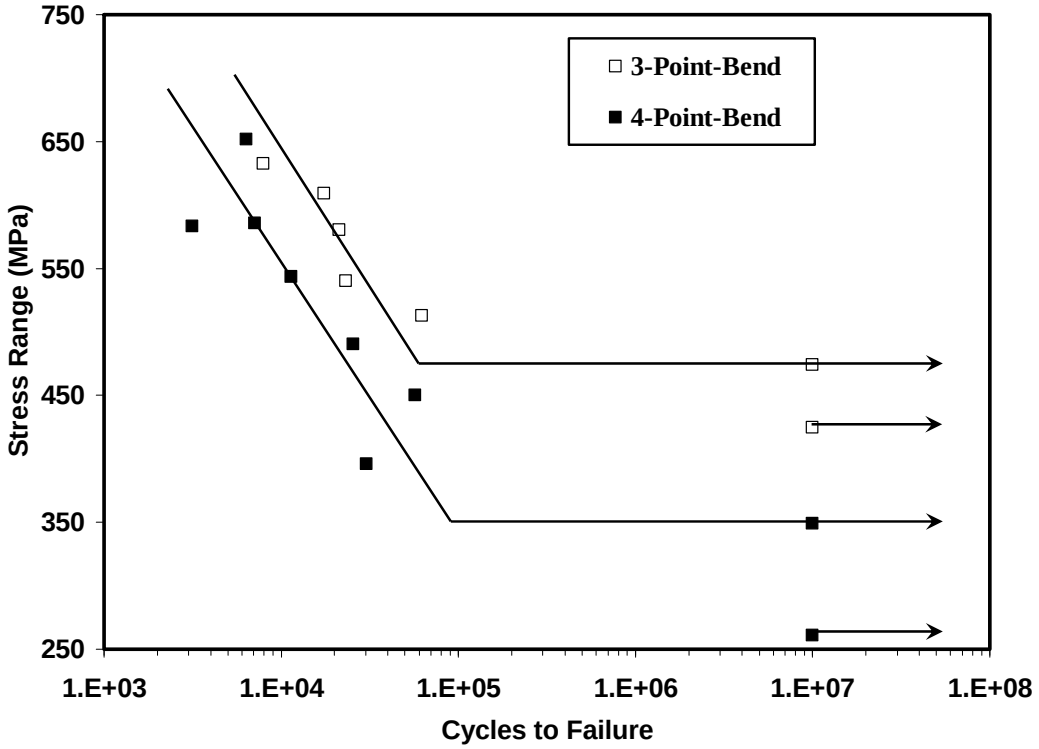

Figure 4-22: N_f measured as a function of the applied σ_R, showing both 3PB and 4PB loading conditions. R ratio was 0.1 and the frequency was 10 Hz in an air environment.

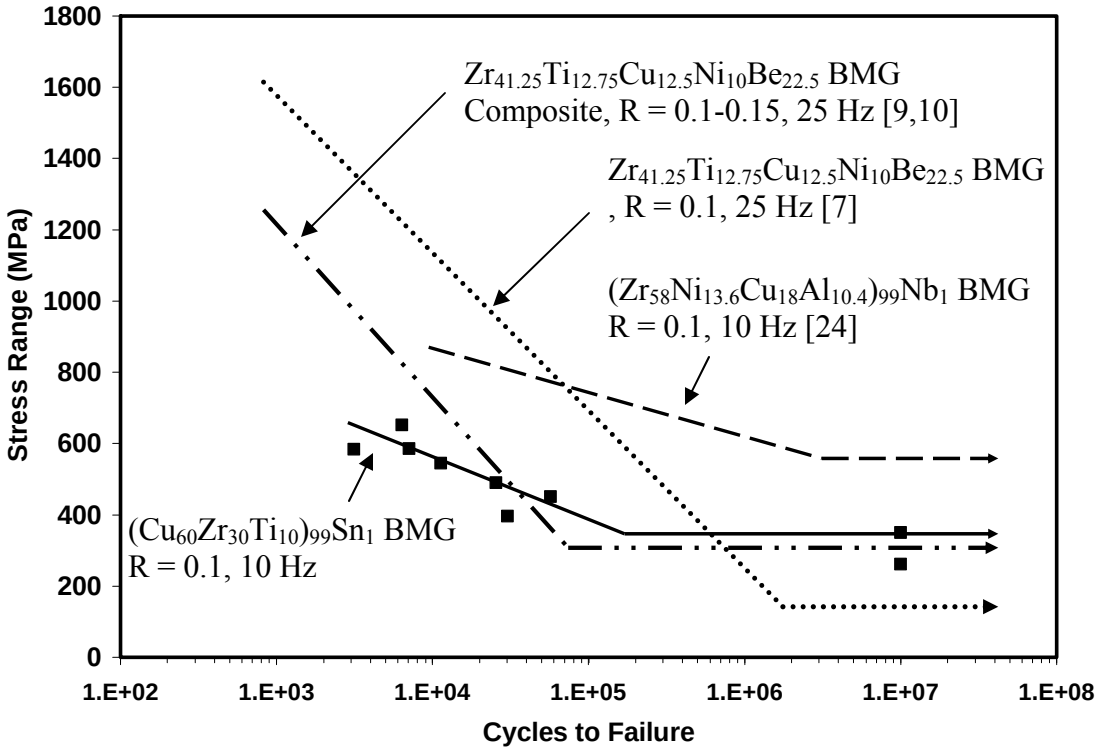

Figure 4-23: Comparisons of 4PB fatigue S-N data for Zr-based BMGs, a Zr-based composite, and the present Cu-based BMG.

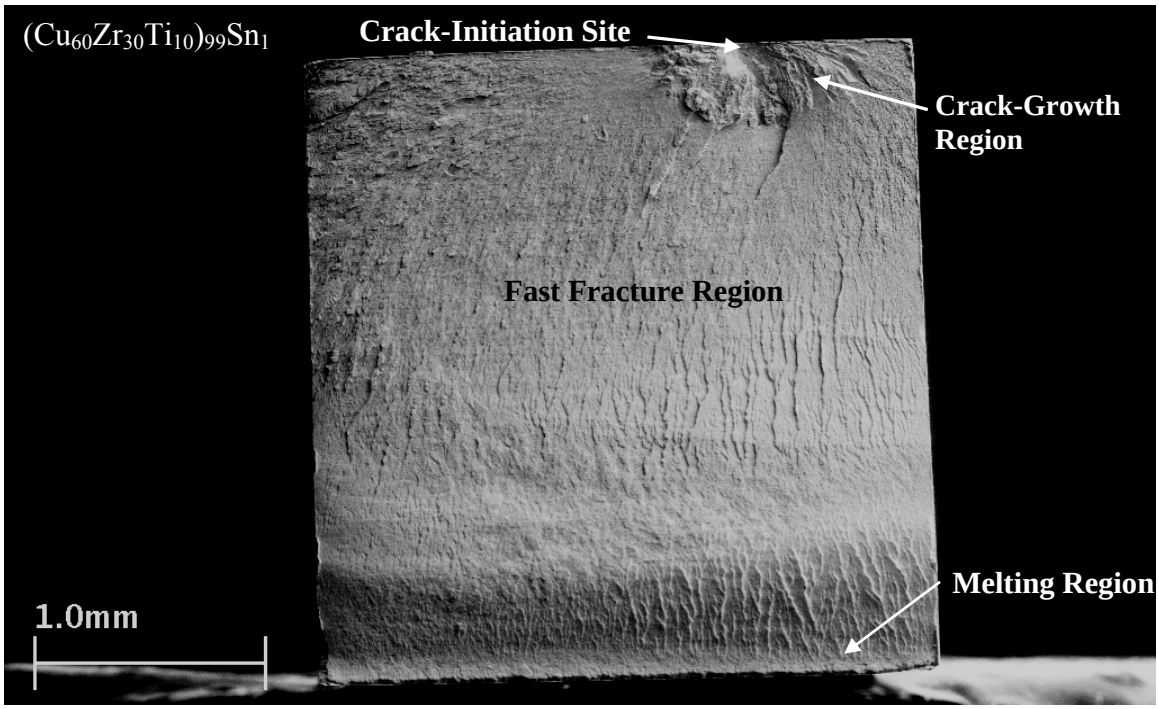

Figure 4-24: A typical overall fatigue fracture surface showing the locations of the crack-initiation site, stable crack-growth region, unstable fast-fracture region, and melting region. Specimen tested under 3PB loading conditions, σ_R = 580 MPa, R = 0.1, frequency = 10 Hz, in air environment.

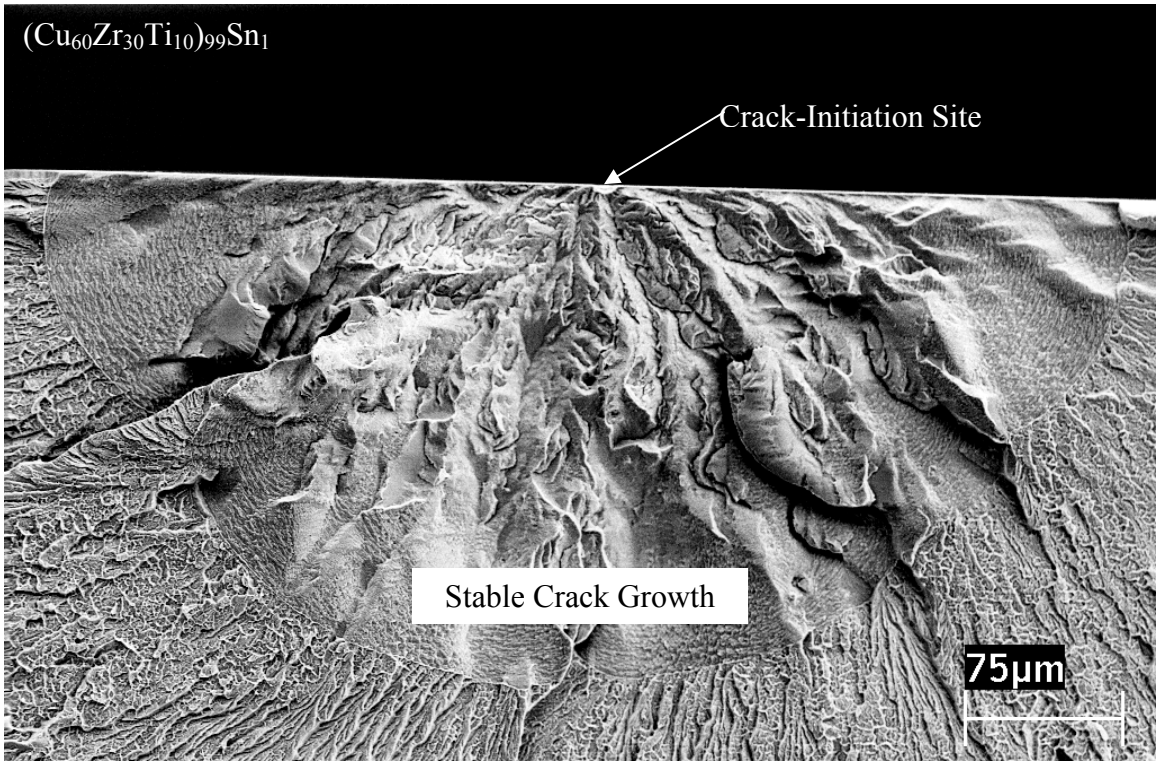

(a)

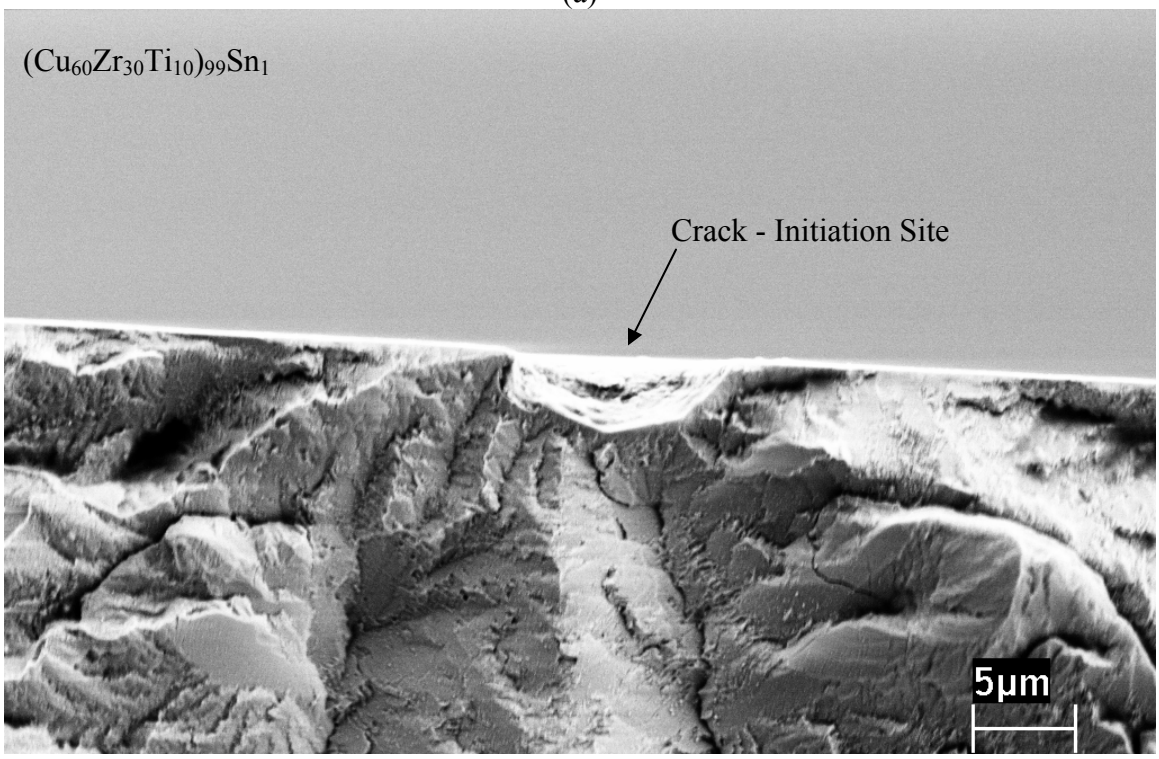

(b)

Figure 4-25: (a) Typical crack-initiation site and crack-growth region, (b) Higher magnification of the crack-initiation site of sample shown in (a).

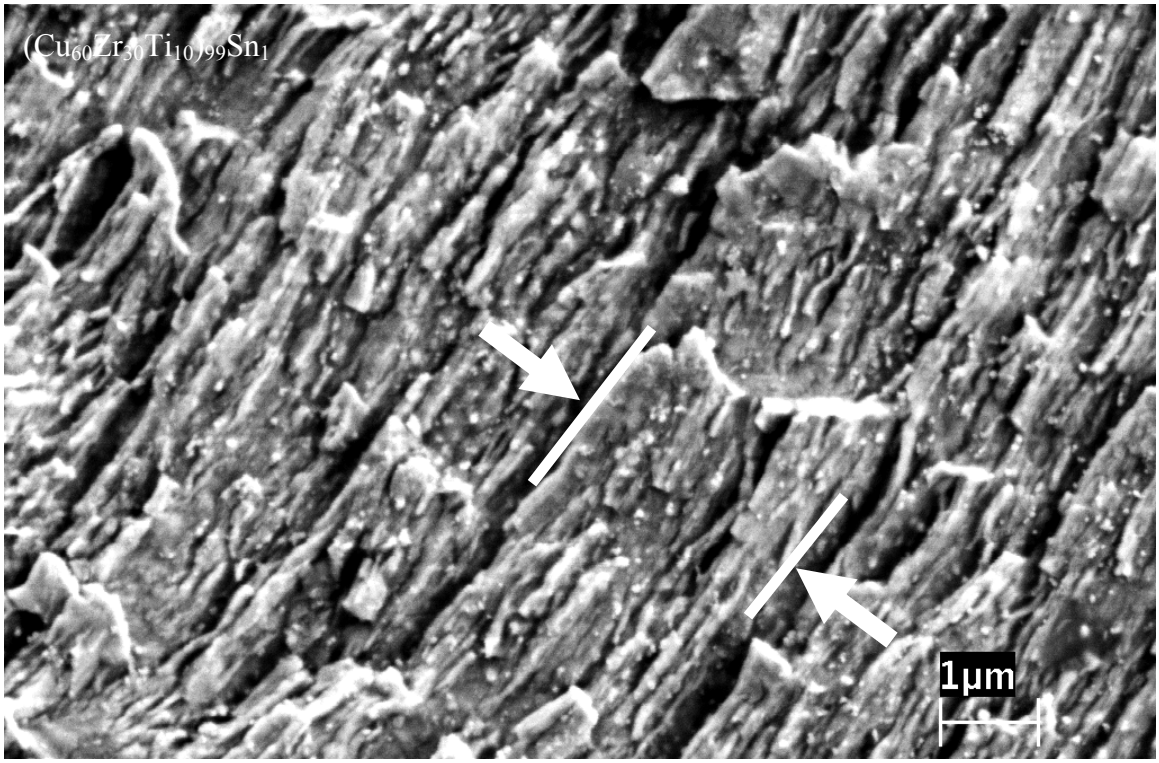

(c)

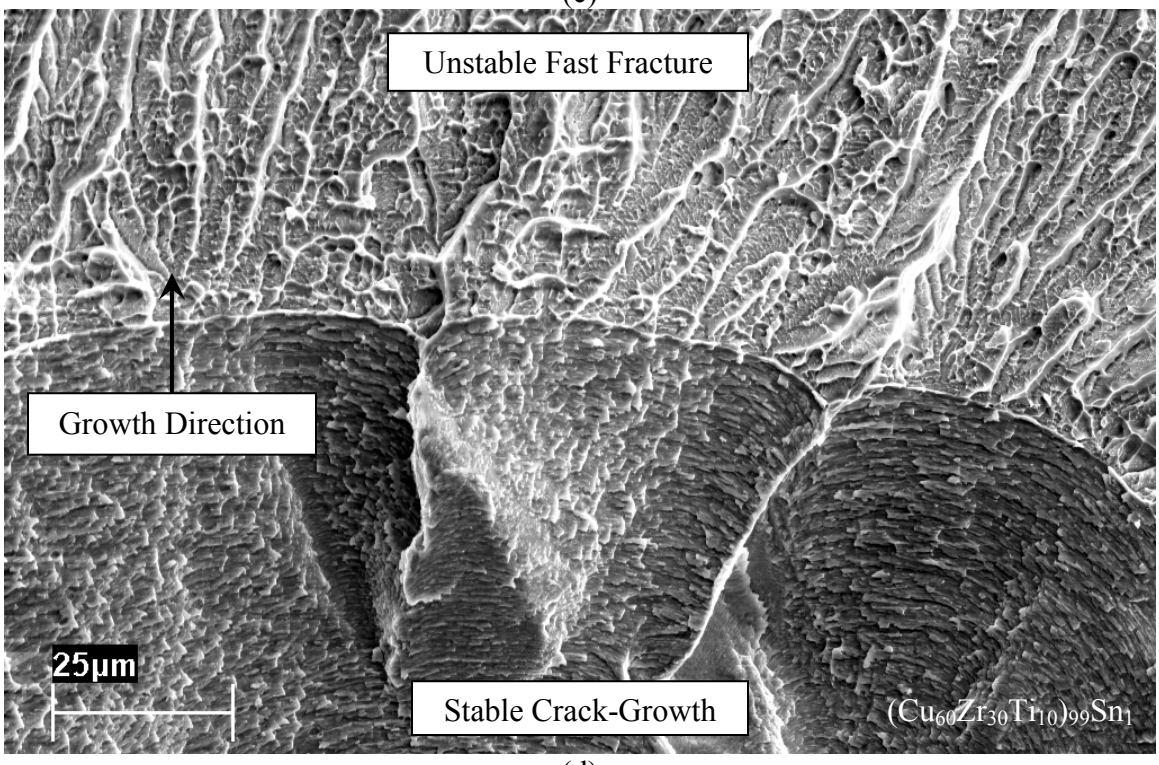

(d)

Figure 4-25: (continued) (c) Fatigue striations, (d) Transition from a stable crack-growth to unstable fast fracture.

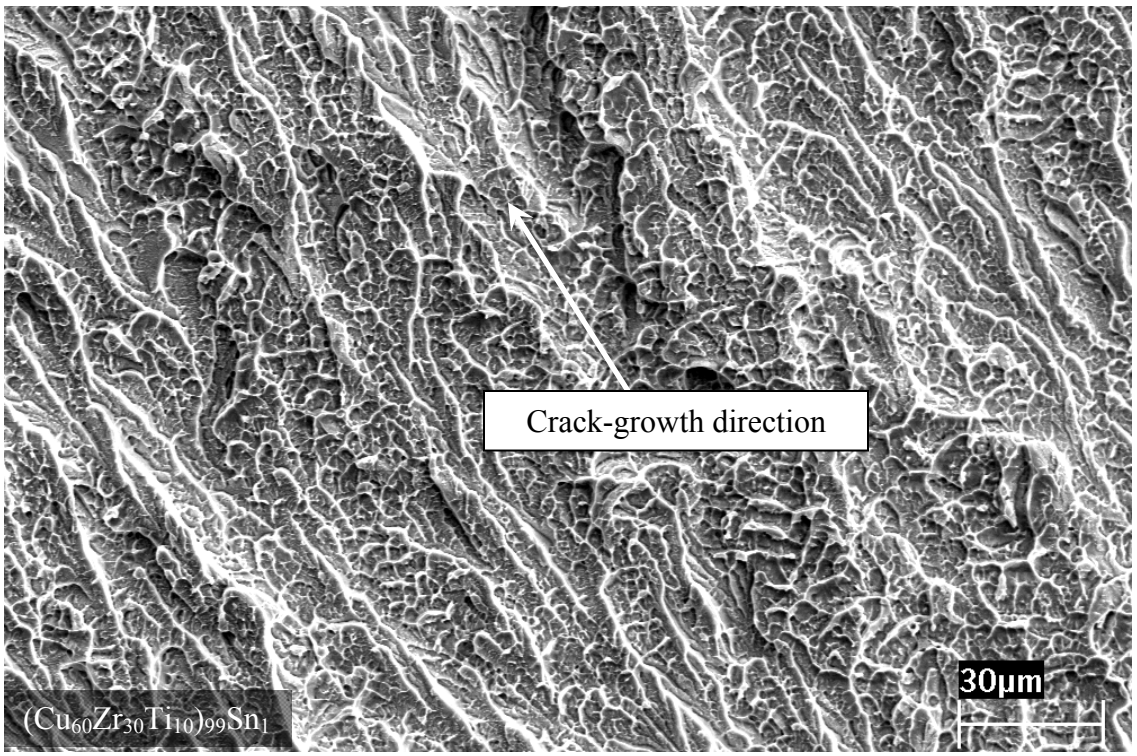

(e)

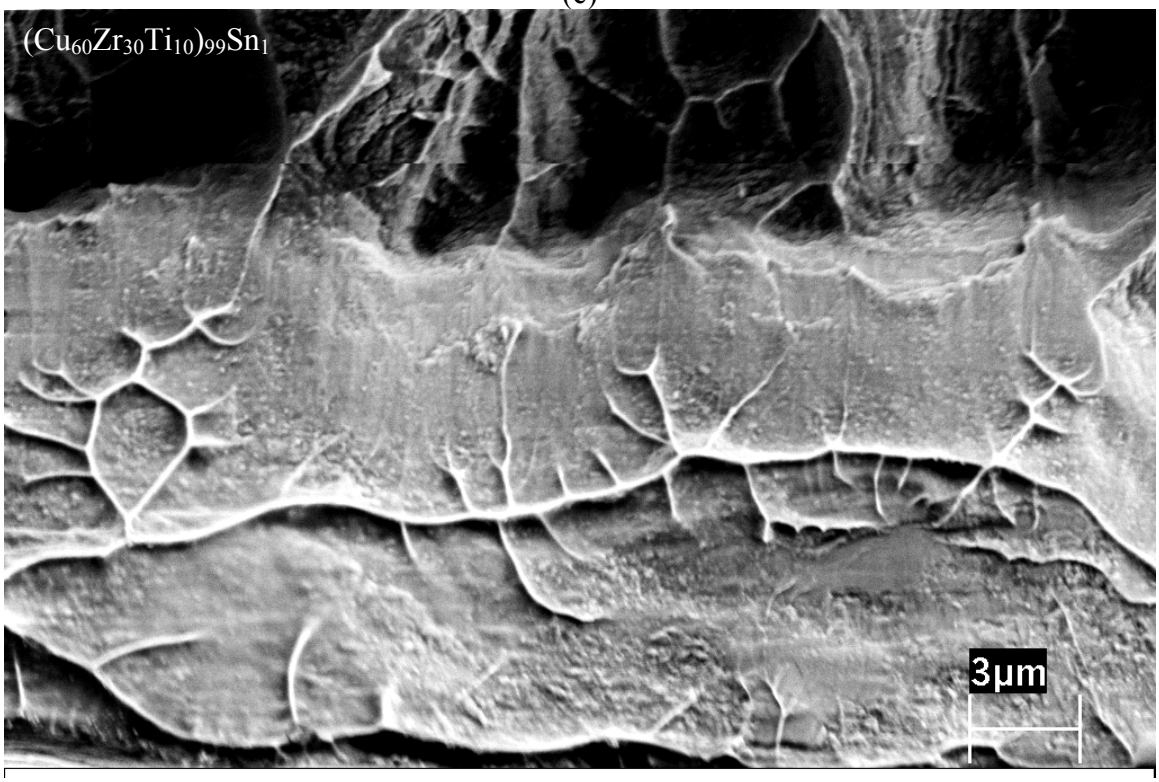

(f)

Figure 4-25: (continued) (e) Unstable fast-fracture region, (f) Melting region.

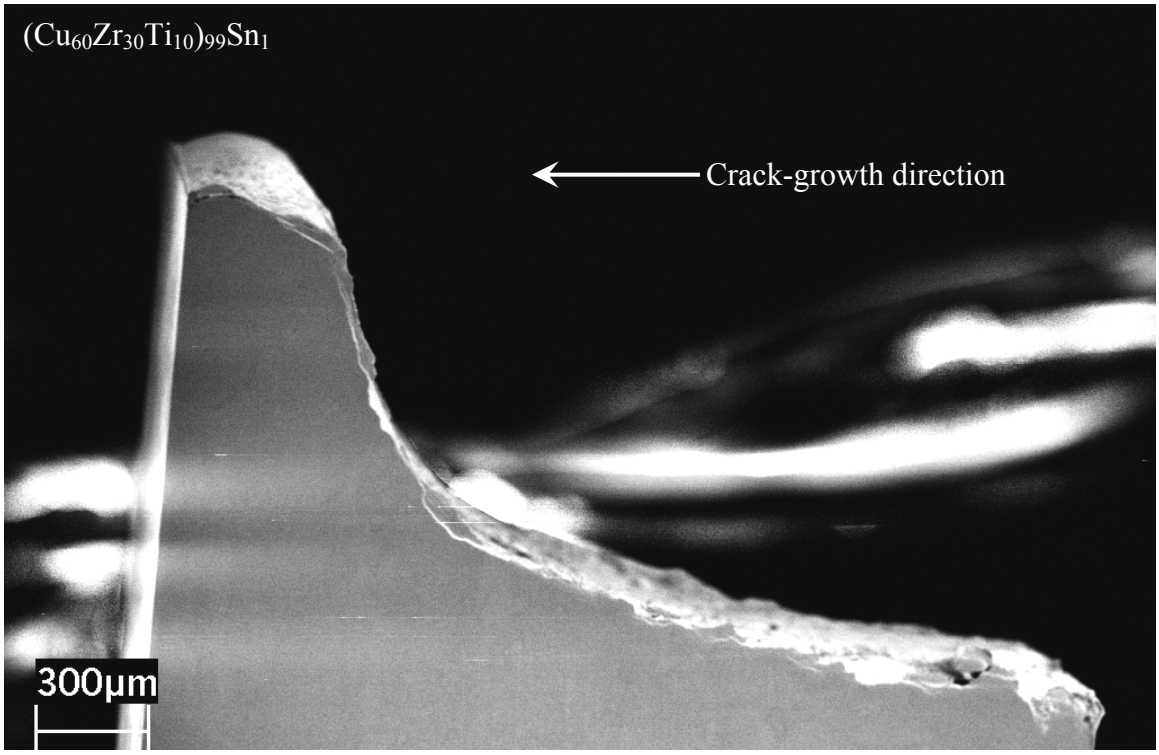

Figure 4-26: Side view of a fracture surface.

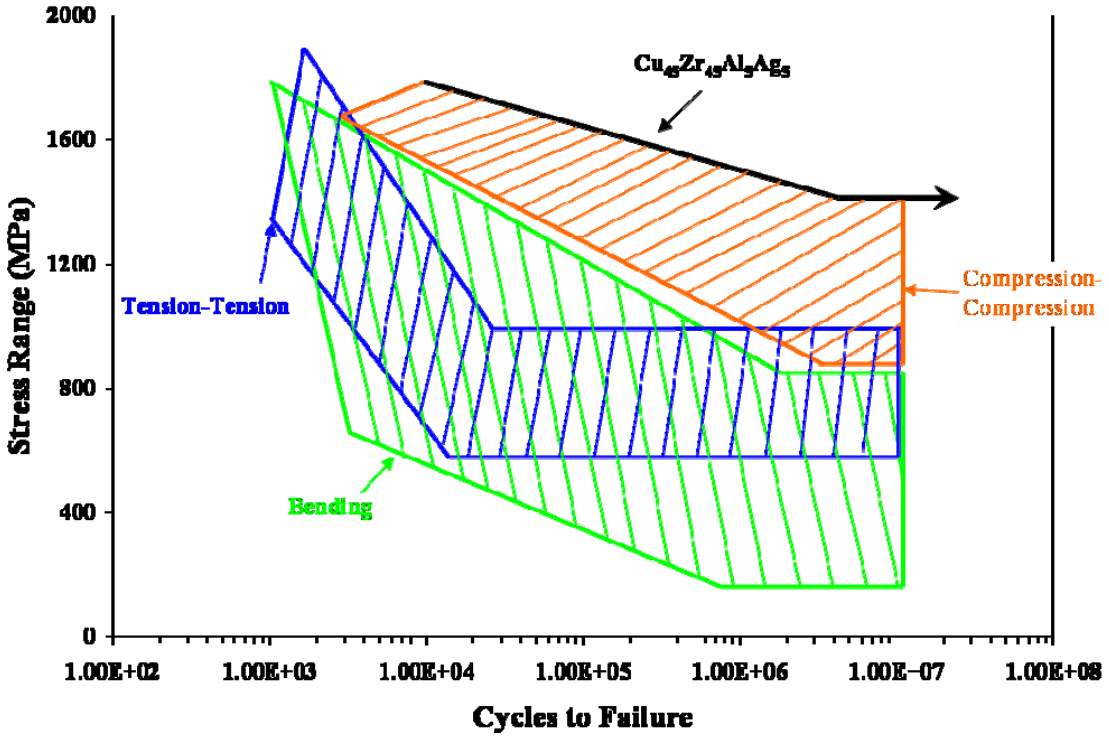

Figure 5-1: A general comparison of the S-N behavior of BMGs under cyclic bending [19, 34, 128, 129, 131-133, 169], cyclic tension [7, 29, 30, 135-139], and cyclic compression [29, 38, 137] loading conditions. Also included are the results for the present $Cu_{45}Zr_{45}Al_5Ag_5$ BMG alloy.

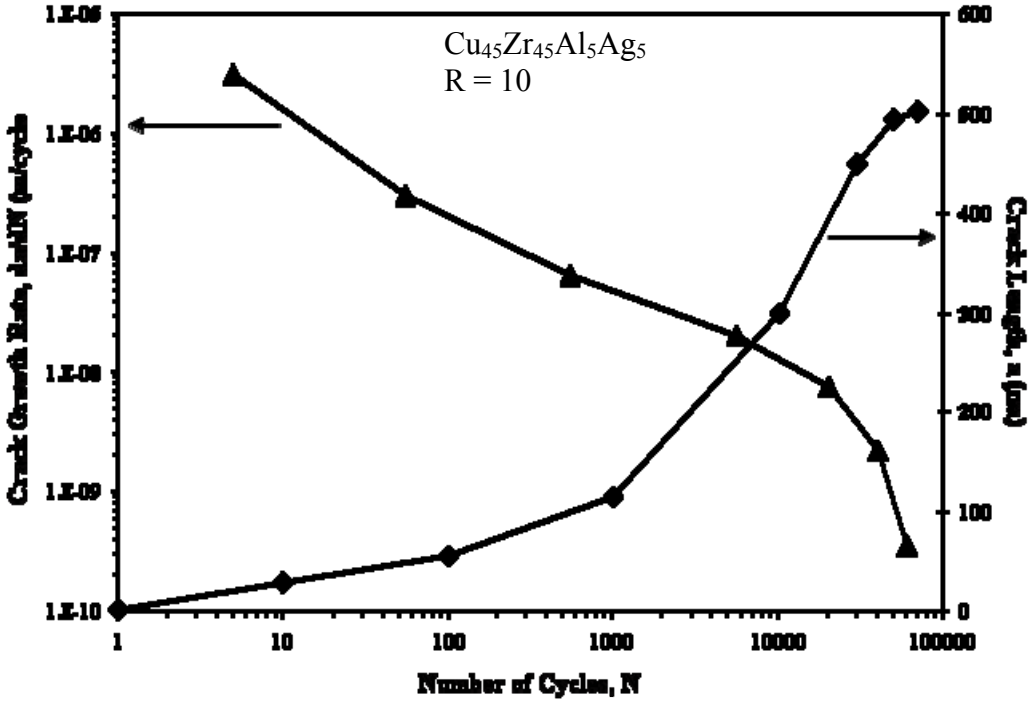

Figure 5-2: The relationship between surface crack lengths and the number of fatigue cycles for Type I behavior. Also plotted is da/dN for the measured crack length data as a function of fatigue cycles.

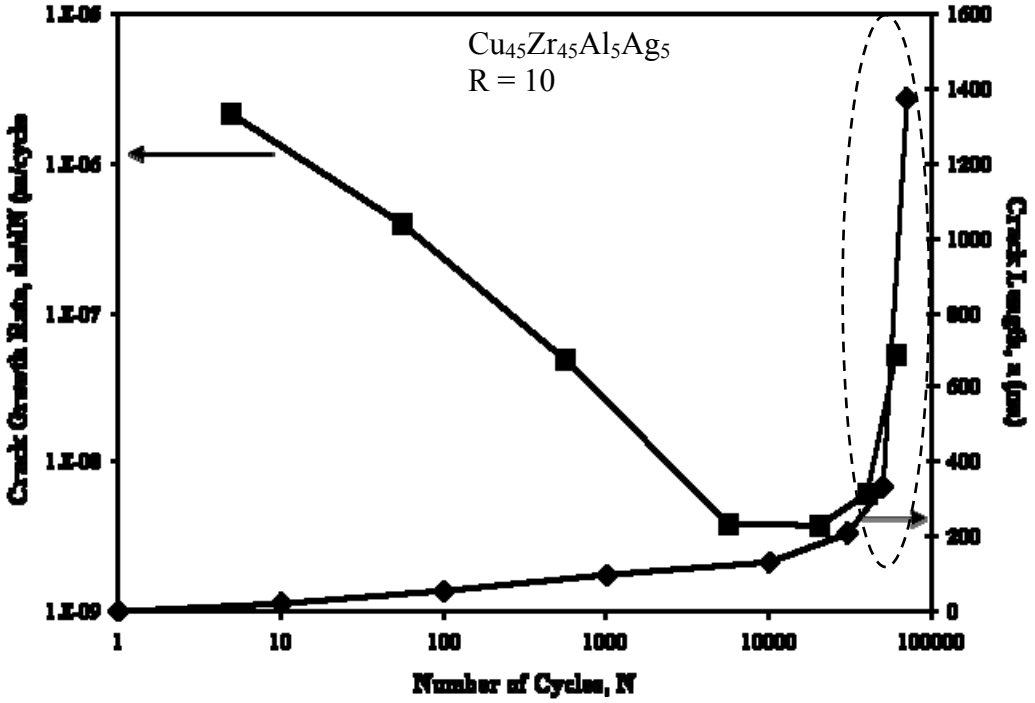

Figure 5-3: The relationship between surface crack lengths and the number of fatigue cycles for Type II behavior. Also plotted is the da/dN for the measured crack length data as a function of fatigue cycles.

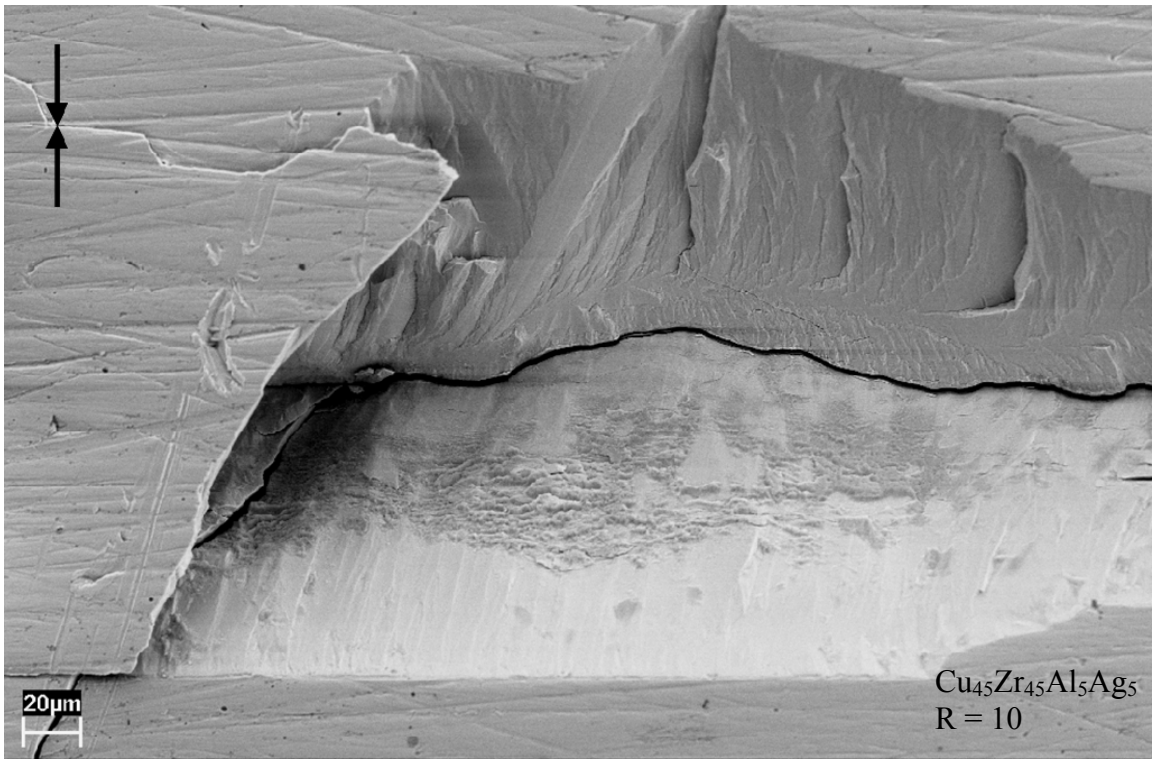

Figure 5-4: Fracture surfaces of a chipped region.

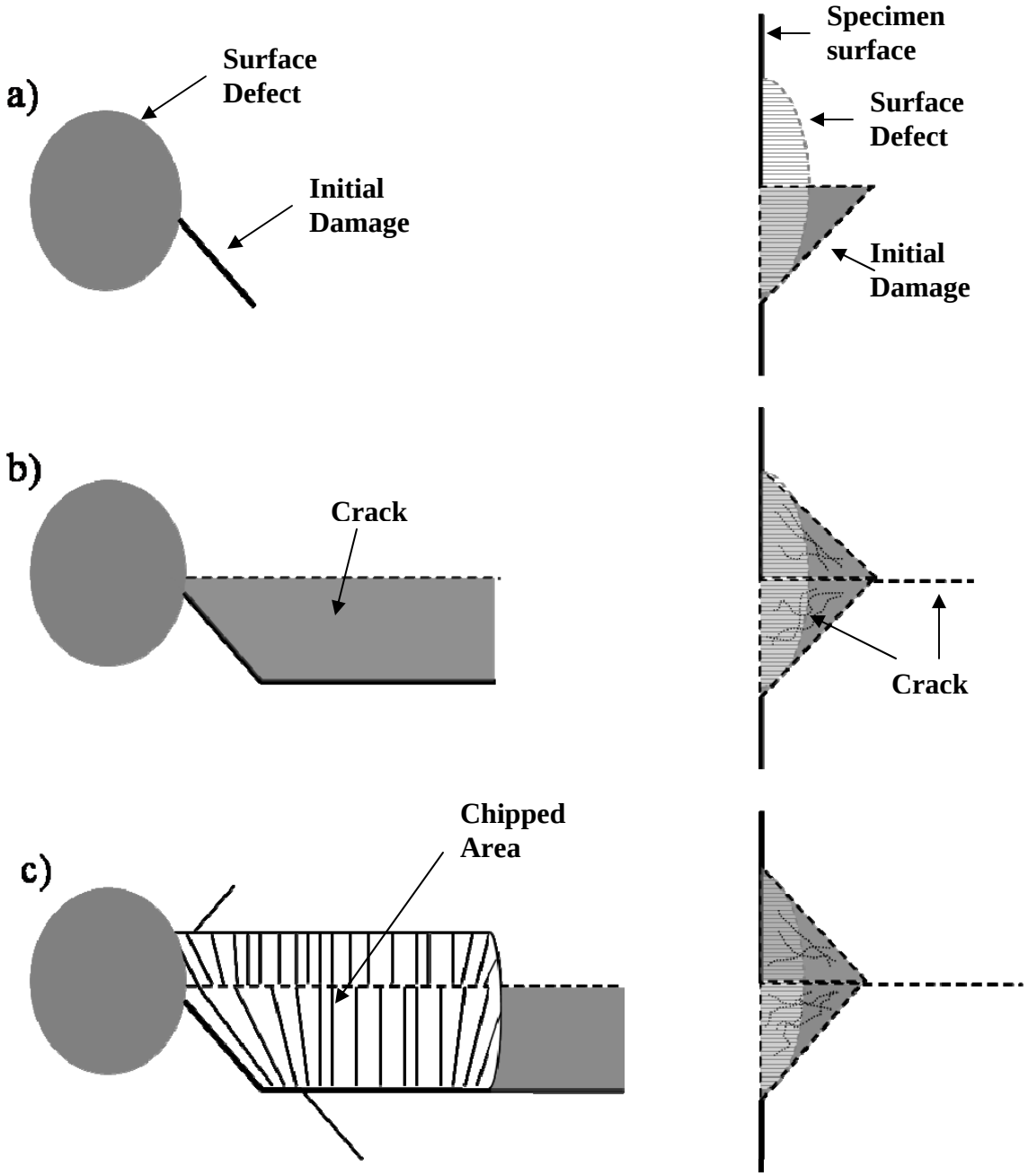

Figure 5-5: Summary of the fatigue damage process that occurs during cyclic compression of BMGs.

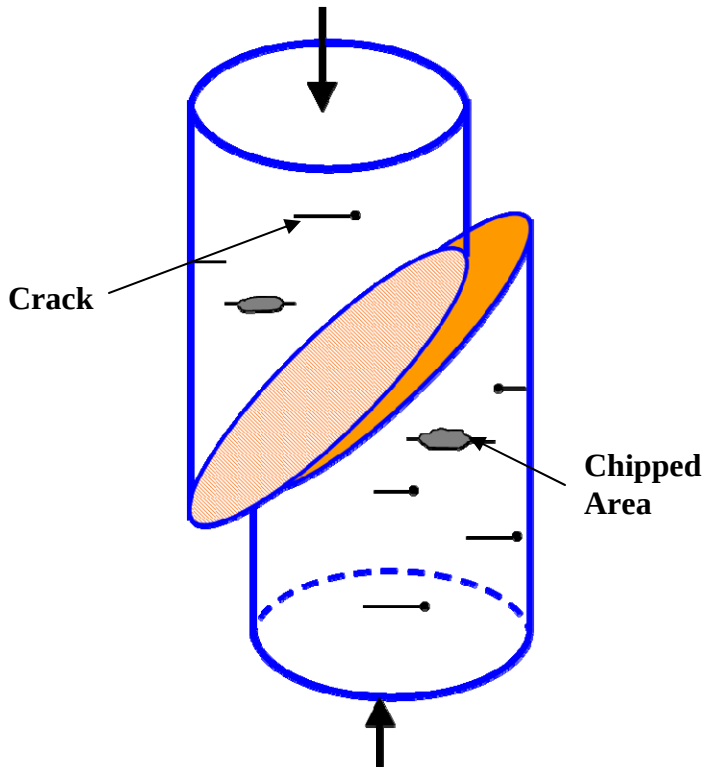

Figure 5-6: Schematic showing the final failure of BMGs under cyclic compression.

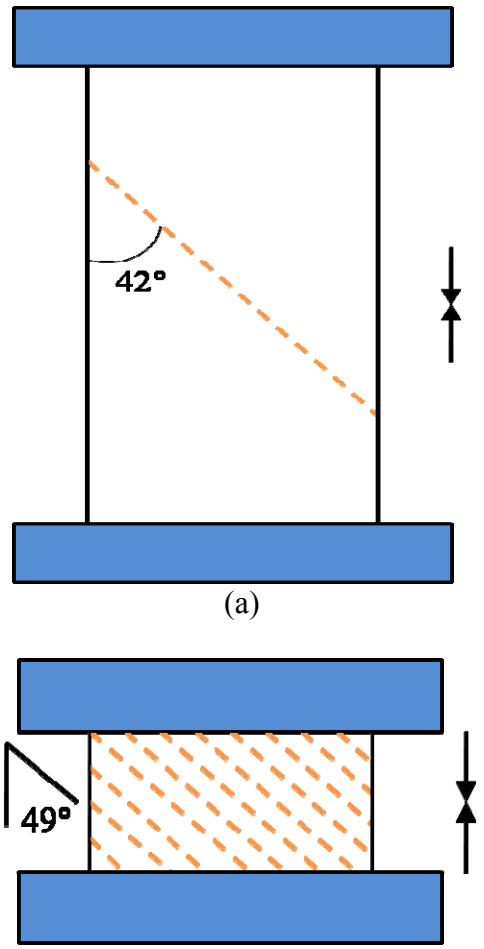

Figure 5-7: Effect of aspect ratio on the shear band behavior; (a) aspect ratio = 2 and (b) aspect ratio = 0.5.

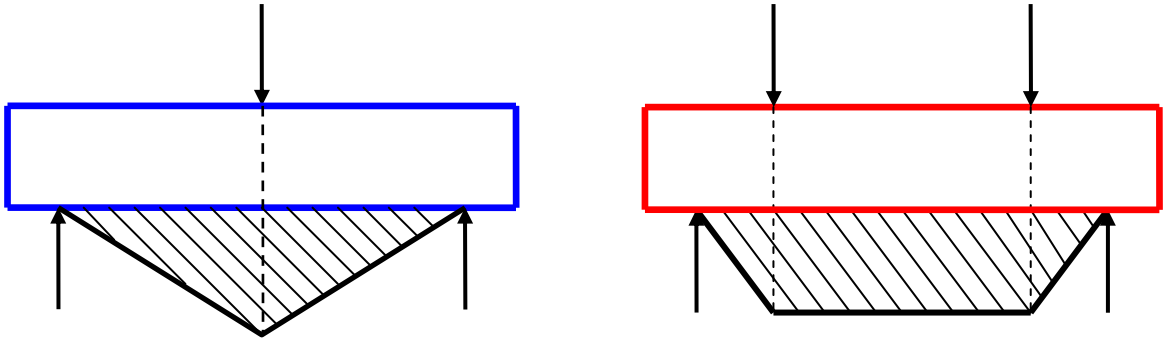

(a) (b)

Figure 5-8: Stress distributions for (a) 3-point loading, and (b) 4-point loading.

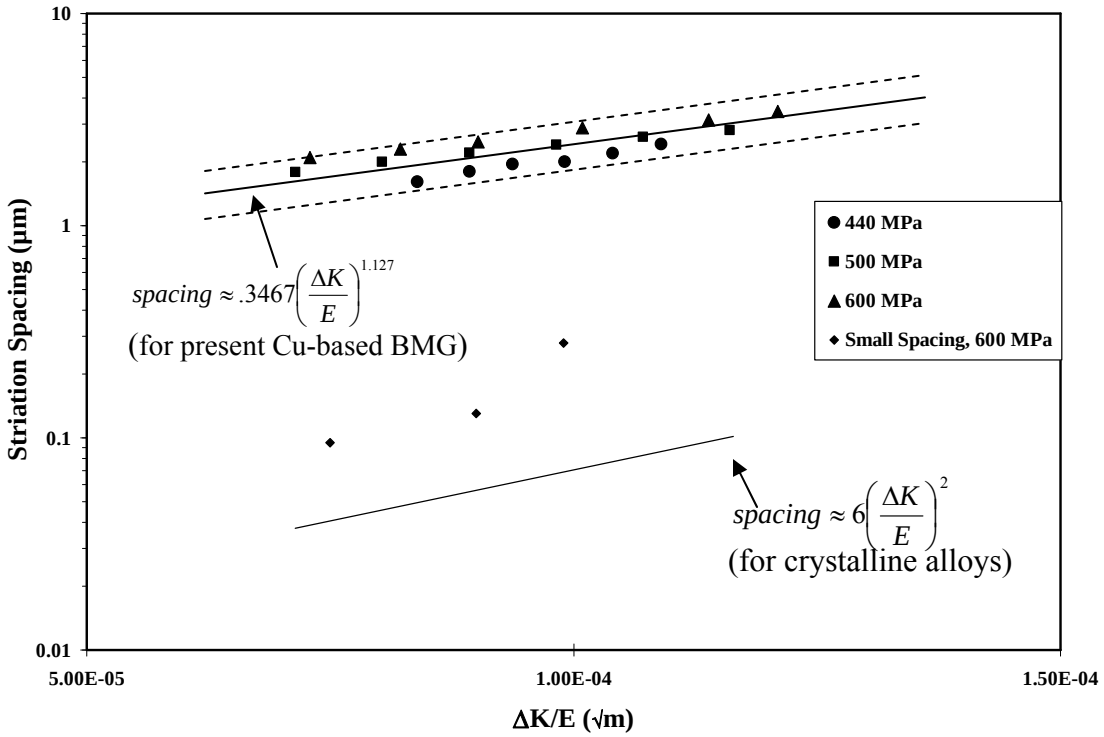

Figure 5-9: Striation spacing as a function of ΔK normalized by E.

VITA

Matthew Webster Freels was born in Clinton, TN. He graduated in 1999 from Clinton High School in Clinton, TN. Matt began his undergraduate studies at Pellissippi State Technical Community College, Knoxville, TN in 1999. He then enrolled at the University of Tennessee, Knoxville, TN in 2001. He received his Bachelor of Science degree in Materials Science and Engineering in 2004. In 2004, Matt began his graduate studies at the University of Tennessee, Knoxville, TN, receiving his Doctor of Philosophy degree in Materials Science and Engineering in 2010.